Master thesis - Mechanical Engineering

Direct Internal Methane Steam Reforming in Operating Solid Oxide Fuel Cells

A kinetic modelling approach

Lindert van Biert 4044452

Delft University of Technology

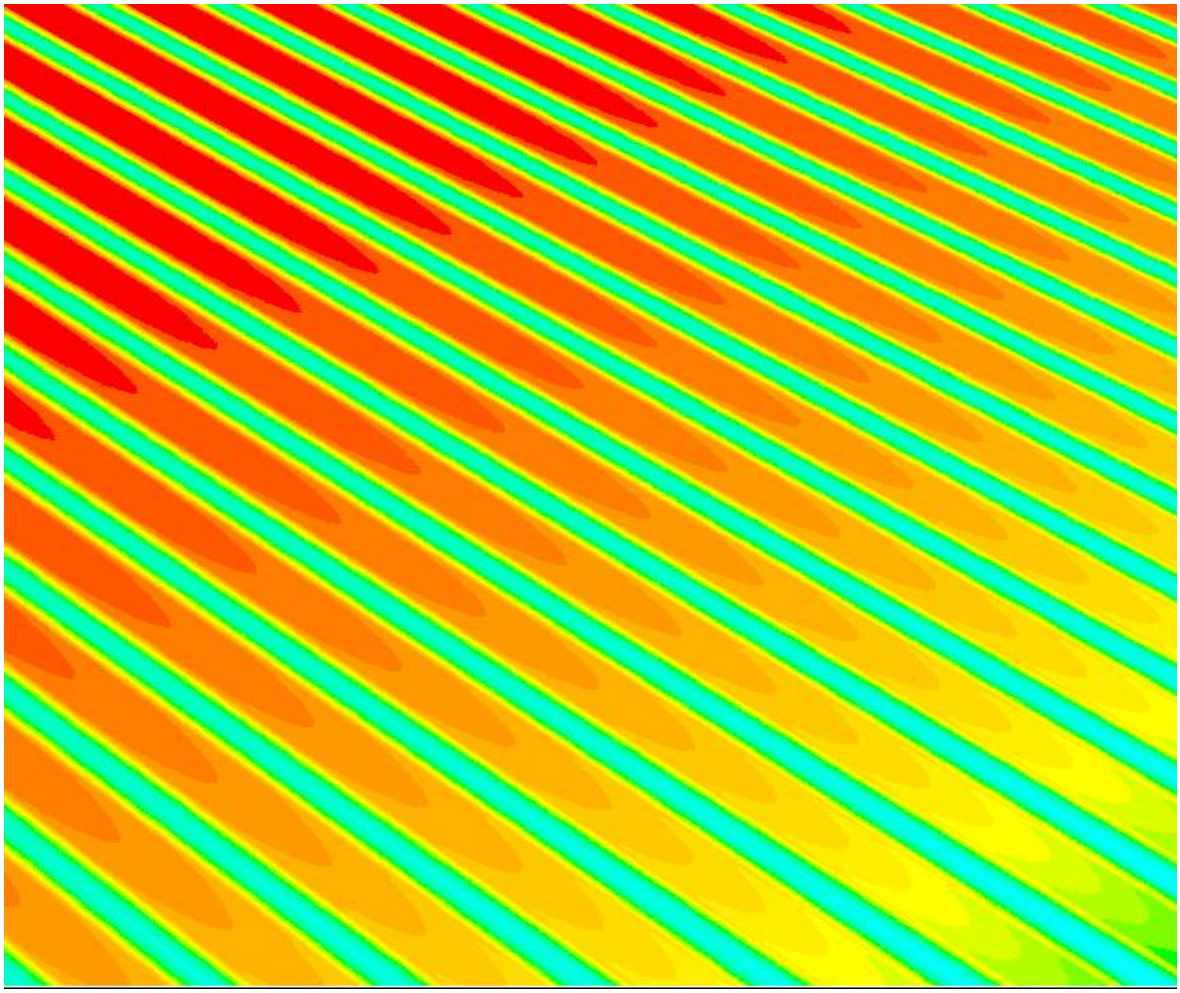

4th of December 2014

TU Delft Delft University of Technology

Specialization Energy Technology,
Faculty of Mechanical, Maritime,
and Materials Engineering

Challenge the future

Abstract

Direct Internal Reforming (DIR) on Solid Oxide Fuel Cell (SOFC) anodes is often considered for fuel cells systems utilising carbon based fuels. Methane Steam Reforming (MSR) is one of the most extensively studied types of DIR. The hydrogen formed by the MSR reaction can be electrochemically oxidised in the fuel cell to produce electricity, while the exothermic electrochemical reaction supplies heat to the endothermic MSR reaction.

The balance is delicate and unsuitable design choices will result in operational problems and poor fuel cell performance. These issues are known for over two decades now and remain unsolved despite several attempts to capture the rate limiting kinetics of the reforming process on fuel cell anodes and modelling studies of methane fuelled SOFCs. It is not yet clear whether MSR kinetics derived from substrate measurements can be used to model SOFC performance and the influence of electrochemistry on the MSR reaction kinetics is rarely reported.

In this work a rate equation is selected based on experimental observations and kinetics proposed in literature, on both industrial catalysts and SOFC anode materials. Ideal reactor models are derived for two specific test setup geometries, considering the electrochemical reactions in the anode. The ideal reactor models are then used to fit the parameters of the selected rate equation to experimental data from earlier work.

The selected rate equation is of the Langmuir-Hinshelwood-Hougen-Watson type. The rate determining kinetics are characterised by the slow reaction of surface adsorbed carbon hydroxide forming carbon monoxide and atomic hydrogen. In addition surface coverage of atomic oxygen on the catalyst is limiting the available number of reaction sites. Two constants and their respective energies, associated with the activation of the rate limiting kinetics and the surface adsorption of oxygen, are fitted to experimental data.

To evaluate the selected rate equation Computational Fluid Dynamics (CFD) type models are developed for the two experimental setups, one with a $Ni-GDC$ anode and the other utilising a $Ni-YSZ$ anode. These model are used to solve fluid dynamics, heat transfer, species transport, and electrochemistry. To model methane steam reforming in the fuel cell anode the selected rate equation is implemented in the CFD models.

The obtained models are used to simulate MSR on the fuel cell anode for the experimental conditions. The modelled methane conversions and I-V characteristics are compared to the experimental values. The spatial distributions in the anode predicted with the selected rate equation and a power law model, fitted to the same experimental data, are compared to evaluate the use of global reaction models.

For the $Ni-GDC$ anode setup the model predicts the experimental methane conversions with good accuracy: the R^2 value is with 0.987 close to unity. The experimental and modelled I-V characteristics are in good agreement. The model adopting a power law reaction mechanism underestimates the gradients in the anode.

However, the model shows poor agreement with the experimental results obtained on the $Ni - YSZ$ test setup. Large deviations with the temperatures and concentrations assumed in the ideal reactor model are found which might explain the inaccuracy of the model.

The good agreement on the $Ni - GDC$ anode suggests that MSR kinetics in SOFCs can be modelled for both open and closed circuit conditions with an appropriate intrinsic rate equation. This was not confirmed for the $Ni - YSZ$ anode. Therefore further investigation with a combined experimental and modelling approach, preferably on similar setups, is required.

Contents

Nomenclature

Abbreviations

BoP	Balance of Plant
CFD	Computational Fluid Dynamics
CISTR	Continuous Ideally Stirred Tank Reactor
CPIM	Cylindrical Pore Interpolation Model
DGM	Dusty Gas Model
DIR	Direct Internal Reforming
GDC	Gadolinium Doped Cerium
IIR	Indirect Internal Reforming
IP-SOFC	Integrated Planar Solid Oxide Fuel Cell
IPFR	Ideal Plug Flow Reactor
LH	Langmuir-Hinshelwood
LH-HW	Langmuir-Hinshelwood-Hougen-Watsen
MPTM	Mean Transport Pore Model
MSR	Methane Steam Reforming
NEMCA	Non-faradaic Electrochemical Modification of the Catalytic Activity
OCV	Open Circuit Voltage
SOFC	Solid Oxide Fuel Cell
TPB	Triple Phase Boundary
UDF	User Defined Function in FLUENT
WGS	Water Gas Shift

YSZ	Yittria-Stabalised Zirconia	

Greek Symbols

α	Reaction order	-
α_a	Anode transfer coefficient	-
α_c	Cathode transfer coefficient	-
α_p	Porous permeability	-
$\bar{\bar{\tau}}$	Viscous stress tensor	N/m^3
β	Reaction order	-
η	Electric potential losses	V
γ_j	Concentration exponent	-
ι	Tortuosity factor	-
λ	Thermal conductivity	$W/(m \cdot K)$
λ_{eff}	Effective thermal conductivity	$W/(m \cdot K)$
μ	Viscosity	$Pa \cdot s$
Ω_D	Diffusion collision integral	-
ϕ	Electric potential	V
ρ	Density	kg/m^3
σ	Electric condutivity	S/m
σ_{ij}	Lennard-Jones characteristic length	m
θ	Surface coverage	m^2/m^2
ε	Porosity	m^3/m^3

Roman Symbols

ΔE_O	surface adsorption energy for atomic oxygen	kJ/mol
ΔG_{gws}	Gibbs free energy change of the water gas shift reaction	kJ/mol
$\boldsymbol{I}$	Unity matrix	-
$\vec{g}$	Gravitational force	N/kg
$\vec{u}$	Flow velocity vector	m/s

A_{ele}	Cell electrolyte area	m^2
A_O	Pre-exponential factor for the surface adsorption of atomic oxygen	-
Br	Brinkmann number	-
c	Speed of sound	m/s
c_p	Heat capacity	kJ/kg
C_{drag}	Inertial drag force	m^{-1}
C_i	Species concentration	mol/mol
CC	Current to carbon ratio	mol/mol
D_i	Mass diffusion coefficient	m^2/s
d_p	Particle diameter	m
$D_{i,T}$	Soret diffusion coefficient	m^2/s
D_{ij}	Binary diffusion coefficient	m^2/s
E	Energy	kJ
E_A	Activation energy	kJ/mol
F	Faraday constant	$s \cdot A/mol$
f	multiplication factor	$mol \cdot Pa/s$
F_{CH_4}	Methane flow rate	mol/s
f_{split}	Split factor for electrochemical oxidation of carbon monoxide	mol/mol
H	Enthalpy	kJ
h	Specific enthalpy	kJ/kg
HC	Hydrogen to carbon ratio	mol/mol
i	Current density	A/m^2
i_{0eff}	Effective reference current density	A/m^2
J	Diffusive flux	$kg/(m^2 \cdot s)$
K	Langmuir adsorption constant	Pa^a
k	Rate constant	*consistent units*
k_0	Rate constant (frequency factor)	*consistent units*
k_{ad}	Adsorption rate constant	mol/s
K_{CHO}	surface adsorption constant for CHO	$Pa^{0.5}$

k_{des}	Desorption rate constant	mol/s
K_{drag}	Viscous drag force	m^{-2}
$K_{eq,wgs}$	Water gas shift equilibrium constant	-
K_O	surface adsorption constant for atomic oxygen	-
l	Length	m
L_c	Arc length of the curve	m
Le	Lewis number	-
M	Mach number	-
M_w	Molar weight	kg/mol
n	Number of electrons involved in the electrochemcial reaction	-
p	Pressure	Pa
p_i	Partial pressure species i	Pa
R	Universal gas constant	J/(mol · K)
r	Reaction rate	mol/(m^3· s)
R_c	Distance between the ends of the curve	m
R_{ohm}	Ohmic resistance	Ω
S_h	Energy source	W/m^3
S_M	Momentum source	N/m^3
S_m	Mass source	kg/(m^3· s)
$S_{i,r}$	Chemical species source	kg/m^3· s
SC	Steam to carbon ratio	mol/mol
T	Temperature	K
t	Time	s
V	Reactor volume	m^3
X	Mole fraction	mol/mol
x_{CH_4}	Methane converted into carbon monoxide	wt%
X_m	Mass fraction	kg/kg
y	Methane converted into carbon dioxide	wt%
Y_i	Species concentration	kg/m^3

Chapter 1

Introduction

Electrochemical conversion is widely applied and is an important technology for the chemical storage of electrical energy. Batteries are electrochemical cells adopted in many portable devices and mobile applications. The fuel cell is another electrochemical cell type that utilises a continuous supply of fuel and oxidant. In principle this process can also be reversed. Unlike batteries the storage capacity of a fuel cell is not limited to the size of the cell. This makes fuel cells more suitable for long term base load storage applications. Important drawbacks are increased electrochemical losses, limited power and storage problems of the fuel.

Hydrogen is an electrochemically attractive fuel but it is difficult to store in a convenient way. Most hydrogen produced these days comes from hydrocarbon fuels. Hydrocarbons, like methane, exhibit less storage problems and are therefore also considered for fuel cell applications. Since direct electrochemical conversion of these fuels is difficult they are usually *reformed* and *shifted* to hydrogen and carbon dioxide. Hydrogen is then utilised by the fuel cell to produce electricity. For low temperature fuel cells reforming and shifting of the fuel is done in an external reformer. In some high temperature fuel cells these reactions can proceed directly in the fuel cell, improving heat integration in the system. This work studies the reforming kinetics of methane on the anode of a high temperature fuel cell.

1.1 Solid Oxide Fuel Cells

Since the first fuel cell was developed by William Grove in 1838, researchers have developed several electrochemical cells that can utilise various fuels to produce electricity [1]. The concept of the fuel cell is however the same in all cases. Fuel is provided on the anode while an oxidant is fed to the cathode. Either the fuel or oxidant is ionised and travels through a membrane, while the electrons travel through an external circuit, thus generating electricity [2].

Fuel cells are categorised according to their membrane, fuel and operating temperature. Generally we consider fuel cells at low (80-200°C), intermediate (600-800°C) and high temperature (>800°C). Among the elevated temperature fuel cells, Solid Oxide Fuel Cells (SOFC) is the type that is studied most intensively because of its wide range of applicability, availability of the materials used and relative simplicity. SOFCs are developed for both high- and intermediate temperature applications.

The electrolyte materials in these type of fuel cells are ceramics, doped with higher valent cations to create oxygen vacancies [3]. This results in high ionic conductivity at elevated temperatures, while the ceramics are practically electrical isolators and gas tight [4]. In Figure 1.1 the working principle of a SOFC is shown. Oxygen, usually from air, is ionised at the cathode. The oxygen ions are transported through the electrolyte to the anode where the fuel is oxidised. The electrons travel through an external circuit to deliver electrical power. Most solid oxide fuel cell are fuelled with hydrogen.

The operation temperature has a significant influence on the electrochemical performance of the fuel cell. The ideal potential of a fuel cell is related to Gibbs free energy from which the ideal voltage, generally referred to as the Nernst potential, can be calculated [5]. The Nernst potential is higher for low operating temperatures which favours the fuel cells in this category. The over potential losses in these cells are however generally high at practical current densities because the electrochemical reactions are slow [6]. To limit these losses, the very noble but expensive Platinum is generally used to catalyse the electrochemical reaction.

At higher temperatures the electrochemical losses can be significantly reduced [7]. Another advantage is the higher tolerance for impurities and carbon monoxide [8]. The high temperature does however force us to use expensive high temperature materials for the other fuel cell parts and the Balance of Plant (BoP). To exploit the thermo mechanical energy left in the flue gas, hybrid systems with gas turbines are used [9]. This results in higher investment costs, the need for heat integration, complicated stack design and long response times of the fuel cell system.

It is because of these issues that research is now focussing on lowering the operating temperature of SOFC, which was originally a high temperature fuel cell [6]. Researchers generally agree that a trade-off exists between the reduction of electrochemical losses at high temperature and the investment and operational costs at lower temperature [10]. This requires a two way approach: effort on lowering the electrochemical losses at lower operating temperature and on bringing down the materials cost at elevated temperature.

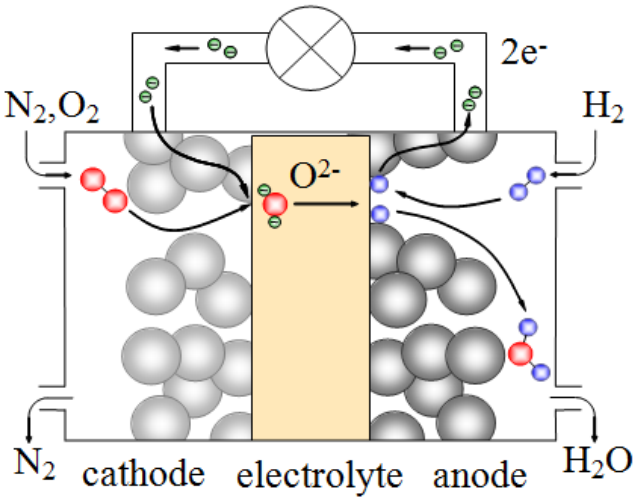

Figure 1.1: The working principle of a fuel cell, fuelled with hydrogen [11].

1.2 Internal Reforming of Methane in SOFCs

Methane is the main component of natural gas and a side product of many petrochemical processes and gasification. Reforming of the methane molecule has become one of the most extensively studied reforming reactions because of its common appearance and relative simplicity. There are two main types of methane reforming, referred to as wet and dry reforming. In wet reforming, the carbon is oxidised with oxygen from steam, yielding an additional hydrogen molecule:

$$CH_4 + H_2O \Leftrightarrow 3H_2 + CO \qquad \Delta H = 206.2[kJ/mol]$$

This is also known as Methane Steam Reforming (MSR) and will be addressed as such in this work. In dry reforming, this oxygen comes from carbon dioxide:

$$CH_4 + CO_2 \Leftrightarrow 2H_2 + 2CO \qquad \Delta H = 247.3[kJ/mol]$$

In many cases these reactions are followed by the Water Gas Shift (WGS) reaction that converts the formed carbon monoxide into carbon dioxide using steam:

$$CO + H_2O \Leftrightarrow H_2 + CO_2 \qquad \Delta H = -41.1[kJ/mol]$$

For the conditions of SOFC operation wet reforming is generally considered to be the most practical type of reforming [12]. Most studies on methane reforming in SOFCs are therefore investigating methane steam reforming.

The solid oxide fuel cell is a convenient electrochemical cell if hydrocarbons are used. Nickel is a well-established anode material that can be used to reform hydrocarbons directly on the fuel cell anode [13, 14]. This property can be used to operate SOFCs with methane as a fuel without the complications of electrochemical methane oxidation, reform hydrocarbons partially or to reform traces left in the fuel [15].

Methane can be supplied to the fuel cell in several ways. The fuel is often externally reformed before it is fed to the fuel cell. In this reforming reaction hydrocarbons are converted into hydrogen and either carbon monoxide or carbon dioxide. This process requires heat, while the electrochemical reactions in the fuel cell produce heat. These processes are therefore sometimes heat-integrated, referred to as Indirect Internal Reforming (IIR). Even further integration can be achieved if the fuel is reformed directly on the fuel cell anode, which is therefore called Direct Internal Reforming (DIR).

The fuel cell anode is in many cases Nickel based, usually mixed with the ceramic electrolyte material to increase the interface between the metal, ceramic and gas phase, referred to as the Triple Phase Boundary (TPB) [16]. Such electrodes are called *cermets* because they consist of both ceramic and metal. Nickel is however also known as a good catalyst for the MSR reaction and is widely adopted in industrial reforming applications. This makes nickel based solid oxide fuel cell anodes a good candidate to combine the electrochemical reactions with methane steam reforming.

1.3 Literature review

In this section some literature is discussed on the modelling of solid oxide fuel cells, capturing electrochemistry and mass transport. In the second part methane steam reforming kinetics is addressed.

1.3.1 Modelling Solid Oxide Fuel Cells

Modelling fuel cells is important for various reasons. The modelling allows us to verify our understanding of the physics involved in electrochemical oxidation and reaction mechanisms in the fuel cell. It can also be used to evaluate experimental data or for design purposes. In this section important literature on the modelling of SOFCs is briefly discussed. This includes the modelling of electrochemistry, mass transport and the detailed modelling of complete SOFCs, considering all relevant physical phenomena.

Electrochemistry

Electrochemical reactions at the electrolyte interfaces are delivering power in a fuel cell. To determine the power drawn from the cell, the relation between current and cell potential has to be calculated. From the thermodynamic equilibrium the ideal cell potential can be determined, which is usually referred to as the *Nernst potential*. In operation, the cell voltage will deviate from this potential due to several losses.

During electrochemical conversion at fuel cell electrodes species are diffusing, adsorbed and reacting at the fuel cell electrodes while ions are diffusing trough the electrolyte and electrons are conducted through the electrode. If the charge transfer process is slow an electrical *double layer* is formed which is polarising the electrode. The respective potential loss is referred to as *activation polarisation* or *activation over potential*. In gas electrodes other physical processes can limit the electrochemical reaction rate as well.

To predict the operating voltage of a SOFC, this over potential has to be calculated. In classical electrochemistry, assuming charge transfer is the rate determining step, this can be done with the Butler-Volmer equation as described by Newman [17]. This equation can be further simplified to either the *Tafel equation* for high activation over potentials and a linear relation for low activation over potentials, as is stated by Chan et al. [18]. They also show that for SOFCs, if errors up to 5% are permitted, it is usually sufficient to use the Tafel equation for the anode over potential and the linear relation for the cathode over potential.

Although the Butler-Volmer equation is usually not capturing the rate determining kinetics for all operating conditions in SOFCs, it can still be used to predict useful current-potential relations. Both Chan et al. and Costamagna et al. [7] parameterised the Butler-Volmer equation for SOFCs. In the latter, the reference current density in the Butler-Volmer equation are of the Arrhenius type and are a function of the composition of the gases involved in the electrochemical reaction.

Other potential losses in the SOFC are *ohmic losses* in the ion conducting parts, mostly the electrolyte, and the electron conducting parts, usually the electrodes. The value of this loss depends on the conductivity of these parts and the current

density with an ohmic relationship. Kharton et al. [19] and Fergus [20] have reported conductivity data for a lot of frequently used electrolyte and electrode materials.

Transport Equations

An important aspect in modelling SOFCs is the effect of transport of reactants and products, especially at high current densities and in complicated geometries. The *concentration losses*, also referred to as *concentration over potential*, can limit the fuel cell performance severely. For SOFCs, these losses are usually largest in the fuel channel and the anode and governed by advection and diffusion of the species involved in the chemical and electrochemical reactions that take place on the fuel cell anode.

Diffusion has an important effect on the transport of species. In the modelling of fuel cells, several diffusion laws have been used, like Fick's law of diffusion, Stefan-Maxwell diffusion and the Dusty Gas Model (DGM), which corrects for the porous zone by including Knudsen diffusion [21–24].

Fick's law of diffusion is only applicable for diluted two component systems, and is therefore inappropriate to model most fuel cell operating conditions. Some authors have pointed out that the DGM would be most appropriate [25]. Calculation of the diffusive flux does however require numerical solution, whereas Fick's and Stefan-Maxwell's diffusive flux can be derived analytically. According to Kerkhof the DGM does have its limitations as well [26].

Alternatively, the Mean Transport Pore Model (MPTM) [27] can be used. Like the DGM this model adds Knudsen diffusivity to a modified Stafan-Maxwell equation. The DGM and the MTPM do however have a different approach for the calculation of the permeation flux. They are discussed in detail in appendix A.

The Cylindrical Pore Interpolation Model (CPIM) [28] might give even better results. This model describes total species fluxes rather than just diffusive mass fluxes. Again, Knudsen diffusion is included. The Knudsen flow coefficient is generally calculated using the formulation of Kennard [29].

The Knudsen flow coefficient is corrected with the porosity divided by the tortuosity. In literature, confusion exists on the formulation of this correction, as some take the tortuosity squared where others don't. Epstein [30] showed that this should be the tortuosity squared, a value that is sometimes referred to as the *tortuosity factor*, which explains the confusion.

Fuel cell modelling

A wide variety of fuel cell models exists, varying from one dimensional models focussing on elementary reactions taking place on the fuel cell electrodes up to fully three dimensional finite volume methods, referred to as computational fluid dynamic (CFD) models, seeking to solve fluid dynamics, species transport, heat transfer, chemical reactions and the electrochemical reactions in the complicated geometries.

Typical examples of one dimensional models are the polarisation model of Chan et al. [18] and impedance models like the one of Bessler [21]. Due to the geometrical simplifications these models are very useful for detailed analysis and understanding of various effects during the fuel cell operation. Chan evaluates the sensitivity to

several electrochemical equations and their validity range. The objective of the model of Bessler is to model elementary reactions and diffusion processes in the fuel cell to model impedance behaviour of fuel cells.

Extension of these models towards two dimensional models gives more insight in the effects of different fuel cell configurations, fuel utilisation, diffusive effects perpendicular to the electrolyte, heat conduction and current distribution. An example of such model is that of Costamagna et al. [7], modelling an Integrated Planar Solid Oxide Fuel Cell (IP-SOFC). They calculate the cell potential for various current densities, solving electrochemistry, species depletion and species diffusion in the anode and fit it to experimental data.

Full three dimensional models are useful to evaluate new fuel cell designs and to capture all relevant physical phenomena. They are however much more computationally demanding. It is because of this and the complexity that these models usually adopt a large number of assumptions. Simplifications are common with respect to boundary conditions, species transport equations, electrochemistry and the electrolyte.

Haberman and Young [31, 32] presented fully three dimensional studies on integrated planar SOFC stacks, one focussing on methane steam reforming reaction kinetics and species distribution in the fuel cell stack, the other one on the electrochemical reactions coupled with the water gas shift reaction. They conclude that multi-component diffusion can be handled correctly using Stefan-Maxwll equations and state the importance of the temperature distribution on the methane reforming reaction.

Similar work was done by DiGiuseppe et al. [33] for a tubular test setup in the commercial package COMSOL. They include Knudsen diffusion in the porous anode and, in contrast to Haberman and Young, verified the model using experimental I-V curves. Their work is used to design experimental conditions and identify possible problems.

In this group, CFD type methods with the commercial code FLUENT have been used by Qu et al. [34] to evaluate the design of the SOFC stack developed by ECN. The work focusses on the distribution of species and current in the cell. The developed model was used by Fan et al. to study fuel flexibility [35] and methane conversion [36] in the proposed design.

Another example is the study of Yuan et al. [37], who used a CFD method to compare a global reaction mechanism with a more detailed multi-step mechanism developed by Hecht et al. [38] for the MSR reaction, using partially pre-reformed methane. They show that the detailed reaction model predicts completely different profiles compared to the global reaction model. This suggests that global reaction mechanisms generally fail to predict the local methane reforming rate correctly.

1.3.2 Methane Steam Reforming kinetics

Methane steam reforming is relatively well studied and yet relatively poorly understood. The reforming of methane in industrial reformers has been studied in more detail and is well established. Some key literature on industrial reforming is therefore discussed. An overview of the discussed MSR rate expressions can be found in Appendix D. Transferring these kinetics to SOFC anodes does however

seem to be not straightforward and this is reflected by the large number of studies done on fuel cell materials, most proposing different rate equations. The reactions are probably even more complicated if the electrochemical reactions have to be considered as well. Few people have addressed this issue, although it is expected to be of significant importance.

Industrial Methane Steam Reforming

Methane steam reforming (MSR) is a relatively well studied reaction for industrial applications. In the second half of the last century several researchers tried to capture the rate determining mechanism on the cheap Ni catalyst, usually on a metal support structure. They argued among each other on the specific influences of methane and steam on the reforming reaction rate.

A standard work on the MSR reaction is that of Xu and Froment [14] who propose a reaction model based on Langmuir-Hinshelwood-Hougen-Watson (LH-HW) kinetics. They postulate that the rate determining step is either the formation of carbon monoxide (high temperatures) and carbon dioxide (low temperatures) from carbon hydroxide on the catalyst. Similar work conducted by Hou et al. [39] shows a very similar reaction mechanism.

As is stated by Elnashaie et al. [40], such a reaction model would explain the contradictions between researchers presenting positive and negative dependency of the MSR reaction on the steam partial pressure and the apparent temperature dependency of reaction orders in global power law kinetics. This is mainly due to the competition between adsorbed methane and steam species on the catalyst for specific experimental conditions.

It is generally agreed that the reaction model proposed by Xu et al. captures the rate determining kinetics of typical industrial methane steam reforming on Ni-based catalysts.

Methane Steam Reforming in SOFCs

Although the SOFC anode is not optimised for methane steam reforming, the Ni-based catalysts used to promote the electrochemical reactions can also be used to reform methane, either wet (with steam) or dry (with carbon dioxide). Usually, wet reforming is used as steam is produced by the electrochemical oxidation of hydrogen and steam protects the anode from carbon deposition [41].

The possibility to use hydrocarbons as a fuel has attracted a lot of attention and resulted in a large number of studies on the MSR kinetics on SOFC anodes. As with industrial reforming a discussion arose on reaction mechanisms, appropriate rate equations and the influence of steam. Several proposed reaction kinetics are discussed in the review of Morgensen et al. [41].

Lee et al. [42], Yakabe et al. [43] and Ahmed et al. [44] studied methane reforming in a similar operating range. All used an empirical power law expression to calculate an overall reaction mechanism on the solid oxide fuel cell anode. They report methane reaction orders in the range 0.85 to 1.4 and steam reaction orders between -0.35 and -1.28.

Achenbach and Riensche [45] argue that large negative dependencies on the steam partial pressure are highly unlikely. In their experiments they investigate

the initial reforming reaction rate for various methane to steam ratios, far from equilibrium. They do not find any influence of steam and show that the reaction is first order in methane in their experiments, if corrections are made for diffusive effects.

Ahmed and Foger [44] mention that the varying reaction orders and the negative reaction orders for steam found in their experiments can be explained by a model such as that of Xu, taking into account the adsorption and desorption effects of the species involved in the MSR reaction.

Dicks et al. [46] obtain temperature dependent reaction orders as well and come up with a Langmuir-Hinshelwood type of rate equations, as does Nakagawa et al. [47]. Both are first order with respect to methane, and negative dependence on the partial pressure of steam originates from adsorption effects of steam or oxygen on the anode.

Perhaps the most extensive study into methane reforming kinetics was done by Hecht et al. [38] on a Ni-YSZ SOFC anode. Their multi-step reaction mechanism contains a set of 42 individual rate equations considering adsorption and desorption of (intermediate) species and reactions between the adsorbed species. Most are of the Arrhenius type and some depend on the CO coverage of the catalyst.

Successful SOFC modelling was done by Janardhanan et al. [48] and Yuan et al. [37] considering the (modified) multi-step reaction model developed by Hecht et al. [38]. They show that the multi-step reaction mechanism predicts behaviour different from overall reaction kinetics and that anode over potentials depend strongly on fuel gas composition and current density. Aguiar et al. [49] investigated a first order in methane model in a full three dimensional steady stat model and concluded that high temperature gradients are expected.

1.3.3 Influence of electrochemical reactions on the Methane Steam Reforming reaction rate

In an attempt to separate electrochemical reactions and the water gas shift reaction from the methane steam reforming reaction, experimental investigation is usually limited to open circuit conditions and using initial reforming reaction rates. It is because of this that the influence of anodic current on the MSR reaction on SOFC anodes is rarely reported.

Dicks et al. [46] mention when they propose their MSR rate equation that the conversion of hydrogen to steam would decrease the methane conversion rate because more steam will block reaction sides. This is in agreement with other authors proposing Langmuir-Hinshelwood reaction types and those who report negative influences of steam in global power law kinetics.

There are two studies which actually report on the influence of electrochemical conversion on the methane conversion rate. Belyaev et al. [50] report an increase in the methane conversion. Apart from the increased methane conversion, the production of carbon monoxide is decreasing and that of carbon dioxide is increasing. They state that this is mainly because of the change in the water gas shift equilibrium, and partially because some carbon monoxide and methane are electrochemically converted to carbon dioxide.

A similar result is obtained by Yentekakis [51], who postulates that methane can

be electrochemically oxidised to carbon monoxide and hydrogen at high methane to steam ratios, and to carbon dioxide and steam for low methane to steam ratios. Such conversion is usually referred to as *faradaic* conversion. In addition, they mention *non-faradaic* enhancement at low temperatures and under coking conditions because of electrochemical modification of the catalytic activity.

1.4 Objectives and outline

Despite two decades of investigation, the direct internal reforming of methane in SOFCs is yet poorly understood. This is reflected in the large number of kinetic expressions that is derived for the MSR reaction. It looks like there are a lot of parameters that have an influence on the reforming reaction. This makes the modelling of methane reforming and its influence on the cell performance very challenging. Because of these difficulties, only a limited number of modelling studies have compared their results to experimental data.

Researchers have tried to simplify the problem by separating out all other influences. The MSR reaction is therefore mostly studied on anode substrates in special reactors designed to control gas phase composition and temperature. Whether the rate equations obtained with this approach can be applied to real SOFC anodes has hardly been investigated. Of particular importance in DIR is the influence of the electrochemical reactions taking place at the same catalyst. Because few studies have been done on real operational fuel cells, this influence is almost never reported.

1.4.1 Objectives

In this study some of the discussed issues are addressed. Based on literature and the experimental investigation done earlier in this group [52] a rate equation is selected. Experimental data is fitted to this rate equation. Since the experimental work is done on operating SOFCs no in-situ measurements have been done and the fuel cell remains a black box. The electrochemistry and water gas shift reaction are additional complications that have to be considered.

In the work of Fan [52] methane steam reforming is studied on two SOFC anodes. In both cases the catalyst is Nickel but one is mixed with Gadolinium Doped Cerium oxide (GDC), generally used for intermediate temperature applications, while the other is mixed with a Yittria-Stabalised Zirconia (YSZ), usually applied in high temperature operation.

To evaluate the obtained rate expression for the specific test conditions, a finite volume model is developed. With computational fluid dynamics the flow field and species diffusion in the test setup is solved. The electrochemistry and water gas shift reaction are also implemented in the model. The rate equation is then hooked to the model and evaluated. With this approach the author tries to:

- Study the influence of the test setup geometry on the spatial distributions in the fuel cell anode;
- Evaluate the use of ideal reactor models for the fitting of experimental data obtained in operational SOFCs;

- Investigate possible Methane Steam Reforming mechanisms on SOFC anodes;
- Study the influence of electrochemical reactions on the MSR reaction rate in SOFC anodes.

1.4.2 Outline

In this work a method is developed to model Methane Steam Reforming reaction in Solid Oxide Fuel Cells. In Chapter 2 ideal reactor models are derived for the experimental setups. Based on literature and the experimental observations a rate equation is selected and the parameters are fitted with the ideal reactor models. To further investigate the proposed kinetic model, full three dimensional CFD models of the fuel cell setups are developed in ANSYS FLUENT. The governing equations in these models are described in Chapter 3. Chapter 4 discusses the implementation of these equations and the mesh optimisation. In Chapter 5 the obtained models are then used to evaluate the proposed reaction mechanism and the parameters fitted with the ideal reactor models. The conclusions and recommendations are discussed in Chapter 6.

Chapter 2

Kinetic rate equations and fitting to experimental data

In the experimental setup used in the study of Fan [52], methane reforming kinetics are studied by measuring the methane conversion for different temperatures, inlet gas compositions and current densities. Methane Steam Reforming reactions have been studied in two setups. The first one is referred to as the square cell set-up as it has a square layout and utilises a $Ni - GDC$ anode. The second one is the button cell set-up with a $Ni - YSZ$ anode.

An integral analysis is then exploited to obtain kinetic parameters for the rate equation. Because the reaction model that was obtained in this way does not predict the conversions well in the CFD model, it was decided to have a closer look at the way these parameters were obtained and to improve the fit where possible.

2.1 General principle of the ideal reactor analysis

In ideal reactors, the conversion only depends on the size of the reactor, the inflow and reactor conditions and the rate equation. In contrast to the study of Fan [52] two reactor types are considered in this work: The Ideal Plug Flow Reactor (IPFR) and the Continuous Ideally Stirred Tank Reactor (CISTR) [53].

The important difference between the two is the assumed amount of mixing: In the plug flow reactor, the flow is not allowed to mix. Initial simulations with the square $Ni-GDC$ cell show that this is probably the best assumption, as can be seen in Figure 2.1a. The stirred-tank reactor is ideally mixed: the outlet concentration equals the concentration in the whole reactor. From initial simulations of the $Ni - YSZ$ button cell this is most applicable to that setup, as the gas concentration is relatively homogeneous in the anode of this setup. This is shown in Figure 2.1b.

It should be noted that both equations are simplifications to the actual distributions in the anode, but the different specific geometries make different ideal models the most reasonable assumption. In both models it is assumed that pressure and temperature are constant and equal to the temperature set in the furnace that was used to heat the fuel cell setups.

The two ideal models are then used to obtain specific kinetic expressions for the anodes used in the experimental work. The data that is extracted from the

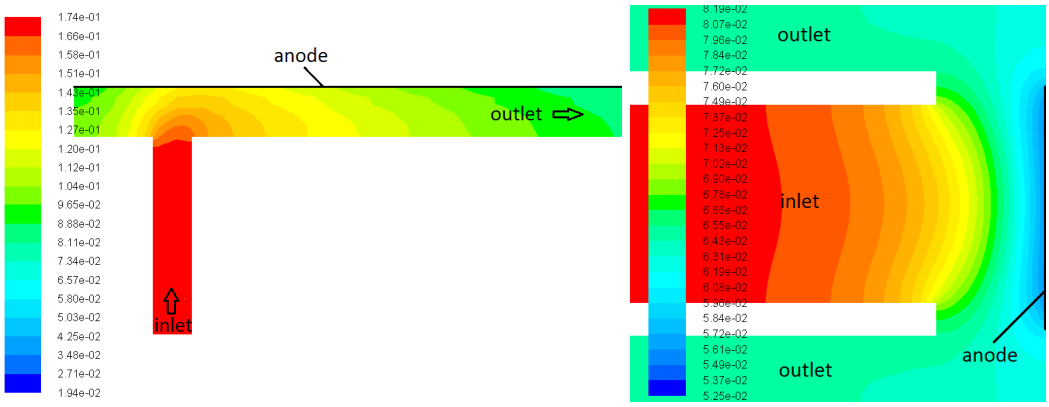

(a) Square cell (b) Button cell

Figure 2.1: Typical distribution of methane in the square cell (2.1a) and button cell (2.1b). It is decided that the IPFR model is most applicable for the square cell, while CISTR is the best assumption for the button cell.

experiment is the conversion of methane, which is defined from the in- and outflows of methane:

$$x_{CH_4} \equiv \frac{F_{CH_4,in} - F_{CH_4}}{F_{CH_4,in}} \tag{2.1}$$

In which x_{CH_4} represents the weight percentage of methane that is converted, and F_{CH_4} is the molar methane flow rate.

2.1.1 Ideal Plug Flow Reactor

In the IPFR the flow is assumed not to mix at all. The volume of the reactor needed to complete the reaction can thus be found using an integral analysis. For a 'reactor unit' V, that is either volume, length, catalyst or whatever is used to quantify the reactor, the differential balance is given by:

$$\frac{dx_{CH_4}}{dV} = \frac{d}{dV}\left(\frac{F_{CH_4,in} - F_{CH_4}}{F_{CH_4,in}}\right) = -\frac{r_{CH_4}}{F_{CH_4,in}} \tag{2.2}$$

In this equation, r_{CH_4} is the reaction rate (mol/m^3· s). With the assumption that the *reactor*, in this case the anode, is the same in all the experiments, V should be a constant and is analytically equal to:

$$V = \int \left(\frac{dV}{dx_{CH_4}}\right) dx_{CH_4} = -F_{CH_4,in} \int_0^{x_{CH_4,final}} \frac{1}{r_{CH_4}} dx_{CH_4} \tag{2.3}$$

The rate equation can be substituted, if expressed in the methane conversion x_{CH_4}.

2.1.2 Continuous Ideally Stirred-Tank Reactor

The evaluation of the CISTR model is mathematical even simpler. In this case, the concentrations in the reactor are assumed to equal the outflow conditions, so the

size of the reactor simply follows from:

$$V = \frac{F_{CH_4,in} - F_{CH_4,out}}{r_{CH_4,out}} = \frac{x_{CH_4,out} \cdot F_{CH_4,in}}{r_{CH_4,out}} \tag{2.4}$$

Again, substituting the rate equation expressed in the final methane conversion $x_{CH_4,out}$ allows calculation of the reactor volume. This reactor volume should be constant, as it is not varied in the experiments. This property is used to find the best combination of parameters in the rate expression using non-linear optimisation algorithms. The algorithm is developed in Matlab, see Appendix E.

2.2 Ideal reactor model of a SOFC anode

An important part of the experimental investigation is to find an appropriate rate equation and determine its parameters to describe the MSR reaction rate. In general, reaction kinetics of gases depend on the concentrations of species involved in the reaction, the temperature and the pressure. A common choice is therefore to present the concentrations of the gases in partial pressures, effectively assuming ideal gas properties of the gas mixture. Often power law kinetics of an Arrhenius type are proposed, yielding expression of the form that is proposed in the study of Fan [52]:

$$-r = k_0 \cdot p_{CH_4}^{\alpha} \cdot p_{H_2O}^{\beta} \cdot exp(\frac{-E_A}{RT}) \tag{2.5}$$

To fit the reaction orders α and β, the frequency factor k_0 the activation energy E_A of such equation to experimental data, the concentration of the various species has to be expressed in terms of the conversion of methane.

2.2.1 Electrochemical reactions

In this particular research the influence of anodic current is of primary interest. Therefore the presence of the electrochemical reaction, converting hydrogen to steam, should be considered. The electrochemical conversion is assumed to progress together with the methane conversion. Therefore a current to carbon ratio (CC) is defined as:

$$CC = \frac{I}{2F \cdot F_{CH_4,0} \cdot x_{CH_4,final}} \tag{2.6}$$

With I the cell current and F the Faraday constant. With this definition, the steam generated by the electrochemical reaction is gradually added and the current density profile is similar in all the experiments. In addition, the current density profile is related to the hydrogen concentration, as is expected. This equation is substituted in Equations (2.7), (2.9) and (2.10) to calculate the species partial pressures.

2.2.2 Water Gas Shift reaction

Another complication is the simultaneously occurring water gas shift reaction. This reaction is assumed to be fast compared to the reforming reaction and is thus in equilibrium. Its progress is defined by $y = x_{CH_4} x_{CO}$ which represents the amount of methane that is converted to carbon dioxide.

The value of y then follows from the equilibrium condition:

$$K_{eq,wgs} = e^{-\frac{\Delta G^0_{gws}}{RT}} = \frac{p_{CO_2} \cdot p_{H_2}}{p_{CO} \cdot p_{H_2O}} = \frac{y(HC + x_{CH_4}(3 - CC) + y)}{(x_{CH_4} - y)(SC - x_{CH_4}(1 - CC) - y)} \quad (2.7)$$

In this expressions, SC and HC are the steam and hydrogen to carbon ratio's at the inlet respectively. The expressions for the partial pressures follow from a mole balance as is described more detailed in the next part. For calculation speed, of particular importance in non-linear fitting, an expression for y is preferred over solving it for every evaluation.

2.2.3 Species partial pressures

With the expressions for the current to carbon ratio and the equilibrium of the water gas shift reaction, the local partial pressures of the species as a function of x_{CH_4} are therefore found by a mole balance:

$$p_{CH_4} = f(1 - x_{CH_4}) \quad (2.8)$$

$$p_{H_2O} = f(SC - x_{CH_4}(1 - CC) - y) \quad (2.9)$$

$$p_{H_2} = f(HC + x_{CH_4}(3 - CC) + y) \quad (2.10)$$

$$p_{CO} = f(x_{CH_4} - y) \quad (2.11)$$

$$p_{CO_2} = fy \quad (2.12)$$

In these relations, f is a multiplication factor to relate all flows to the methane flow at the inlet, as everything is expressed in terms of methane conversion. It also corrects for the increase in the total number of moles during steam reforming. It is finally multiplied by the pressure to obtain the species partial pressure:

$$f = F_{CH_4,in}(\frac{F_{T,in}}{F_{CH_4,in}} + 2x_{CH_4})^{-1}p \quad (2.13)$$

In this equation, $F_{T,in}$ is the total molar flow at the inlet and p is the experiment pressure.

As the rate equation is now expressed in terms of conditions and methane conversion, it can be substituted in Equation (2.4), and the parameters in the rate equation can be fitted to the experimental data. The code that is used to fit the data can be found in Appendix E.

It should be noted that both the IPFR and CISTR are a simplification of the real experimental conditions. Most importantly, effects of diffusion and temperature distribution are not accounted for. It is however, due to its low complexity and low numerical demand attractive for optimisation problems and parameter fitting.

2.3 Experimental investigation by Fan

Experiments were performed by Fan [52] on the two setups mentioned before: the square cell with $Ni - GDC$ anode and $Ni - YSZ$ button cells with two anode thicknesses. Detailed data obtained for every setup can be found in appendix Appendix B. A close look at the results reveals the following trends:

- The reaction rate increases with methane partial pressures and decreases with steam partial pressures;
- The reaction rate increases with temperature for the square cell, but decreases with temperature for the button cell;
- Drawing current from the cell has a positive influence on the methane steam reforming reaction rate.

Attention is drawn immediately to the decreasing reaction rate with temperature which was found for the button cell. Such behaviour is rarely observed, as the rate limiting kinetics are usually heat activated processes. In addition, if such model would be fitted to a power law expression, negative activation energies should be found which is physically highly unlikely.

It is also not straightforward why more steam decreases the reaction rate while drawing current, which increases the local partial pressure of steam, has a positive effect on the methane conversion found in the experiment. Although these observations seem to be in conflict, they are generally reported. Negative reaction orders for steam have been reported by several authors [42,44,47,54]. Positive influence of electrochemical reaction has been reported in the past by Dicks et al., Yentekakis et al. and Belyaev et al. [50,51,54].

The kinetic data shows that methane reforming on SOFC anodes is probably a complex reaction. The specific reaction paths on the anode will need to be investigated to obtain a model that is suitable for design purposes and modelling of more complex fuel cell operation modes. As there is no certainty on the specific reactions on the anode, it is decided to investigate the global dependencies using a power law expression.

2.3.1 Power law kinetics

This section focusses on the rate equation proposed in the work of Fan [52]. As the objective of that work was to obtain insight in the overall kinetics on the anode of SOFCs, the experimental data was fitted to a power law expression, as stated in Section 2.2. This reaction model was fitted to the experimental data in a similar way as described in the previous section, with minor differences. All the data was fitted with a IPFR model.

The strategy adopted by Fan [52] is to fit a combination of the reactions orders α and β in Equation (2.5) for every temperature, using the data of several inlet gas compositions. This solution is obtained by minimizing the standard deviation of the vector $k = k_0 \cdot exp(-\frac{E_A}{RT})$, since k should be constant at constant temperature. With these k vectors for every temperature, k_0 and E_A are finally fitted.

The work of Fan [52] generally reports reaction orders for methane close to one and slightly negative reaction orders for steam. Some correlation with the current density and temperature can be observed. The activation energy does however vary from 39 to 64 kJ/mol for the square cell and from 47 to 196 kJ/mol for the button cell. The rate constant is also varying in a large range. Any trend connected to these variations remains unclear.

Because of this indistinctness and the problems during modelling with this kinetic model, it was decided to check the fitting procedure and improve if possible.

Table 2.1: Result obtained from the improved power law fitting.

$i[A/m2]$	0		600		1000	
	α_{CH_4}	α_{H_2O}	α_{CH_4}	α_{H_2O}	α_{CH_4}	α_{H_2O}
$T[K]$	Square cell, $35\mu m\ Ni-GDC$					
1023	0.671	0.068	0.734	-0.017	0.700	-0.027
998	0.737	-0.029	0.708	-0.059	0.694	-0.114
973	0.728	-0.106	0.617	-0.073	0.598	-0.109
$E_A[kJ/mol]$	87.63		63.21		65.64	
$T[K]$	Button cell, $16\mu m\ Ni-YSZ$					
1048	0.208	-1.859	0.573	-0.967	0.575	-0.736
1023	0.381	-1.582	0.523	-0.709	0.545	-0.504
998	0.525	-0.983	0.525	-0.393	0.518	-0.415
973	0.737	-0.587	0.540	-0.294	0.631	-0.315
$T[K]$	Button cell, $27\mu m\ Ni-YSZ$					
1048	0.846	-0.626	0.583	-0.236	0.544	0.385
1023	0.592	-0.119	0.515	-0.186	0.453	-0.151
973	0.503	0.449	0.491	-0.024	0.525	0.215

2.3.2 Improving the power law fit

Some limitations to the original fitting procedure of Fan [52] were discovered. Therefore the code was improved and further optimised. A different formulation of the electrochemical species source (Equation (2.6)) is proposed and the influence of the anodic current on the WGS equilibrium is included.

The general optimisation strategy remains the same. The integral is now evaluated using global adaptive quadrature. For the optimisation the quasi-newton algorithm is used. The activation energy is finally obtained from a linear fit to the Arrhenius expression in the form:

$$ln(k) = ln(k_0) - \frac{E_A}{R}\frac{1}{T} \tag{2.14}$$

The results obtained with the improved code differ quite a lot from those obtained in the work of Fan [52]. The obtained data is puzzling and appears somewhat uncorrelated. Most important is the variation of the reaction orders with the cell temperature. For the reaction of methane, this value varies between 0.2 and 0.85, and for steam even between -1.86 and 0.45. They also appear to be correlated to the current density in the experiment.

The fitted reaction orders can be found in Table 2.1. For the square cell, the reaction orders are relatively constant with temperature, although some trend can be observed. For the button cells, the reaction orders vary in a larger range and a strong correlation with temperature is observed, especially for the influence of steam.

The temperature dependence of the reaction orders is very undesirable. In the first place, the temperature dependence is usually assumed to be of the Arrhenius type and thus governed by an activation energy. In addition, the value of the activation energy would depend on the temperature dependence of the reaction orders and formulation of the concentration. This causes a great variety in the activation energies and possible negative activation energies, making any fitted activation energy physically meaningless.

For these reasons, the activation energy could only be successfully obtained for the square cell and can also be found in Table 2.1. A decrease in the activation energy is found between open and closed-circuit conditions.

Observations from the power law kinetics

From the power law fitting it is concluded that, although the power law fitting is reasonable for the square cell, it is unable to correctly correlate all physical phenomena. More specifically, power law kinetics cannot explain why the conversion decreases with temperature for the button cell setup. In addition, the negative influence of steam and positive influence of the electrochemical reaction is unlikely to be predicted by a power law model. Other, more intrinsic kinetic rate equations should investigated to capture the physics of methane steam reforming.

2.4 Langmuir-Hinshelwood kinetics

The power law kinetics that were proposed in the previous section do not give a fully consistent and clear fit for the experimental data. The temperature dependent reaction orders and difficult fitting of the activation energy suggest that the power law model is unable to predict the correlations for these experimental conditions. Therefore a more intrinsic kinetic expression is proposed in this section based on kinetic expressions reported in literature. The model is of the classical Langmuir-Hinshelwood-Hougen-Watsen type [55], taking into account surface adsorption of species on the catalyst. The model is fitted to experimental data and evaluated.

2.4.1 Langmuir-Hinshelwood reaction model

The Langmuir-Hinshelwood (LH) reaction model is a classical equation used to describe reactions on surfaces, like a catalyst, involving species that need to adsorb on this surface to react [56]. It can generally be assumed that reactions of species in the gas phase can be neglected. The reaction model on the catalyst then is of the form:

$$A + S \rightleftharpoons AS$$

$$B + S \rightleftharpoons BS$$

$$AS + BS \rightarrow Products$$

It is supposed that the rate determining step in the reaction mechanism is the reaction between adsorbed species on the catalyst surface. The reaction rate is then proportional to the number of reaction sites and the surface coverage of the adsorbed species:

$$r = kC_S^2\theta_A\theta_B \tag{2.15}$$

If the surface coverage of a species can be found by the Langmuir equation, the surface coverage of species A (θ_A) can be approximated by:

$$\theta_A = \frac{k_{ad,1} C_A \theta_E}{k_{des,1} + k C_S \theta_B} \approx \frac{k_{ad,1}}{k_{des,1}} C_A \theta_E = K_1 C_A \theta_E \tag{2.16}$$

Where θ_E is the empty surface area and $k_{ad,1}$ and $k_{des,1}$ are the adsorption and desorption constants for species A respectively. Solving for θ_E and substitution in Equation (2.15) yields the classical Langmuir-Hinshelwood rate equation:

$$r = k C_S^2 \frac{K_1 K_2 C_A C_B}{(1 + K_1 C_A + K_2 C_B)^2} \tag{2.17}$$

Of course, this rate expression is usually a simplified overall equation for a more complex multi-step reaction mechanism. Hougen and Watson expanded this type of expression to a form in which not only the reactants but also products can influence the reaction rate [55]. These reaction mechanisms can become quite complex and several have been proposed for the MSR reaction, both for industrial reactors and SOFC anodes [14, 39, 46, 47, 57].

2.4.2 Proposed kinetic model

The reaction model and analysis is based on the models that have been reported in literature. The idea is that one rate expression of the LH-HW type exists that fits all experimental data, including the effect of the electrochemical reactions. For every tested anode, one set of parameters can be fitted to this LH-HW expression. The rate equation must thus be able to explain:

- The increase of the reaction rate with higher methane partial pressures;
- The decrease in reaction rate with increasing steam partial pressures, especially for the button cell;
- The increase of the reaction rate with temperature for the *Ni-GDC* square cell anode and the decrease of the rate with temperature on the *Ni-YSZ* button cell anode;
- The increase of the reaction rate with increased current densities.

Multiple rate expressions based on kinetic models reported in literature were evaluated. Important criteria are stated above. In addition, the model should represent important physical processes on the fuel cell anode and be thermodynamically consistent. Adsorption constants should be positive and decrease with temperature and the activation energy should have a positive value.

Various rate equations were evaluated and fitted with various strategies. Most were of the LH or LH-HW type and in some cases Freundlich's non-ideal adsorption [58] was considered, effectively giving a hybrid expression of the LH and power law type.

Consequently, the models were discriminated according to the requirements stated above. If an equation was not able to predict our observations, had thermodynamically inconsistent dependencies or had unlikely physical correlations, the

expression was dropped. If Freundlich's non ideal adsorption was considered, care was taken to fit adsorption orders as constant as possible with temperature.

From the model discrimination, kinetics reported in literature [14, 39–47, 57, 59], of which an overview is given in Appendix D, and experimental observations [52], it is concluded that:

- The surface coverage of oxygen can play an important role in the kinetic expression. It is well known that the catalyst provides an excellent pathway for the reaction between surface adsorbed oxygen and gaseous hydrogen. As is often reported, this can result in serious blocking of reaction sites [14, 39, 46]. The amount of surface adsorbed oxygen depends on the gas phase composition and increases with temperature;
- The adsorption of methane on the catalyst is probably much slower and does not seem to result in significant reaction site blocking. The adsorbed amount of methane is proportional to the methane partial pressure;
- A significant negative influence of hydrogen is needed to explain the positive influence of the electrochemical reactions. It is thus likely that hydrogen lean radicals are involved in the rate limiting step;
- It is unlikely that deposited carbon is involved in the rate determining step. As was proposed by Xu et al. [14] it is more likely that the rate limiting step is the formation of adsorbed CO and H from adsorbed CHO;
- The adsorption of the other species does not seem to influence the reaction kinetics in the experimental work of Fan [52];
- The reaction is far from equilibrium and the equilibrium does not influence the reaction kinetics.

If the rate limiting step is indeed the formation of CO from adsorbed CHO, the reaction rate is proportional to the adsorbed amount of CHO on the catalyst. The formation of this radical is then assumed to be fast compared to the formation of CO.

$$CHO(s) + Ni(s) \iff CO(s) + H(s) \tag{2.18}$$

The reaction between CH_4 and H_2O yielding CHO is a multiple step mechanism, governed by adsorption, desorption and surface adsorption of species on the catalyst and reactions between radicals surface adsorbed on the catalyst. Specific reaction paths were proposed by Xu et al. [14] and Hou et al. [39]. The overall reaction of methane and steam yielding surface adsorbed CHO is given by:

$$CH_4(g) + H_2O(g) + Ni(s) \iff CHO(s) + 2.5H_2(g) \tag{2.19}$$

It is not hard to imagine that the amount of surface adsorbed CHO is governed by the equilibrium with the gas phase composition and a specific enthalpy associated with it. The overall equilibrium of this surface adsorption would be:

$$[CHO(s)] = K_{CHO}\frac{[CH_4][H_2O]}{[H_2]^{2.5}} \tag{2.20}$$

Where K_{CHO} is the overall surface adsorption constant for species CHO.

A negative effect of steam is most likely the result of reaction site blocking by surface coverage of oxygen, as the adsorption of steam itself is usually very low. Of course, in SOFC anodes Ni is selected as a catalyst as it provides a pathway between the hydrogen in the gas phase and oxygen ions in the electrolyte. If this is governed by surface adsorbed oxygen on the catalyst the overall reaction becomes:

$$H_2O(g) + Ni(s) \iff O(s) + H_2(g) \tag{2.21}$$

Like the previous surface adsorption reaction, the surface adsorbed oxygen on the surface is in equilibrium with the gas phase according to:

$$[O(s)] = K_O \frac{[H_2O]}{[H_2]} \tag{2.22}$$

Again, K_O is an equilibrium constant for this reaction and is associated with energy of surface adsorption of oxygen on the catalyst.

With these expressions for the surface adsorbed rate limiting species CHO and the reaction site blocking of surface adsorbed oxygen the LH-HW expression for the reaction is obtained using Equations (2.20) and (2.22). Writing the gas phase concentrations as partial pressures, the expression for the reforming rate (mol/m^3·s) becomes:

$$-r = k \frac{p_{CH_4} p_{H_2O}}{p_{H_2}^{2.5}(1 + K_O \frac{p_{H_2O}}{p_{H_2}})^2} \tag{2.23}$$

In this equation, k (mol Bar$^{0.5}$/s) and K_O (unit less) depend on the energy associated with the adsorption, desorption, surface adsorption and reactions on the catalyst and will be of the Arrhenius type:

$$k = k_0 e^{-\frac{E_A}{RT}} \tag{2.24}$$

$$K_O = A_O e^{-\frac{\Delta E_O}{RT}} \tag{2.25}$$

In these equations, E_A is usually related to the activation energy of the rate determining kinetics. Like the energy of the oxygen surface adsorption process ΔE_O, this value should be positive, as energy is generally needed to drive these processes. Therefore, the reaction site blocking of surface adsorbed oxygen will be more severe at higher operating temperatures.

A quick look at the obtained rate expression reveals that it seems to be able to explain our experimental observations:

- The first order dependency on the methane partial pressure agrees with the observed increase in methane conversion at higher methane partial pressures, while the dependency on the desorption of hydrogen explains why the apparent reaction orders in the power law fitting are below unity;
- The reaction site blocking by surface adsorbed oxygen on the catalyst explains the negative dependency on the steam partial pressure and why this is more severe at higher temperatures. This effect is most important at high steam to hydrogen ratios;

- The decrease of the reaction rate with temperature in the button cell setup can be explained by the increasing denominator with temperature, and is thus mainly caused by the reaction site blocking of surface adsorbed oxygen. This agrees well with the observation that the apparent reaction order of steam in the power law fit is almost -2 at the highest temperature for the 16μm anode;
- The negative influence of high hydrogen partial pressures on the formation of surface adsorbed CHO would explain why anodic current promotes the reaction rate, even if additional oxygen is surface adsorbed on the catalyst.

The obtained model thus has four parameters that should be fitted to the data obtained from the experimental investigation by Fan [52].

2.4.3 Parameterizing the kinetic model

To evaluate the rate expression obtained in the previous section, the parameters k_0, E_A, A_O and ΔE_O have to be fitted to the experimental data that was obtained in the work of Fan [52].

The principle of the procedure is essentially similar to the one used to fit the simple power law expression. Although the kinetic model is totally different, the k_0 should still be a constant in the rate expression, and the other parameters can be optimised to obtain k_0 as constant as possible.

The most important difference is a large reduction in parameters. For every data set, a total of four parameters is fitted: In the power law expressions, the reaction orders were depended on temperature and current density ($\alpha(T, i)$) and the rate constant and activation energy were allowed to change with current density ($k_0(i)$, $E_A(i)$).

The new intrinsic kinetics are expected to, at least qualitatively, describe the trends for the whole data set. Therefore, A_O and ΔE_O are simply fitted to obtain the most constant k for every temperature, while k is not allowed to vary with the current density. The obtained k vectors are fitted to the Arrhenius equation to obtain the activation energy E_A and rate constant k_0 for the whole data set.

For the fitting, the equations derived in Section 2.2 are used. The obtained constants for Equation (2.23) are listed in Table 2.2 for every experimentally evaluated anode.

Table 2.2: Constants in Equation (2.23) fitted to the experimental data for the three anodes. It is assumed that the surface adsorption process on the button cell anodes is the same, and so are the constants that represent that process.

Anode	A_O [-]	ΔE_O [kJ/mol]	k_0 [mol Bar$^{0.5}$/s]	E_A [kJ/mol]
35μm $Ni-GDC$	173.8	35.05	1.376e6	164.7
16μm $Ni-YSZ$	2.448e6	116.5	212.3	135.3
27μm $Ni-YSZ$			500.1	136.0

2.4.4 Discussion of the kinetic model

The rate equation is based on a basic ideas of the rate limiting mechanism for methane steam on the Nickel catalyst. Further study and detailed modelling is needed to evaluate the proposed model. The context of the proposed rate equation in literature is discussed in this section.

Context of the kinetic mechanism

The mechanism that is proposed in this section is not new. It is based on a large amount of models reported in literature and discrimination according to the trends observed in the experiments (Appendix B). The model is analytically equivalent to the one obtained by Xu et al. [14] if adsorption effects of CH_4, H_2 and CO are ignored, which is probably a reasonable assumption due to the higher experimental temperatures.

It should be noted that this model was selected after considering a large number of equations. Most models were dropped because they were unable to predict either negative effects of steam, positive influence of hydrogen or the decrease with temperature for the button cell. Other models were dropped because fitted parameters had wrong values to their physical meaning, like positive adsorption enthalpies, negative adsorption constants, and negative activation energies.

The final model is, at least qualitatively, able to explain positive influences of methane partial pressure, negative influences of steam and the promotion of the methane reforming reaction when current is drawn.

This model also explains the 'non-Arrhenius' type behaviour that is sometimes reported [54] and was found in this study, and why the apparent activation energy in the power law changes at closed circuit conditions.

The relatively high steam to hydrogen ratios at closed circuit conditions make the denominator in the expression more dominant. The electrochemical reactions thus result in more surface adsorbed oxygen and lower apparent activation energies. A similar effect was found by researchers before and named NEMCA, Non-faradaic Electrochemical Modification of the Catalytic Activity [51].

Oxygen spillover mechanism

The strong surface adsorption of oxygen on the catalyst might reveal yet another property of the studied fuel cell anode. In the discussion of the mechanism of electrochemical oxidation of hydrogen on the fuel cell anode, several reaction paths have been proposed. Two main types are the *hydrogen spillover* and the *oxygen spillover* mechanisms. The first one assumes that the surface of the catalyst is mainly occupied by atomic hydrogen, while the second one states that the surface is more likely covered by adsorbed atomic oxygen.

A strong surface adsorption of oxygen on the Nickel surface would thus be in good agreement with the oxygen spillover mechanism. This is supported by the conclusions of Rossmeisl and Bessler [60] who did quantum mechanical calculations on the stability of surface-adsorbed molecules on several catalyst metals for electrochemical oxidation is SOFCs. They found that the activity of Nickel was the highest and well-correlated with the stability of surface-adsorbed atomic oxygen. They did

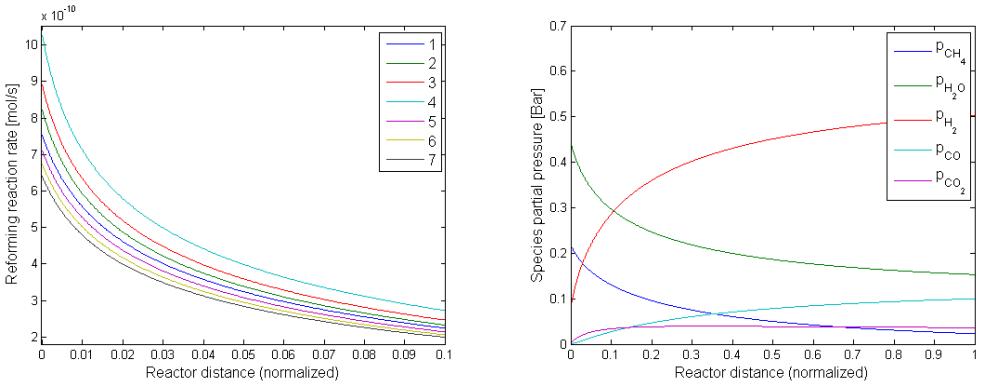

(a) Reforming reaction rate

(b) Species partial pressure

Figure 2.2: Reaction rates for various gas compositions at 1023 K for the $Ni-GDC$ anode at open-circuit conditions (2.2a) and species distribution for case one (2.2b).

not find a correlation with surface-adsorbed hydrogen and therefore conclude that surface-adsorption of oxygen is the most likely pathway for electrochemical oxidation in SOFC anodes.

2.5 Evaluation of the proposed rate equation

The rate equation with the subsequent parameters obtained in this chapter is evaluated in this section. This is done by studying the reaction rate and species distribution for a one dimensional plug flow rector mode and check the dependencies for the stirred-tank reactor. More specifically a closer look is taken at the influence of temperature, steam to carbon ratio and the effects of the electrochemical reaction.

2.5.1 Reactions on the square $Ni-GDC$ anode

To get a clear picture of the progress of the MSR reaction in the square $Ni-GDC$ anode, some results of the fitted rate equation are plotted in Figure 2.2 for the open circuit case at 1023 K. In Figure 2.2a the reaction rates are plotted for cases one to seven. The methane partial pressure was increased in the experiments in cases two to four. In cases five to seven, the steam partial pressure is increased. The exact experimental conditions can be found in Appendix B. In theFigure 2.2b the partial pressures of the reactants and products is plotted in the reactor for the *base case* (case 1) at open circuit conditions and at 1023 K.

It is clear that with the obtained kinetic expression, the negative influence of steam and positive influence of methane is at least qualitatively correctly predicted. The reaction rate is highest in the inflow region and decreases as methane and steam partial pressure decrease and hydrogen partial pressure increases, as would be expected.

The influences of current and temperature are evaluated as well for the base case: the case with lowest methane and steam partial pressures. In Figure 2.3a the

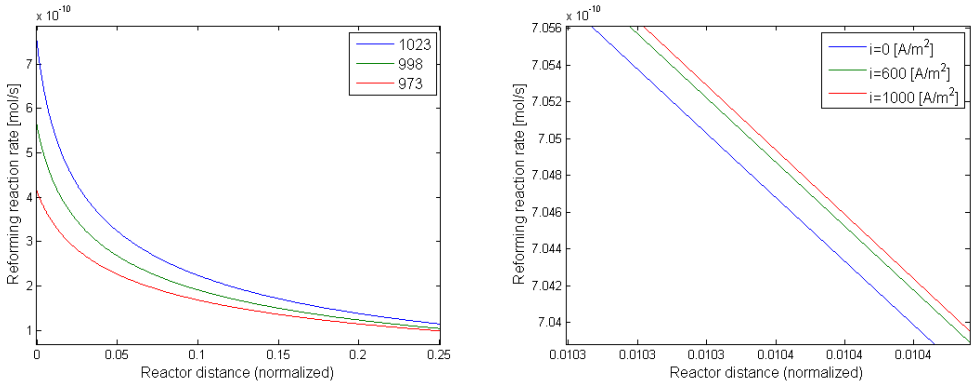

(a) Influence of temperature

(b) Influence of current

Figure 2.3: Influence of temperature on the reaction rate (2.3a) and the influence of current (2.3b) for gas composition 1.

reaction rate is plotted for various temperatures in the first quarter of the anode. The reaction rate is higher for higher temperatures, as is expected.

Of particular interest is the influence of current. In the experiment a small positive influence of current was found. The model is indeed able to predict such positive influence, as can be seen in Figure 2.3b, but the difference is small and is not seen for all cases: usually the lines are very close together. The influence is perhaps more clear at higher current densities. It should also be noted that the actual methane and steam to hydrogen ratio will be lower compared to the IPFR model due to a concentration gradient between the fuel cell and the anode and that the temperature is probably elevated by the electrochemistry. The positive influence of current is therefore most likely underestimated by the IPFR model.

2.5.2 Reactions on the $Ni-YSZ$ button anode

One of the most fascinating experimental results is the decreasing conversion with temperature for the button cell. This is especially interesting since the conversion increases with temperature for the square geometry. A possible explanation is given in this study: The activation energy appears to be significantly lower at the $Ni-YSZ$ anode while the temperature influence on the surface adsorption process seems to be more severe, as can be seen from the fitted parameters in Table 2.2.

For the button cell, it is pointless to plot reaction rates versus the reaction path as it was evaluated with the CISTR model and the concentrations are assumed to be constant in the whole reactor. Therefore, in Figure 2.4 the natural logarithm of the reaction rates are plotted versus the temperature for the various inlet gas compositions.

Figure 2.4a shows results for the tests at open circuit for the 16 μm button cell while in Figure 2.4b results are shown at closed circuit conditions with a current of 1000 A/m^2 applied. In cases one to three, the methane partial pressure of the inlet gas was increased, while in cases two, four and five the steam partial pressure is decreased. The exact experimental conditions can be found in Appendix B.

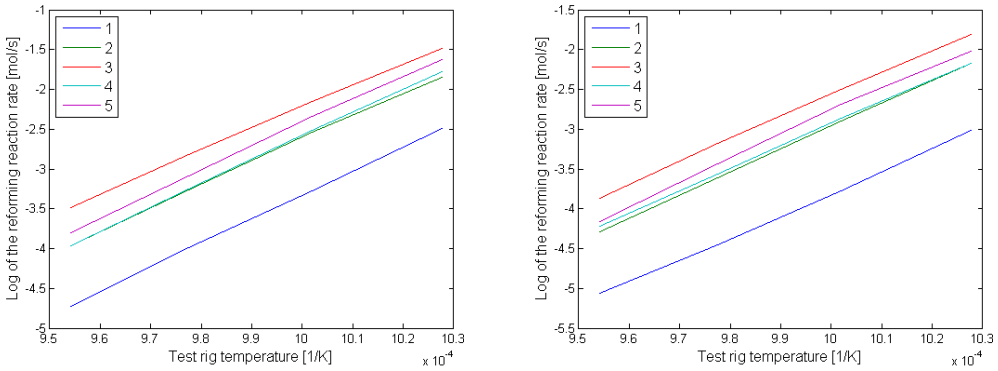

(a) Open circuit

(b) Closed circuit

Figure 2.4: The natural logarithm of the reaction rate in the 16 μm button cell versus the temperature for various gas compositions for open circuit conditions (2.4a) and closed circuit conditions (2.4b)

As is expected, the increase of the methane partial pressure in the inlet gas composition results in higher reaction rates and the decrease of the steam partial pressure is also resulting in higher reaction rates.

Indeed, the increased oxygen surface adsorption at higher temperatures results in severe reaction site blocking at these specific operating conditions and therefore the reaction rate is decreasing with temperature. The model seems to give an appropriate explanation for the decrease in conversion with higher steam partial pressures and temperatures using the same physical phenomenon.

The model fails to predict the improved conversion for closed circuit conditions, as can be seen from comparison between the reaction rates in Figure 2.4. Explanations are discussed in the next section.

2.5.3 Influence of the electrochemical reactions

With the obtained expression, it seems that the model is unable to predict the improved conversion under closed circuit conditions. For the $Ni - GDC$ cell the model does predict some positive influence, but not for all tested cases and under all operating conditions. For the button cell, the model fails to predict the positive influence at all. There can be several reasons for this limitation of the rate expression:

- By assuming a constant reactor temperature, a severe simplification is made to an important parameter. Due to the strong endothermic MSR reaction and exothermic electrochemical reaction, it is likely that there will be deviations. These are more important at high conversions and high current densities;
- As was stated before: due to the assumption of no mixing (IPFR) or complete mixing (CISTR) diffusional effects are ignored. The reality is probably somewhere in between, closer to IPFR for the square test rig and closer to CISTR for the button cell;

- The rate expression is a simplification of probably more detailed multi-step chemistry in the anode. Processes that are not present or irrelevant at open-circuit conditions might become important at closed circuit conditions;
- Several authors have proposed other explanations for the improved catalytic activity due to electrochemical activity, like the NEMCA effect [51].

Some of these explanations can be verified with the CFD model that is also developed in this work. This will be done in the following chapters.

Chapter 3

Governing equations for CFD modelling of operating SOFCs

Computations fluid dynamics is a powerful method to model fluid flows and coupled phenomena, like flow induced forces (lift and drag), heat transfer, chemical reactions, noise generation, phase transitions and so on. The equations governing fluid flow, the Navier-Stokes momentum equation and the continuity equation, have only been analytically solved for hugely simplified flows. In general, especially for complex geometries, researchers therefore rely on numerical methods to calculate the flow field. In this work, computational fluid dynamics is used to develop a SOFC model with the inclusion of electrochemical reactions and methane steam reforming reaction in the fuel cell anode. In this chapter, the methods used for CFD calculations, SOFC simulation and chemistry are discussed.

3.1 Computational Fluid Dynamics

In CFD the problem is discretised. For example, in finite volume methods it is divided into a finite number of volumes, for which mass, momentum and coupled balances are solved in an iterative way. The set of equations that needs to be solved are of continuity and momentum, heat transfer, species transport, electrochemistry and chemical reactions.

3.1.1 Continuity equation

The continuity equation, or conservation of mass, has the form:

$$\frac{\partial \rho}{\partial t} + \nabla \cdot (\rho \vec{u}) = S_m \tag{3.1}$$

It leads to the definition of the so called material derivative (not discussed here) if the mass source term (S_m) is zero. In porous media, the continuity equation changes to:

$$\frac{\partial (\varepsilon \rho)}{\partial t} + \nabla \cdot (\varepsilon \rho \vec{u}) = \varepsilon S_m \tag{3.2}$$

With ε the porosity of the medium. The continuity equation is not only a fundamentally important principle, it is used to calculate the pressure distribution in flow field and is an important measure of the convergence of the computations.

3.1.2 Conservation of momentum

The Navier-Stokes or conservation of momentum equations are used to calculate the velocities of the flow field. They have the following general form:

$$\frac{\partial(\rho\vec{u})}{\partial t} + \vec{u}\cdot\nabla(\rho\vec{u}) = -\nabla p\boldsymbol{I} + \nabla\bar{\bar{\tau}} + \rho\vec{g} + S_M \tag{3.3}$$

$$\bar{\bar{\tau}} = \mu[(\nabla\cdot\vec{u} + \nabla\cdot\vec{u}^T) - \frac{2}{3}\nabla\cdot\vec{u}\boldsymbol{I}]$$

But for an incompressible flow ($M \equiv u/c = u/\sqrt{\gamma RT} \ll 1$) and if $\nabla\cdot\vec{u} = 0$ a more simpler form is obtained:

$$\rho(\frac{\partial\vec{u}}{\partial t} + (\vec{u}\cdot\nabla)\vec{u}) = -\nabla p + \mu\nabla^2\vec{u} + \rho\vec{g} + S_M \tag{3.4}$$

In the Navier-Stokes equation S_M is a momentum source term, for example in porous media and μ is the viscosity of the fluid. Note that $\nabla\cdot\vec{u}$ isn't necessary equal to zero since the mass source term S_m is not zero at the TPB.

In the porous zones, the Navier-Stokes equations should be solved based on the physical velocity if convection or diffusion is expected, and they have the form for an incompressible flow and an isotropic porous zone:

$$\varepsilon\rho(\frac{\partial\vec{u}}{\partial t} + (\vec{u}\cdot\nabla)\vec{u}) = \varepsilon(-\nabla p + \mu\nabla^2\vec{u} + \rho\vec{g}) + S_M \tag{3.5}$$

The momentum sink is implemented in FLUENT in the following form:

$$S_M = -(\frac{\varepsilon^2\mu}{K_{drag}} + \frac{\varepsilon^3 C_{drag}}{2}\rho|\vec{u}|\vec{u}) \tag{3.6}$$

In which the first term represents a viscous and the second term an inertial drag force. This equation is implemented in the FLUENT model considering purely viscous drag. The constant is based on earlier work in this group [61]. An alternative but similar way to calculate the viscous drag that is adopted by Hosseini et al. [62] can be found in Appendix A.

3.1.3 Energy equation

The energy equation, here written in its general form for the porous zones, is used to compute the conservation of energy:

$$\frac{\partial}{\partial t}(\varepsilon\rho_f E_f + (1-\varepsilon)\rho_s E_s) + \nabla\cdot(\vec{u}(\rho_f E_f + p)) = \nabla\cdot[\lambda_{eff}\nabla T - \sum_i h_i J_i] + S_h \tag{3.7}$$

The subscripts f and s refer to the fluid and solid region respectively. The total energy is given by:

$$E = h - \frac{p}{\rho} + \frac{u^2}{2} \tag{3.8}$$

And the effective thermal conductivity by:

$$\lambda_{eff} = \varepsilon\lambda_f + (1-\varepsilon)\lambda_s \tag{3.9}$$

The second term in Equation (3.7) describes the transport of energy due to species diffusion. This term should not be neglected if the Lewis number, which is the ration between thermal and mass diffusivity, is far from unity:

$$Le = \frac{\lambda}{\rho c_p D} \ll 1 \tag{3.10}$$

Viscous heating should also be included if the Brinkmann number is close to unity:

$$Br = \frac{\mu u^2}{k_t \delta T} \approx 1 \tag{3.11}$$

A quick estimation shows that that the viscous heating can be neglected, but the diffusion energy source cannot.

Sources in the energy equation are present from chemical reaction energy and ohmic losses in the electrodes:

$$S_{h,chem} = -\sum_i h_i (S_{i,r})_{chem} \tag{3.12}$$

$$S_{h,ohm} = i^2 R_{ohm} \tag{3.13}$$

Where i is the local current density and R_{ohm} is the ohmic resistance.

3.1.4 Species transport

Transport equations are very important in fuel cells, both in the gas channels and the porous anode or cathode. Both the chemical and electrochemical reaction kinetics depend very much on the concentration of the species involved. Their distribution is therefore crucial in modelling solid oxide fuel cell performance and chemical reactions.

Species transport equation

The general (mass based) species transport equation is of the following form:

$$\frac{\partial}{\partial t}(\rho Y_i) = -\nabla \cdot (\rho \vec{u} Y_i) - \nabla \cdot \vec{J}_i + S_{i,r} \tag{3.14}$$

$$S_{i,r} = \sum_{l=1}^{N_R} (S_{i,r})_l \tag{3.15}$$

Where $\vec{J}_i$ is the diffusive flux and $S_{i,r}$ the source from chemical reactions. To calculate the diffusive flux of a species a diffusion law is implemented.

Single component diffusion: Fick's law of diffusion

The most simple but still quite useful law of diffusion is developed by Fick:

$$\vec{J_i} = -\rho D_i \nabla Y_i - D_{i,T} \frac{\nabla T}{T} \tag{3.16}$$

The thermal diffusion $D_{i,T}$ is also included in FLUENT using the (Soret) diffusion coefficient from an empirical relation. This accounts for the slower diffusion of heavy molecules compared to light molecules. Fick's law is the most famous and most simple law of diffusion, but it only holds for one diluted component, which is definitely not applicable for fuel cells.

Multicomponent diffusion: Stefan-Maxwell

For multicomponent diffusion in FLUENT, Stefan-Maxwell diffusion is implemented. A short derivation of the equations used, based on Merk [24]:

$$\sum_{j=1,j\neq i}^{N} \frac{X_i X_j}{D_{ij}} (\vec{u}_j - \vec{u}_i) = \vec{d_i} - \frac{\nabla T}{T} \sum_{j=1,j\neq i}^{N} \frac{X_i X_j}{D_{ij}} (\frac{D_{T,j}}{\rho_j} - \frac{D_{T,i}}{\rho_i})$$

If pressure diffusion is negligible $\vec{d_i} = \nabla X_i$ and since $\vec{J_i} = \rho_i \vec{V_i}$:

$$\sum_{j=1,j\neq i}^{N} \frac{X_i X_j}{D_{ij}} (\frac{\vec{J_j}}{\rho_j} - \frac{\vec{J_i}}{\rho_i}) = \nabla X_i - \frac{\nabla T}{T} \sum_{j=1,j\neq i}^{N} \frac{X_i X_j}{D_{ij}} (\frac{D_{T,j}}{\rho_j} - \frac{D_{T,i}}{\rho_i})$$

$$\vec{J_i} = -\sum_{j=1}^{n-1} \rho D_{ij} \nabla Y_j - D_{i,T} \frac{\nabla T}{T} \tag{3.17}$$

As we can see from this derivation, FLUENT calculates generalised Fick's law coefficients using Stefan-Maxwell, mostly because this is computationally preferred over computation of multicomponent diffusion coefficients.

Binary diffusion coefficients

The binary diffusion coefficients required to calculate the diffusive flux with the Stefan-Maxwell equations can be either specified by the user or calculated from kinetic theory, using a modified Chapman-Enskog formula:

$$D_{ij} = 0.00188 \frac{[T^3 (\frac{1}{M_{w,i}} + \frac{1}{M_{w,j}})]^{1/2}}{p_{abs} \sigma_{ij}^2 \Omega_D} \tag{3.18}$$

In this model σ_{ij} is the average collision diameter, referred to as the Lennard-Jones characteristic length, and Ω_D the diffusion collision integral that is calculated by FLUENT based on the Lennard-Jones energy parameter. Both can be found in literature [63]. An alternative way to calculate the diffusion constants that is often used in literature is based on the Fullers volume and can be found in the Appendix A.

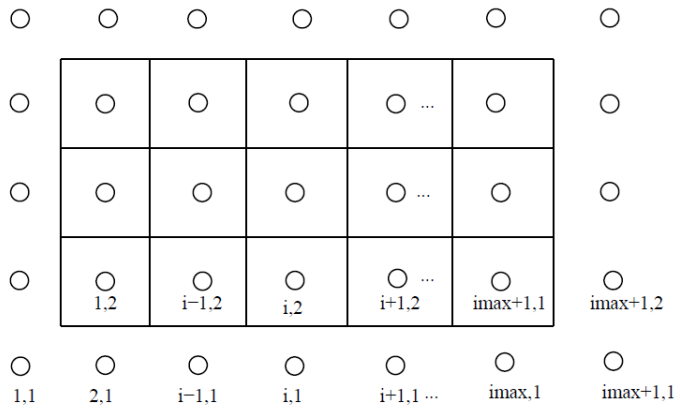

Figure 3.1: Example of a simple 2D grid. For the boundary conditions, virtual points are generated outside the calculation domain.

3.1.5 Solving fluid mechanics using CFD

To solve the equations discussed above, FLUENT uses finite volume methods. The problem is to be spit in a number of finite volumes. Balances of mass, momentum, energy and species are set up for each cell in the computational domain. In this way, a huge number of equations is obtained, because they have to be solved for every grid cell. The equations do however become simpler and numerically attractive.

Discretisation

The idea of discretisation is simple: computers do not really allow us to solve more difficult equations, but they do allow us to solve a lot of them. Splitting the problem in multiple parts and simplifying the equations will give an error, but if we keep the error within certain limits it allows us to solve the equations on more complicated geometries and problems. It is out of the scope of this report to discuss the possible ways of problem discretisation, but a brief example will be discussed.

Consider the two dimensional problem in Figure 3.1. A simple, equidistant square mesh is generated in this case. The set of equations needs to be solved for each of the cells. As an example we will discuss solving stationary advection and diffusion of 'C' on this particular problem. What we want to solve is:

$$U\frac{\partial C}{\partial x} + V\frac{\partial C}{\partial y} = k\frac{\partial^2 C}{\partial x^2} + k\frac{\partial^2 C}{\partial y^2} + S \tag{3.19}$$

Where the left hand side contains the advection equations, the first two terms on the right hand side the diffusion equations and the last term accounts for a source of C. To discretise this for cell i, j, we set up a balance through the cell walls. We can estimate the concentration of C at the cell walls by averaging the quantities in the two cells, to obtain for example on the left cell:

$$(U\frac{\partial C}{\partial x})_{left} \approx U\frac{C_{i,j} + C_{i-1,j}}{2\Delta x} \tag{3.20}$$

This is done in a similar way for the right, top and bottom cell. For the diffusive flux we need an estimation of the second order derivative and we do not need to know the value in the node: the cell values will do. It will be of the form:

$$(k\frac{\partial^2 C}{\partial x^2})_{left} = k\frac{C_{i,j} - C_{i-1,j}}{\Delta x^2} \tag{3.21}$$

If this is done accordingly for the other boundaries as well, we end up with a discretisation of cell i:

$$U\frac{C_{i+1,j} - C_{i-1,j}}{2\Delta x} - V\frac{C_{i,j+1} - C_{i,j-1}}{2\Delta y} = K\frac{C_{i+1,j} - 2C_{i,j} + C_{i-1,j}}{\Delta x^2} + K\frac{C_{i,j+1} - 2C_{i,j} + C_{i,j-1}}{\Delta y^2} + S_{i,j} \tag{3.22}$$

There are various ways of discretising the equations, which will not be discussed in this chapter. The method of discretisation does of course have huge implications on the accuracy of the solution. It will depend on the size of the grid cells taken and the order of the discretisation method. The error of the method can be found using Taylor expansions, and in general higher order schemes have lower inaccuracy. They do however not pay off on coarse grids, as the error from the finite volume approximation will in that case dominate the solution.

Solving the discretised equations

Once the discretised expression are obtained for all the interior grid cells, the boundary conditions are applied to the boundary cells. There are several ways to do this, depending on the type of boundary and boundary condition. For stationary problems, like this work, an initial guess is given. A matrix equation obtained, which is iterated until the solution does not change anymore: the solution is converged.

Due to its non-linearity it is somewhat more complex to solve the Navier-Stokes equations. FLUENT handles that problem by linearizing the momentum equations and iterate them. Then the continuity equation is used to update the pressure in the cells after which other balances are iterated and the next iteration starts. In this way the program can handle a complex system of equations.

Stability is always an issue with numerical problems. The stability of the problem will depend on the formulation, discretisation and numerical scheme. In addition several numerical strategies can be exploited. This include sequentially solving rather than simultaneous, limiters and under-relaxation. In the last case, the new solution is partially replaced by the old one by a weighted average, forcing the solution to change slowly.

3.2 Modelling electrochemistry and Methane Steam Reforming

The modelling of SOFCs can be a very valuable tool in their development as it can, at least partially, replace expensive experiments. The difficulty in modelling them is the amount of closely coupled physical phenomena that need to be accounted

for. The experimental validation of such models can therefore be challenging, as detailed information about these phenomena need verification inside the fuel cell.

In this work a model is developed for two experimental fuel cell set ups. The first one a square cell with a fuel distributer and the second one a button cell. Both cells have been operated with different fuel gas compositions at several temperatures. The fuel gas is mostly methane that is reformed on the fuel cell anode. The model therefore should include the flow field, species transport equations in the fuel channels and the anode, chemical reaction in the anode, energy transport and the electrochemistry at the electrolyte interfaces. Therefore, apart from the usual computational fluid dynamics, additional equations need to be solved for the chemical and electrochemical reactions.

In this section, several modelling approaches for SOFCs are discussed. They include the electric field and electrochemistry, as well as the chemistry of the reforming reaction and the diffusion in the porous electrodes.

3.2.1 Electrochemistry

The modelling approach of electrochemical reactions is discussed in this section. The equations used by default in the ANSYS add-on SOFC module with unresolved electrolyte are discussed, as these will be implemented in the model. Alternative models are discussed in Appendix A that could be used with User Defined Functions (UDFs) if needed.

Cell potential

The ideal (equilibrium) potential for a SOFC is given by the Nernst equation:

$$\phi_{ideal} = \phi_0 + \frac{RT}{2F} \ln \frac{p_{H_2} p_{O_2}^{\frac{1}{2}}}{p_{H_2O}} \tag{3.23}$$

Without load and leakage current this is equal to the open circuit voltage (OCV). The actual cell potential is influenced by various losses, which will become apparent when operating the fuel cell. This cell voltage becomes:

$$\phi_{cell} = \phi_{ideal} - \eta_{ele} - \eta_{act,a} - \eta_{act,c} - \eta_s \tag{3.24}$$

The several subtractions account for the losses from the solids (η_s), electrolyte (η_{ele}) and activation over potential in the electrodes (η_{act}). To calculate the cell potential, these losses need to be evaluated.

Current

Current distribution is calculated in analogy to heat conduction. The potential field is calculated on a conservation of charge base, yielding a laplacian:

$$\nabla \cdot i = 0 \tag{3.25}$$

$$i = -\sigma \nabla \phi \tag{3.26}$$

$$\nabla \cdot (\sigma \nabla \phi) = 0 \tag{3.27}$$

With σ the electric conductivity of the material and ϕ the potential. The resistivity of the electrodes and electrolyte can be calculated from:

$$R_{ohm} = \frac{l_a}{\sigma_a} + \frac{l_{ele}}{\sigma_{ele}} + \frac{l_c}{\sigma_c} \tag{3.28}$$

With σ the electric or ion conductivity and l the conductor length. With these equations, the transport of current and the ohmic losses in the solid parts and the electrolyte be calculated. Since the conductivity of the electrolyte is usually a strong function of the temperature, it is generally necessary to include an electrolyte conductivity model. Unfortunately the default electrolyte conductivity sub-model is invalid for the studied temperature range. Since the temperature is expected to be relatively constant it can be assumed negligible for the purpose of this study. If necessary an alternative equation can be supplied by the user in the *constit.c* file.

Activation over potential

The activation over potentials in the electrodes are usually approximated with the Butler-Volmer equation, derived from the reaction rate [17]:

$$i = i_{0eff}[e^{\frac{\alpha_a n \eta_{act} F}{RT}} - e^{-\frac{\alpha_c n \eta_{act} F}{RT}}] \tag{3.29}$$

In this equation, α refers to the transfer coefficient and n to the number of electrons involved in the reaction. Butler-Volmer can be solved in FLUENT using the Newton-Raphson method. Usually α is equal or very close to $\frac{1}{2}$ and the equation can be simplified to:

$$\eta_{act} = \frac{2RT}{nF} \sinh(\frac{i}{i_{0eff}}) \tag{3.30}$$

The over potentials depend on the gas phase composition. Therefor corrections to the reference current densities are made according to Costamagna et al. [7], giving the effective reference current density i_{0eff} from:

$$i_{0eff} = i_{0,ref}[\frac{X_j}{X_{j,ref}}]^{\gamma_j} \exp(-\frac{E_a}{RT}) \tag{3.31}$$

Where γ_j is a concentration exponent. In the model proposed by Costamagna this is 1 for water and hydrogen, and 0.25 for oxygen. FLUENT allows the cathode reference current density to be a function of temperature, but for reasons unclear to the author not for the anode reference current density. The two parameters adopted by the SOFC, A and B, are respectively assigned as:

$$A = i_{0,cathode}$$

$$B = \frac{R}{E_{A,cathode}}$$

With $i_{0,cathode}$ the reference cathode current density, R the universal gas constant (J/mol·K) and $E_{A,cathode}$ the activation energy of the electrochemical reaction.

Mass and heat source

Once the current distribution is calculated, this can be used to calculate the depletion of oxygen on the cathode side, and the conversion of hydrogen to water on the anode side. From that, the species sources become:

$$(S_{i,r})_{ele} = \frac{A_{ele} i_{cell}}{nF} \tag{3.32}$$

Here A_{ele} refers to the cell electrolyte interface and i_{cell} to the current density in that cell. Consequently the amount of heat produced resulting from the electrochemical reaction is hooked to the energy source:

$$S_{h,ele} = A_{ele} i_{cell} (\frac{\Delta H_{elec}}{2F} - \phi_{cell}) \tag{3.33}$$

Where ΔH_{elec} is change in enthalpy of the specific electrochemical reaction and ϕ_{cell} is the cell voltage calculated from Equation (3.24).

CO chemistry

If CO is present on the anode of a fuel cell, it can be electrochemically oxidised to CO_2. From the implemented overal reaction in FLUENT:

$$3H_2 + CO + 2O_2 \Rightarrow 3H_2O + CO_2$$

The Nernst equation then changes to:

$$\phi_{ideal} = \phi_0 + \frac{RT}{2F} \ln \frac{p^3_{H_2} p_{CO} p^2_{O_2}}{p^3_{H_2O} p_{CO_2}} \tag{3.34}$$

Of course a CO_2 source and a CO sink have to be assigned. A popular (but simplified) way to do this is by defining a split factor, based on the species mole fraction X:

$$f_{split} = \frac{X_{H_2}}{X_{H_2} + X_{CO}} \tag{3.35}$$

By default it is also modelled like this in ANSYS, although a different split factor can be defined by the user. The FLUENT manual reports that species sources and sinks are weighted with this split factor, and the reaction becomes:

$$f_{split} H_2 + (1 - f_{split}) CO + \frac{1}{2} O_2 \Rightarrow f_{split} H_2O + (1 - f_{split}) CO_2 \tag{3.36}$$

Which shows why this is a simplified way. Electrochemical oxidation of carbon monoxide is generally not considered in this study.

3.2.2 Methane Steam Reforming

The main interest of this study is the coupling between the chemical reactions, methane steam reforming and water gas shift, and fuel cell operation. Therefore the modelling of these chemical reactions, especially the reforming reaction, is most important in the modelling.

In the model, the SOFC will be fuelled with methane, which is converted to hydrogen and carbon monoxide at the anode, with the so called steam reforming reaction:

$$CH_4 + H_2O \Leftrightarrow 3H_2 + CO$$

This reaction is usually followed by the Water Gas Shift reaction, yielding additional hydrogen by the reaction:

$$CO + H_2O \Leftrightarrow H_2 + CO_2$$

In FLUENT, the default volumetric rate equation is of the power law type. Far from equilibrium it is usually safe to assume this reaction only depends on the reactants partial pressures. For methane steam reforming, the reaction then becomes:

$$r_{MSR} = k_0 \cdot \rho_{CH_4}^{\alpha} \cdot \rho_{H_2O}^{\beta} \cdot exp(\frac{-E_A}{RT}) \tag{3.37}$$

The water gas shift reaction can be implemented in similar fashion:

$$r_{WGS} = k_0 \cdot \rho_{CO}^{\alpha} \cdot \rho_{H_2O}^{\beta} \cdot exp(\frac{-E_A}{RT}) \tag{3.38}$$

It is expected that the water gas shift reaction is close to equilibrium for the experimental conditions. Therefore, backward reactions should probably be included as well. The impact of this assumption needs to be evaluated with the modelling results.

In this study Langmuir-Hinshelwood kinetics are fitted to the experimental data in Chapter 2. Although FLUENT exhibits a number of more detailed reaction models, alternative volumetric rate equations can only be implemented using UDFs. This is done for the obtained Langmuir-Hinshelwood kinetics. The code can be found in Appendix F.

3.2.3 Species transport in Solid Oxide Fuel Cells

The transport of species in SOFCs is essential to model their behaviour, and care should be taken to implement realistic transport equations. As diffusion is an important mechanism of transport in fuel cells, the specification of the diffusion constants is thus of vital importance. In addition, the diffusion is limited in porous media for which the equations should be adjusted. There are several ways to do this. The complications of these methods vary, as do their accuracies.

Several researchers have been investigating diffusion in porous zones, some particularly for fuel cell applications. Some models worth mentioning are discussed in the Appendix A. In the current model, a default simplified model is used that corrects the diffusion constants with the porosity and the tortuosity of the electrode:

$$D_{ij,eff} = \frac{\varepsilon}{\iota^2} D_{ij} \tag{3.39}$$

Note that ι is usually referred to as the *tortuosity* and ι^2 as the *tortuosity factor*. A common definition of the tortuosity is the length of the curve over the distance between the ends of the curve:

$$\iota = \frac{L_c}{R_c} \tag{3.40}$$

Where L_c refers to arc length of the curve and R_c to distance between the ends of the curve.

Chapter 4

Development of the Solid Oxide Fuel Cell models

To solve these equations discussed in Chapter 3 a CFD method is exploited. Therefore the problem is divided into finite volumes, generally referred to as the grid or the mesh. The meshing of the geometries and the implementation of the equations are discussed in this chapter.

The model is first developed on the square geometry. The objective is to determine the calculation domain and develop an appropriate mesh for this test setup. Meshes have been developed for the full square cell and for a single channel. In the mesh development, a stepwise approach is taken, optimizing both mesh type and mesh size. Since the meshes were developed before the Langmuir-Hinshelwood rate equation was proposed, they are optimised with a Power Law rate equation.

With the mesh obtained, the implementation of the model in FLUENT is verified by checking the balances. The button cell model was built in similar fashion to the square cell.

4.1 Development of the Square Cell model

The square setup has a fuel supply system which distributes the fuel over 22 fuel channels. The cell, with the current collector pressed on the electrodes, is put on top of these fuel channels with the anode faced down. A picture of the anode side fuel distributing system is given in Figure 4.1. As we are purely interested in the anode side of the cell, we will assume a simplified flow of cathode air on the top side of the cell. This model is based on the FLUENT SOFC add-on module with unresolved electrolyte. Therefore the electrolyte is in this case not present in the geometry but simply modelled as a *coupled wall*. A *jump condition* is thus applied to the properties on the two sides of the electrolyte.

4.1.1 Mesh development

The full geometry that needs to be meshed is shown in Figure 4.1. This geometry was first meshed in a coarse way to proof the principle of the model and identify possible problems in the geometry. From this initial mesh it was concluded that:

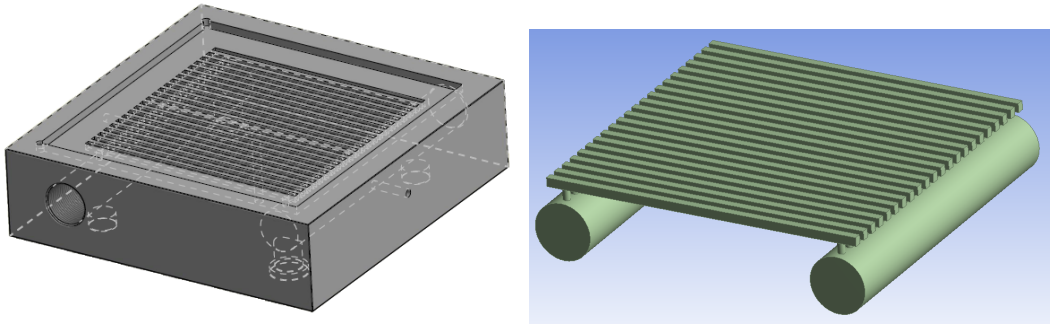

(a) CAD model (b) FLUENT model

Figure 4.1: A CAD model of the fuel distributor, re-drawn from measurements (4.1a) and the fuel channels drawn for the FLUENT model (4.1b). The anode, a 9 x 9 cm and 35 μm thick square layer, is modelled on top of these channels.

- The in- and outflow regions should be extended to ensure fully developed inflow and outflow in relevant regions and prevent backflow;
- In the experiment, the mass flow seems high enough to assume constant mass flow in all channels: A single channel model whit symmetry boundary conditions might therefore be a good representation of the full geometry. This has to be validated;
- The Green-Gaus node based solver shows the best convergence, but seems unable to handle the porous formulation based on the physical velocity and tends to be unstable with the diffusion energy source enabled. The Green-Gaus cell based solver does not exhibit these problems;
- Unstructured tetrahedron mesh shows best convergence in the round fuel channel areas, especially when the flow turns around corners, whereas structured quads give the best results in the anode area;
- The mesh on both sides of the electrolyte needs to be conformal (the mesh has to match). Otherwise a small error in current density may arise and worse, the electrochemical source seems unable to handle it.

These observations are used to develop the mesh for this geometry. It is because of the conclusions above that for further mesh development only a single channel is meshed with symmetry boundary conditions on the sides of the anode and air channel.

Mesh type

The single channel geometry can be seen in Figure 4.2. As was concluded from the full scale mesh, tetrahedrons should be used in the fuel channel and quads in the anode and cathode. From the resulting mesh, several refinements were made to monitor the improvement of the solution and identify poorly meshed regions.

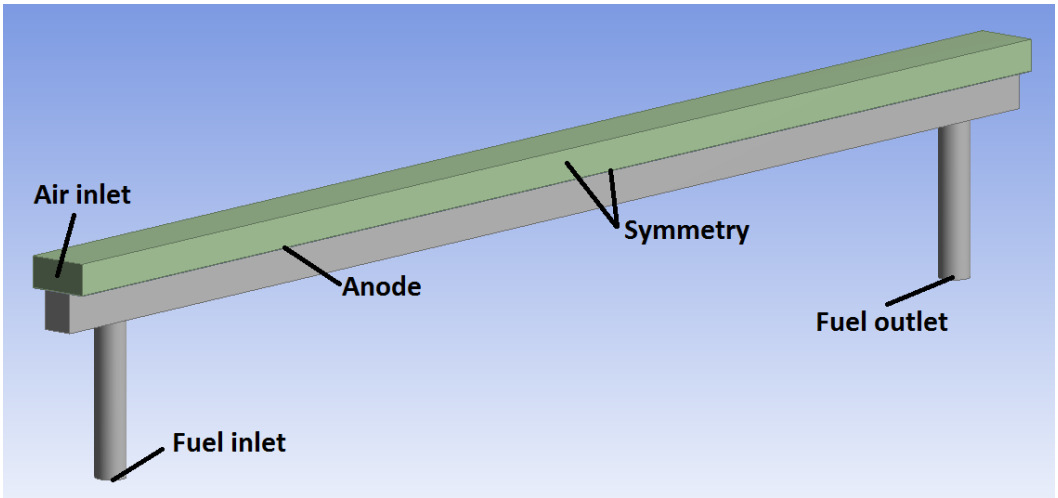

Figure 4.2: Geometry for a single channel: symmetry boundary conditions are used at the sides and in- and outlet are extended. The influence of the fuel distributer is neglected.

To test the meshes, a complete model of the fuel cell with both chemical and electrochemical reactions is evaluated, based on model input parameters as used by Boksteen [61], boundary conditions and the chemical reaction mechanism proposed by Fan [52] which are summarised in Table 4.1. From these meshes the following is concluded:

- The transition from tetrahedron mesh to quad mesh is not very smooth, even with mapped surface mesh on the interface. This results in unexpected wiggles in the solution.
- Structured (non-tetrahedron) mesh in the fuel channel is numerically inconvenient as a large number of grid cells is required to get a converging solution.
- The highest gradient are observed in the corners of the fuel channels, where the anode is no longer directly connected to the fuel channel and species have to diffuse sideways in the anode.

It is therefore decided to add an additional transition region in the top of the fuel channel, where the mesh goes from unstructured tetrahedron to structured quads with a mapped surface mesh on the interface. It is made sure that the top of the transition region matches with the anode mesh and the bottom with the fuel channel mesh.

In Figure 4.3 it can be seen that this shows an excellent improvement, even if a coarser mesh is used. The results are plotted on lines in the middle of the anode in two directions, referred to as x and z. These lines are visualised in Figure 4.4. They are selected because initial results show the gradients are highest in this region and the solution is thus most sensitive to the mesh quality in this area. If the model is able to predict the distribution of species, temperature and reaction rates in these parts of the anode, it can safely be assumed that the mesh is fine enough in other parts of the geometry.

Table 4.1: Table of the model input parameters, including electrochemical and chemical parameters, material properties and boundary conditions.

Anode		
Porosity ε	m^3/m^3	0.35
Tortuosity ι^2	m^2/m^2	5
Viscous drag K	$1/m^2$	1e8
Solid density ρ	kg/m^3	7760
Heat capacity c_p	J/kg K	600
Thermal cond. λ	W/m K	6
Electrical cond. δ	1/Ohm m	30300

Electrolyte		
Density ρ	kg/m^3	6000
Heat capacity c_p	J/kg K	400
Thermal cond. λ	W/m K	2.7

Electrochemistry		
Anode i_0	A/m^2	7460
Cathode i_0	A/m^2	1009
Reference [H_2]	mol/mol	1
Reference [H_2O]	mol/mol	1
Reference [O_2]	mol/mol	1
γ_{H_2}	-	1
γ_{H_2O}	-	1
γ_{O_2}	-	0.25
$i_{0,c}$	-	7e8
R/E_a	K^{-1}	-14434

Boundary		
$\dot{m}_{fuel}$	kg/s	3.679e-7
X_{m,H_2O}	kg/kg	0.5491
X_{m,CH_4}	kg/kg	0.2108
X_{m,H_2}	kg/kg	0.0071
$\dot{m}_{air}$	kg/s	1.5e-6
X_{m,O_2}	kg/kg	0.2
T_{inlet}	K	1023
T_{walls}	K	1023
I_{cell}	A	0.3682

Reforming		
k_0	$(kmol/m^3)^{0.2}$ s	9e5
E_a	J/kmol	6.4e7
α_{CH_4}	-	0.78
β_{H_2O}	-	-0.02

Shift		
k_0	$(kmol/m^3)^{-1}$ s	1.626e7
E_a	J/kmol	6.713e7
α_{CO}	-	1
β_{H_2O}	-	1

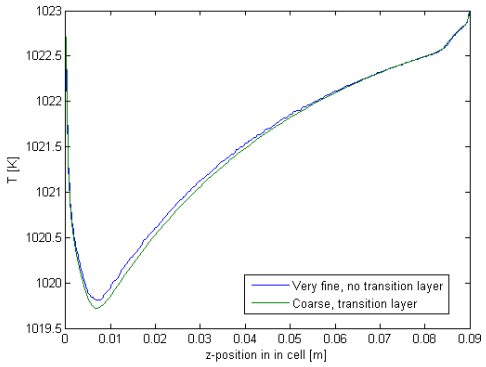

(a) Temperature, flow direction

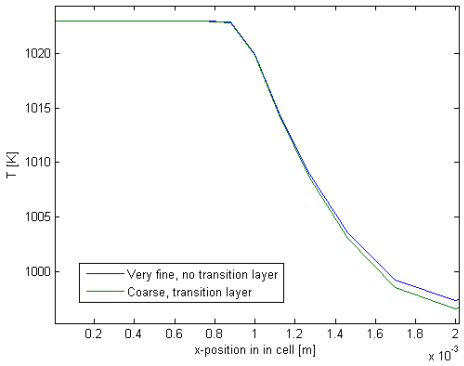

(b) Temperature, sideways

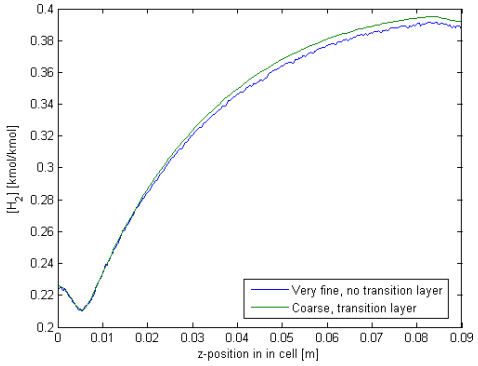

(c) Hydrogen, flow direction

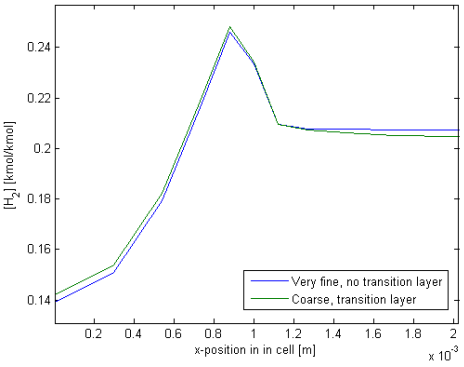

(d) Hydrogen, sideways

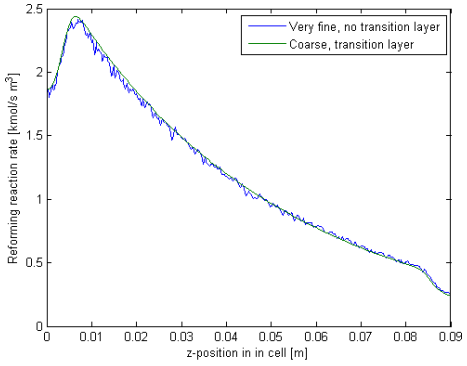

(e) Reforming rate, flow direction

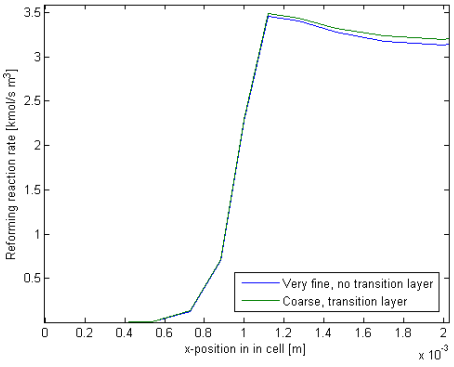

(f) Reforming, sideways

Figure 4.3: Result of initial mesh selection. The results with a very fine mesh without transition layer is compared to those on a coarse mesh with transition layer. Therefore temperature, hydrogen concentration and reforming reaction rate are plotted in flow direction in the middle of the anode in the corner and in sideways direction, 1cm in flow direction. The lines are displayed in Figure 4.4.

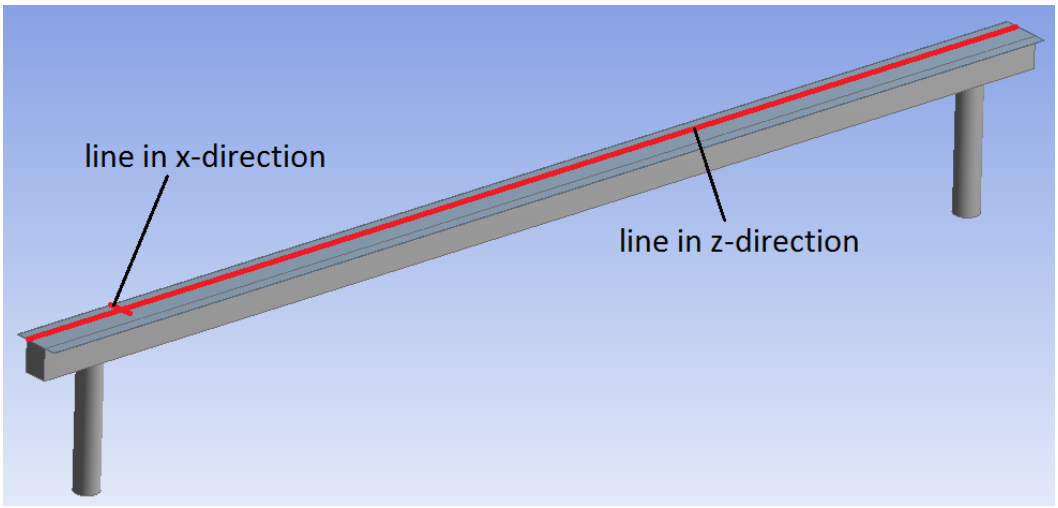

Figure 4.4: Lines on which results are plotted for the single channel meshes. Both lines are in the middle of the anode height and selected in regions with highest gradients.

Mesh refinement

Again a number of meshes is examined, now with the focus on the required number of divisions. A *base mesh* is selected based on the results obtained in the mesh selection procedure. It has the discussed transition layer and a cell growth rate is applied with smaller cells towards the corners in the sides of the fuel channel as high gradients are expected in that region. The growth rate can help to limit the number of grid cells required because it allows the mesh to be coarser in areas with relatively small gradients.

This base mesh is refined in the width (X), height (Y) and flow (Z) direction respectively. The mesh refinements focus more on the anode area, as this is the area of interest and more importantly, the area with all the chemical and electrochemical reactions. The mesh size for the base mesh and the refinements can be found in Table 4.2. In Figure 4.5 several solutions on the mesh are plotted in several areas and directions. The distributions of the temperature, hydrogen concentration and methane reforming reaction rate are plotted on the lines in Figure 4.4.

The plots reveal that further refinement in the Y and Z direction does not change the solution at all, apart from a minor change in the very unimportant beginning of the channel. Further refinement in the X direction does however have a significant influence on the results, especially in the corner area where the highest gradients are present. It is thus decided that further refinement in Y and Z direction superfluous. The refinement in X direction has to be further investigated.

Mesh optimisation

To optimise the mesh a large number of refinements in X direction is evaluated, of which four will be discussed here. The mesh size for these refinements can also be found in Table 4.2. The number of divisions is increased in steps. For all meshes a

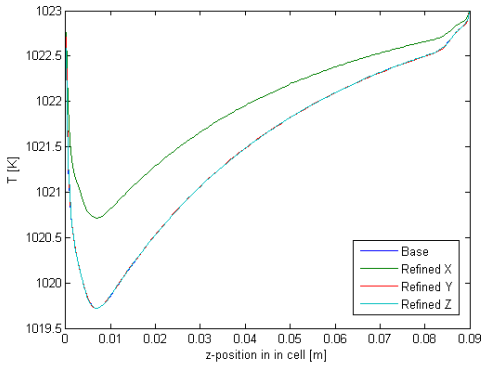

(a) Temperature, flow direction

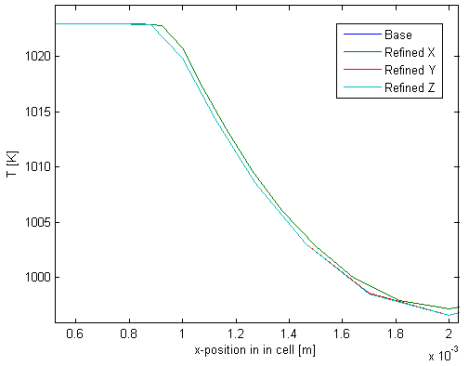

(b) Temperature, sideways

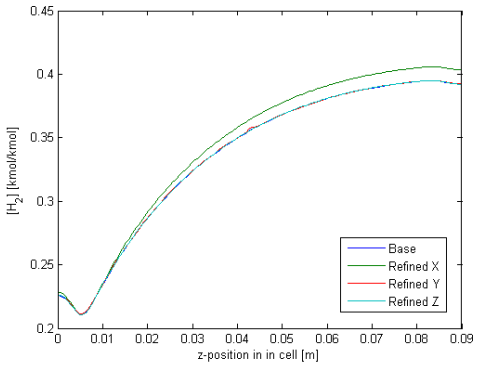

(c) Hydrogen, flow direction

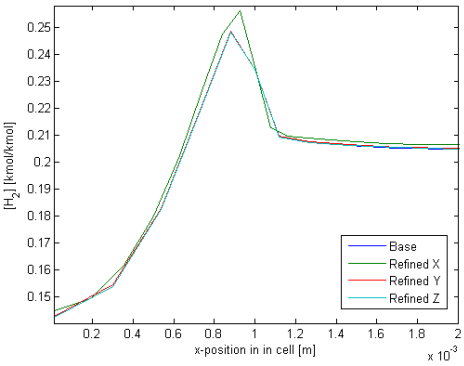

(d) Hydrogen, sideways

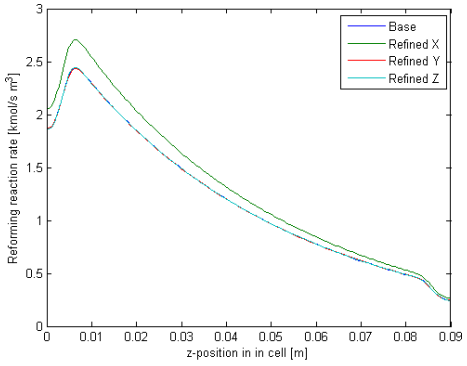

(e) Reforming rate, flow direction

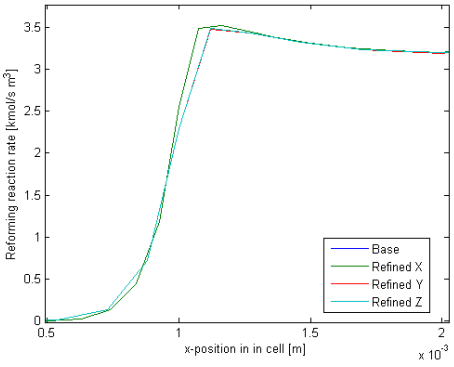

(f) Reforming, sideways

Figure 4.5: Result of initial mesh refinement with the same plots of the same variables and on the same lines as in Figure 4.3.

Table 4.2: Overview of the average mesh size in the mesh optimization. The value corresponds to the mesh size ([m]) in the specified direction. Since a bias factor is defined in x-direction, the average mesh size is specified for this direction.

Spatial direction	Base	First refinement			Second refinement			
		X	Y	Z	X1	X2	X3	X4
x	2e-4	1.67e-4			1.33e-4	1e-4	8.33e-5	7.41e-5
y	5e-6		3.5e-6					
z	6e-4			3.6e-4				
	Bias factor x = 2.5				Bias factor x = 5			

constant growth rate is used towards the corner of the fuel channel. The number of grid cells varies from 84638 for the base case to 218105 for the most refined single channel mesh. Results of this optimisation are plotted in Figure 4.6.

From this optimisation it is seen that the most refined version shows the smoothest curves in x direction. The general shape of the solution does however not change. With the first refinement a rather large change in the results can be seen. The solution is less sensitive to further refinement. The change seems to converge and there is almost no difference between the last two meshes. It should also be mentioned that these changes are only apparent in these very sensitive regions. Plots in the centre of the anode for example, show no noticeable difference from the first refinement on. As the computational requirements quickly increase with the refinements, especially for the full geometry it is decided to use the first refined mesh. This mesh is displayed in Figure 4.7.

4.1.2 Checking balances

Checking the balances is an essential way to verify the correct implementation of a model. Programming errors, software bugs, and incorrect equations that might give large errors in the solution can easily appear from such a balance check. Checking the balances also ensures that the FLUENT output is interpreted in the right way. The balances checked in Table 4.3 are that of mass, heat, energy and species.

From the balances we can see that the residuals appear small and the model seems to be implemented in a correct way. It is also found that although FLUENT uses the actual porous anode volume as the reaction volume if the physical velocity formulation is used, the default integral output multiplies with the total cell volume and not just the porous volume. This is easily corrected by multiplication with the porosity, but is sometimes confusing judging from commentary on the module on internet fora.

With the model derived by Fan [52] a sensitivity analysis was done. Since the model was dropped later and replaced by the Langmuir-Hinshelwood type this is only useful to investigate the sensitivity to the electrochemical parameters. The interested reader can find the sensitivity analysis in Table C.1.

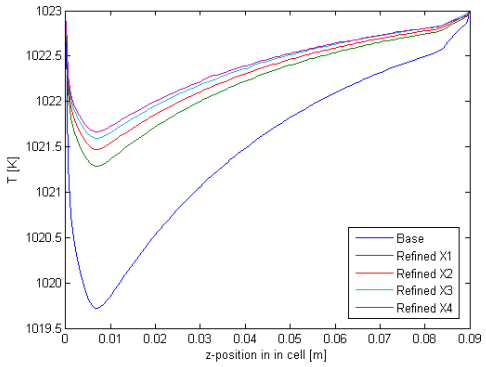

(a) Temperature, flow direction

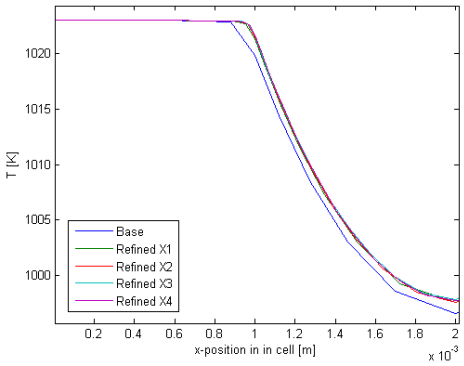

(b) Temperature, sideways

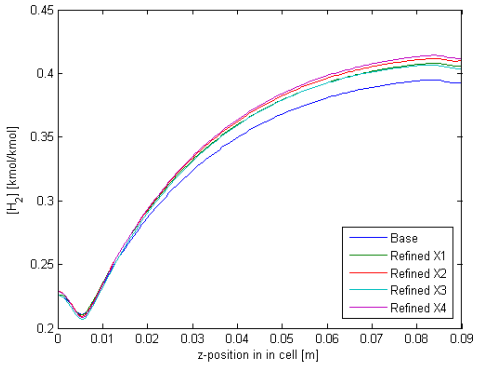

(c) Hydrogen, flow direction

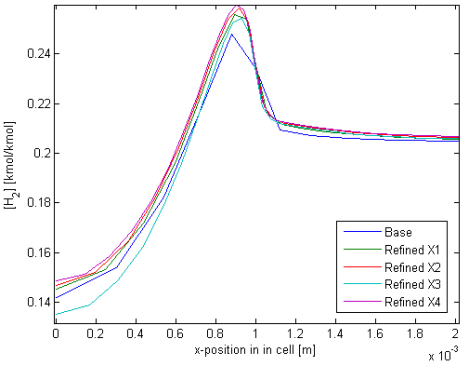

(d) Hydrogen, sideways

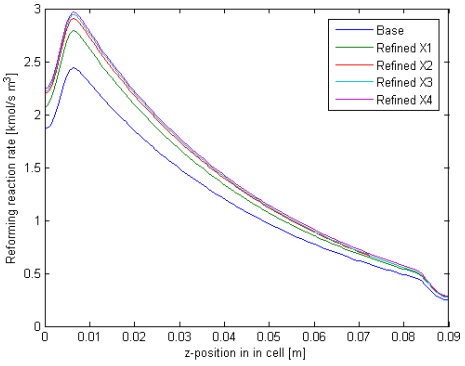

(e) Reforming rate, flow direction

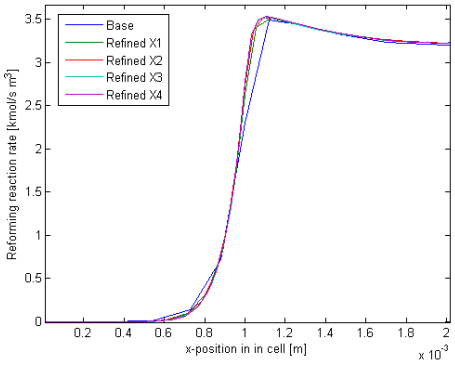

(f) Reforming, sideways

Figure 4.6: Result of the second mesh refinement. The same lines are plotted, this time for three refinements in sideways direction. The first refined mesh (Refined X1) is used for further calculations.

Table 4.3: Table of the balances for the model. The residuals of the energy seem to be rather large, however scaled to the total mass balance they are reasonable, as are the residuals of mass and species.

Mass [kg/s]						**Residual**
$\dot{m}_{fuel,in}$	$\dot{m}_{fuel,out}$	$\dot{m}_{air,in}$	$\dot{m}_{air,out}$			
3.679e-7	-3.984e-7	1.500e-6	-1.469e-6			7.100e-13
Heat [W]						
$\dot{Q}_{inlet}$	$\dot{Q}_{outlet}$	$\dot{Q}_{wall}$	$\dot{Q}_{reactions}$	$\dot{Q}_{ele.ch.}$	$\dot{Q}_{ohmic}$	
1.763	-1.835	0.794	-0.870	0.151	1.054e-4	2.961e-3
Enthalpy [W]						
$\dot{E}_{in,fuel}$	$\dot{E}_{out,fuel}$	$\dot{E}_{in,air}$	$\dot{E}_{out,air}$	$\dot{E}_{Electricity}$	$\dot{Q}_{wall}$	
-2.483	1.974	1.1719	-1.149	-0.311	0.794	-3.276e-3
Species [kg/s]						
	$\dot{m}_{in}$	$\dot{m}_{out}$	S_{MSR}	S_{WGS}	$S_{ele.ch.}$	
H_2	2.612e-9	-2.474e-8	2.549e-8	2.849e-10	-3.816e-9	-1.750e-10
H_2O	2.020e-7	-1.573e-7	-7.647e-8	-2.564e-9	3.435e-8	3.505e-11
O_2	3.000e-7	-2.695e-7	0	0	-3.053e-8	-1.440e-12
CH_4	7.755e-8	-9.186e-9	-6.797e-8	0	0	3.973e-10
CO	0	-1.140e-7	1.189e-7	-3.989e-9	0	1.007e-9
CO_2	0	-6.227e-9	0	6.268e-9	0	4.124e-11

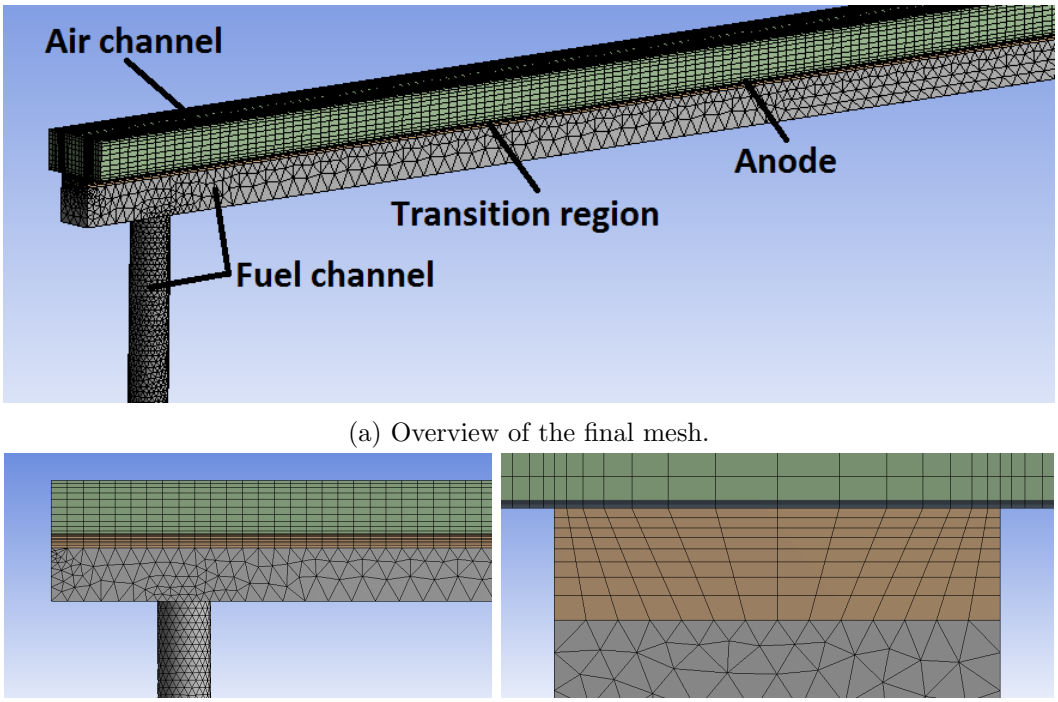

(a) Overview of the final mesh.

(b) Side view of the final mesh.

(c) Front view of the final mesh.

Figure 4.7: The mesh used in the simulation. In the overview of the mesh some zones are indicated (a). Some close-ups on the mesh from the side (b) and front (c) are also shown. The transition region (orange) connects the triangular mesh of the rest of the fuel channel (grey) with the quads meshed anode (blue). The interface between the anode and the air channel (green) is meshed conformal.

4.1.3 Verifying the single channel assumption

For mesh optimisation and model testing it was assumed that the model of the full cell can be represented with a model of a single channel only, using symmetry boundary conditions on the sides, without influencing the solution too much. This assumption has to be verified. Therefore a full fuel channel model is made using the original geometry and the mesh that was selected for the single channel model. In Figure 4.8 plots are shown of the single channel model, a channel from the middle of the full setup and for a channel on the side of the full cell. In addition, in Figure 4.9 typical surface plots of the full cell and single channel models are shown for comparison.

From the plots we can see that there is virtually no difference between the single channel model and a channel in the middle of the full cell. We can see that there is a difference for the channels on the side of the cell, as the geometry is a little different and there is a wall boundary on the left. This effect only effects the two channels on the side (out of the 22) and it is therefore safe to assume that the single channel assumption has little effect on the final results. The single channel model is therefore a good representation of the whole geometry. Simulations on the single channel give sufficient insight in the physics involved in the full cell.

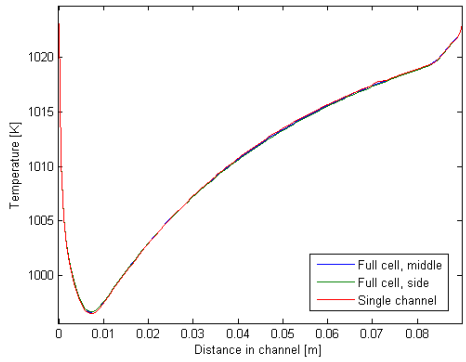

(a) Temperature, flow direction

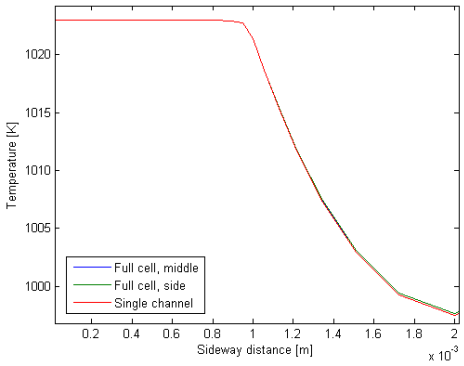

(b) Temperature, sideways

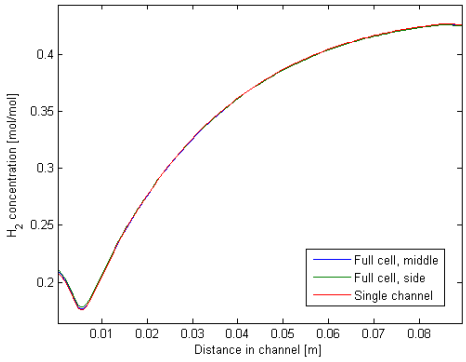

(c) Hydrogen, flow direction

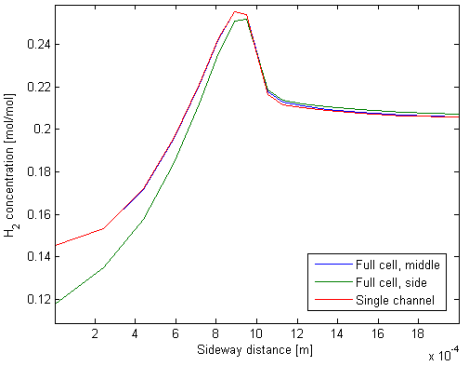

(d) Hydrogen, sideways

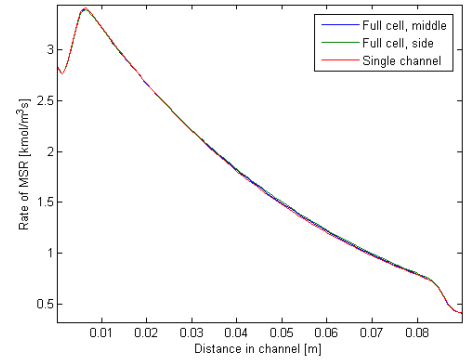

(e) Reforming rate, flow direction

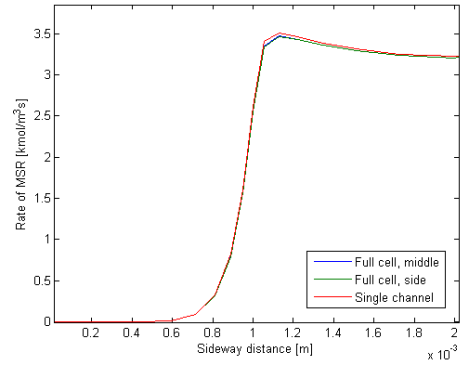

(f) Reforming rate, sideways

Figure 4.8: Result of the comparison between full and single channel geometry. They are virtually equal, except for a decrease in hydrogen concentration towards the side of the full fuel cell.

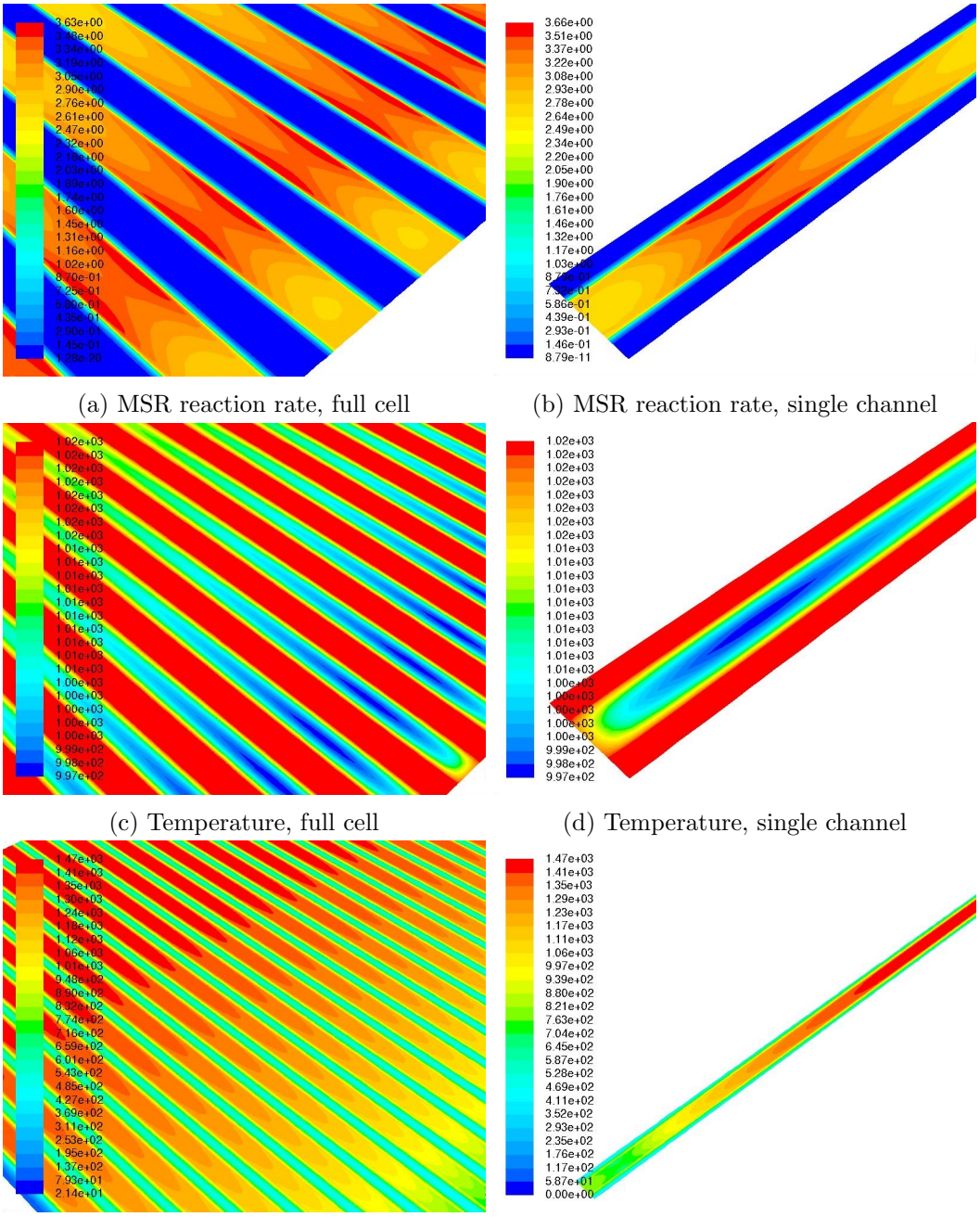

(a) MSR reaction rate, full cell

(b) MSR reaction rate, single channel

(c) Temperature, full cell

(d) Temperature, single channel

(e) Current density, full cell

(f) Current density, single channel

Figure 4.9: Typical results: Methane reforming reaction rate, temperature and current density on the electrolyte interface for the full cell and single channel model.

It should be noted however that the single channel assumption is only verified for the boundary conditions used in this work. It is expected and confirmed by modelling that for lower mass flow rates back diffusion to the fuel distributor is possible, resulting in a non-symmetrical solution, spatial gradients in species concentration and temperature and changes in fuel cell performance.

4.2 Development of the Button Cell model

Geometrically, the button cell setup is simpler to model compared to the square cell, which has a complicated fuel distribution system. The cell has a simple round (button) shape and is mounted on a fuel system, as can be seen in Figure 4.10a. This fuel system supplies fuel via the inner line. Flue gas leaves the setup via the outer tube. The whole setup is placed in a furnace to control the temperature in the system and the cathode is exposed to the air in the furnace.

4.2.1 Mesh development

The problem is axisymmetric, and could therefore probably be represented in a simplified two dimensional computational domain. This would save a lot of computational cost, but unfortunately the FLUENT SOFC module can only be loaded to three dimensional problems. It is however decided to model only half of the cell and use a symmetric boundary condition in the middle to save at least half of the computational cost. Theoretically, a very small slice of the button cell would also do, but it will become harder to obtain a mesh with low aspect ratios.

Because the SOFC module is used, the cathode side has to be modelled too, as FLUENT needs to solve cathode over potentials as well. Since natural convection is numerically unattractive to model and the cathode side is of limited interest in this study, the geometry of the anode is simply mirrored to the cathode side and an airflow is forced through the tubes.

If the assumption is made that heat transfer effects can be ignored at the inflow and outflow region because it has a constant temperature, there is no need to include the solid material of the tubes in the calculation domain.

Mesh type

As the solution is expected to be axisymmetric, it is assumed that the best results are obtained if:

- A conformal, hexagonal mesh is used in tangential and radial direction. The mesh is thus the same at all axial cross sections;
- Towards the centre, some transition is needed to avoid cells with high aspect ratios. Unfortunately the mesh therefore becomes somewhat unstructured in the anode;
- The mesh is also refined towards the outer and inner tube walls with a scaling factor because a no slip boundary condition is used and the flow speed is expected to change rapidly towards the boundary;

- In axial direction the mesh is somewhat refined towards the inlet section because the flow is developing here;
- The mesh in axial direction is refined significantly towards the anode, because large temperature and concentration gradients are expected in this region. The mesh is finest in the anode itself.

The base mesh is obtained with the ANSYS mesher, using advanced meshing algorithms to obtain a conformal mesh in radial and tangential direction while keeping aspect ratios low. Initial simulations show good convergence and smooth profiles.

Mesh optimisation

To see whether the proposed mesh is fine enough to model the physical phenomena in the button cell correctly, several mesh refinements are made to check the influence of the mesh on the simulation results. Since the base mesh is already quite fine, the mesh is coarsened into radial, tangential and axial direction. In addition, a refinement of the anode is studied by increasing the number of anode layers, as the anode is the region of interest and the gradients are expected to be highest.

For the evaluation of the meshes, a typical case is modelled. The experimental mass flows are used, and the temperature is 1023 K. The electrochemical parameters are similar to the ones used for the square cell simulation and the current density is 1000 A/m^2. For the reforming a simple first order in methane model is implemented with an activation energy of 64 kJ/mol and a rate constant of 7.5e6 s^{-1}. With these parameters, the methane conversion is about 19.1%.

As was done for the square cell, the effect on the distribution of temperature, hydrogen concentration and reforming reaction rate are studied. Since the solutions are axisymmetric two lines are plotted: one in axial direction from the fuel tube to the electrolyte and one in radial direction from the centre of the anode to the tube wall. These lines are plotted in Figure 4.10b. The results are plotted in Figure 4.11.

It is clear that coarsening of the mesh in tangential and radial direction does not influence the solution, as does the refinement of the anode. The coarsening of the mesh in axial direction has a slight influence on the distributions in the test set up. This change is however very small, while the mesh size is about two times bigger.

To be sure that this has no severe influence on the obtained solutions, several refinements in axial direction are studied. It can be seen from the solution that the gradients are highest at the interface between anode and fuel line. The mesh size in that region will therefore be most important. In the base case, the mesh size of the first gas layer is 36 μm. In the coarsened case this was 63 μm. To further investigate the influence of the size of this first layer two additional meshes are made, one with a first layer size of 25 μm and one where this layer is only 13 μm. The results of this second mesh study are shown in Figure 4.12.

From the second mesh refinement we can see that the size of the grid cells near to the anode has an influence on the obtained solution. Coarsening the base mesh has a significant influence on the obtained result. Refining the mesh further has some influence as well. However, even with a mesh size that is about three times finer, the result does not change more than $\sim 1\%$.

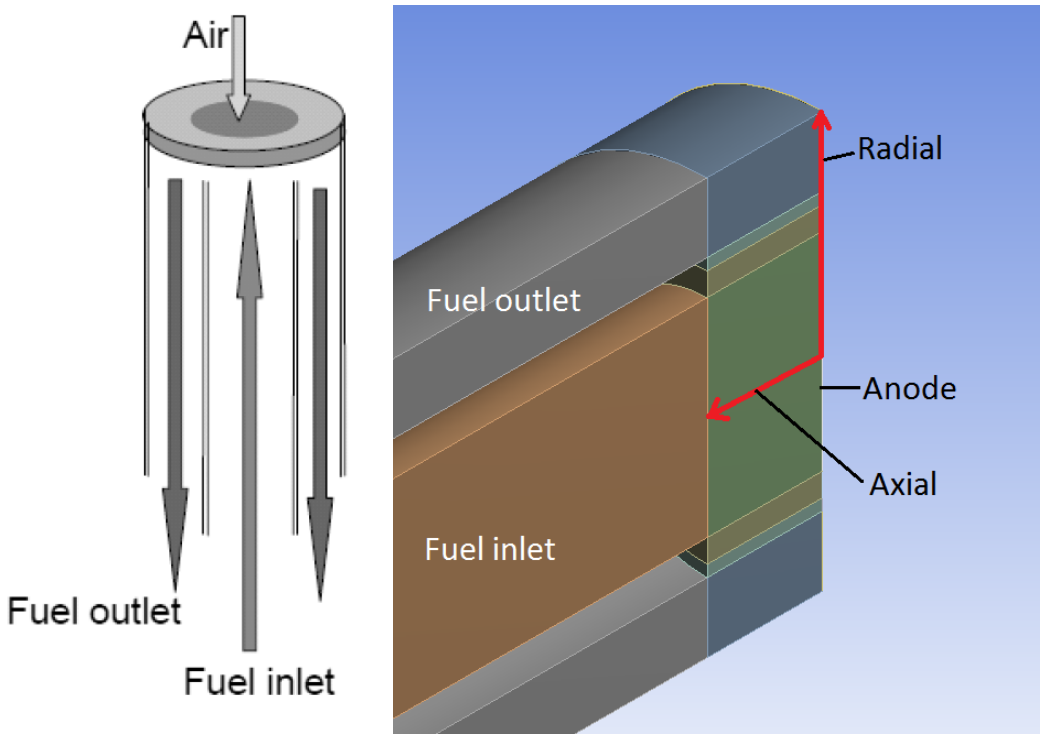

(a) Button cell setup (b) Modelled geometry of the fuel side

Figure 4.10: An overview of the button cell setup (4.10a) and fuel side of the button cell model (4.10b). For meshing purposes the fuel channel is divided in sections to which the different colours refer. The variables are potted along the red lines, referred to as the radial and the axial line.

Like with the square cell, there is a trade of between numerical accuracy and computational time. For the calculations in this study the base mesh is considered to be of sufficient quality, since the deviation from the results on a very fine grid is small. The mesh is capable of predicting correlations in the set-up with reasonable accuracy and computational time.

4.2.2 Geometrical uncertainty

A problem in the modelling of the button cell, is that the exact distance from the fuel supply tube to the anode is unknown. To test the influence of this uncertainty, the distance between the tube and the anode is varied in range that could have been used in the experiment. The other parameters in the model are similar to the ones used for the mesh optimisation. Three distances are evaluated: 7.5, 5 and 2.5 mm. The influence of this distance on the solution is evaluated by comparing the flow field and methane distributions in the setup, and by plotting the distributions of temperature, hydrogen concentration and MSR reforming reaction rate, an approach also used in the mesh comparison.

To get an idea of the main influence of the inlet distance, the magnitude of the velocity in the middle of the setup is displayed in Figure 4.14. On the right in the

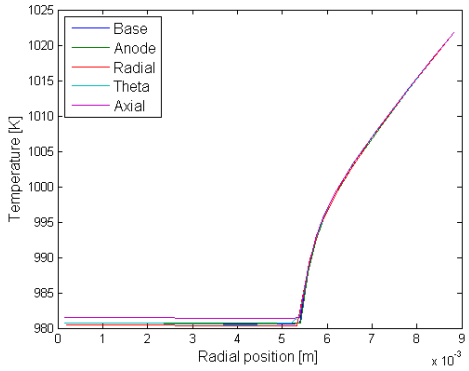

(a) Temperature, radial direction

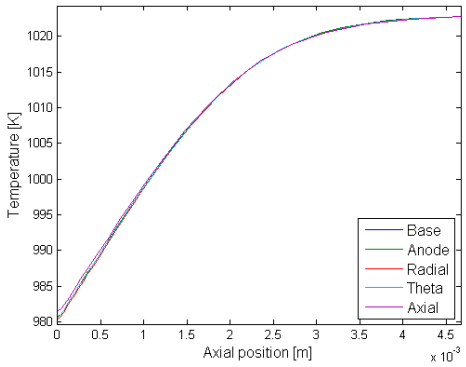

(b) Temperature, axial direction

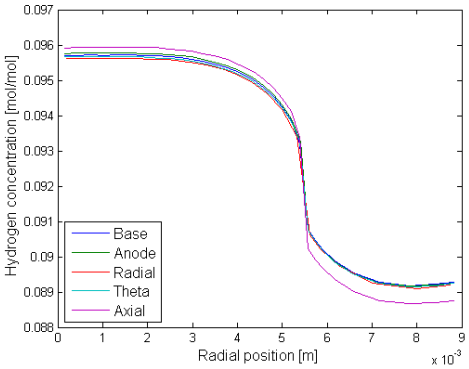

(c) Hydrogen, radial direction

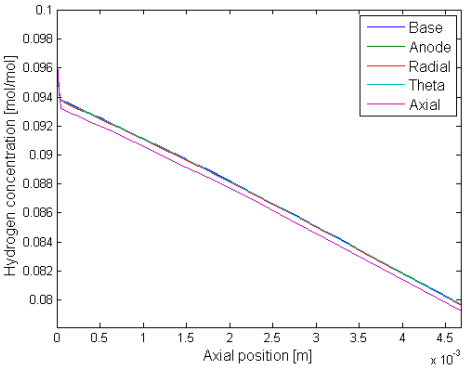

(d) Hydrogen, axial direction

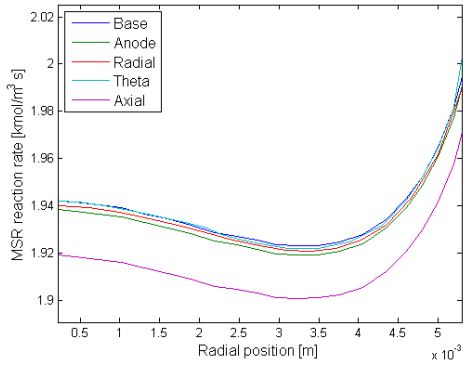

(e) MSR rate, radial direction (anode)

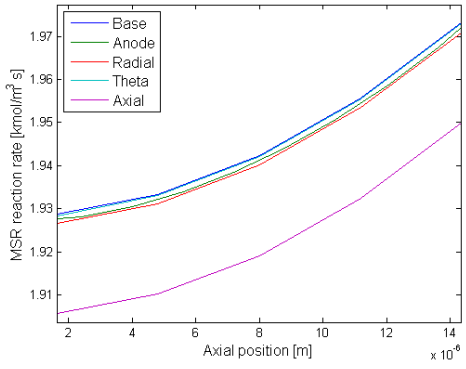

(f) MSR rate, axial direction (anode)

Figure 4.11: Result of the mesh refinement. Spatial distribution of temperature, hydrogen concentration and MSR reaction rate in radial and axial direction. The MSR reaction rate is only plotted in the anode.

same figure, the resulting methane concentration profile is shown. Note that the scaling in the four cases is a little bit different. From the velocity magnitude it becomes clear that the distance has a severe influence on the flow velocity in the gap. This does however not result in more by-passing of fuel, as becomes clear from

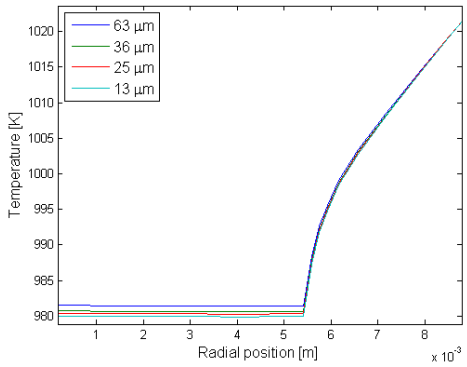

(a) Temperature, radial direction

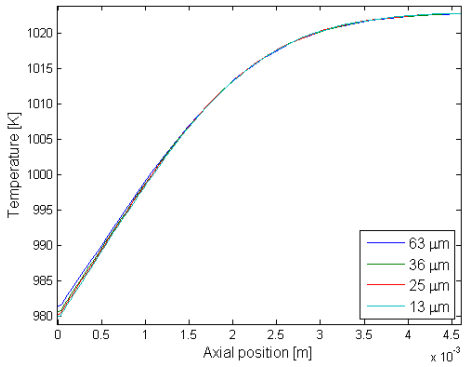

(b) Temperature, axial direction

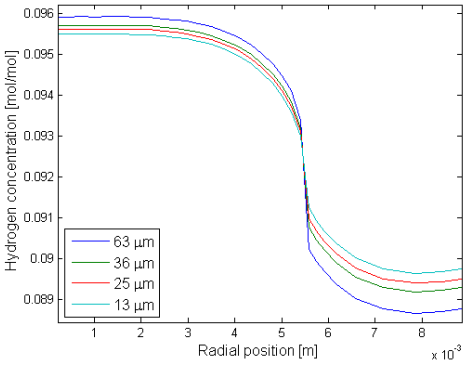

(c) Hydrogen, radial direction

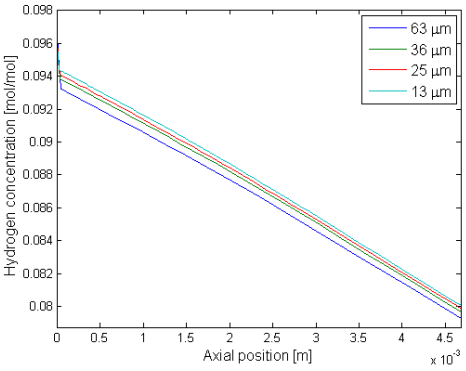

(d) Hydrogen, axial direction

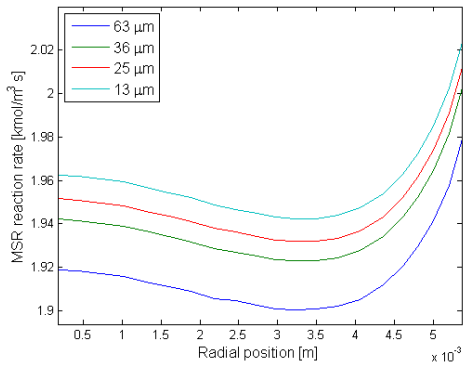

(e) MSR rate, radial direction (anode)

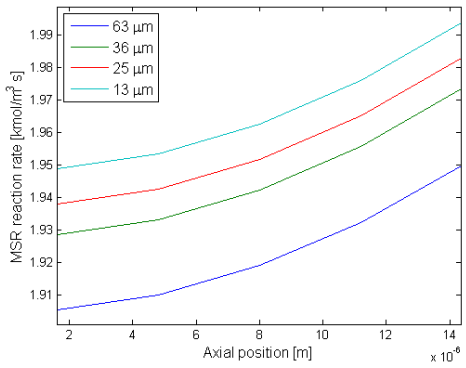

(f) MSR rate, axial direction (anode)

Figure 4.12: Result of the mesh refinements in axial direction. The refinements are quantified by the mesh size of the first layer on the anode interface, which changes from 63 μm for the coarse mesh to 13 μm for the finest mesh.

the methane distribution.

This shows that at the flow velocities under the tested conditions, diffusion of species is the dominant species transport mechanism. With the tube closer to the anode, the fuel cannot diffuse sideways and more fuel diffuses into the anode. This

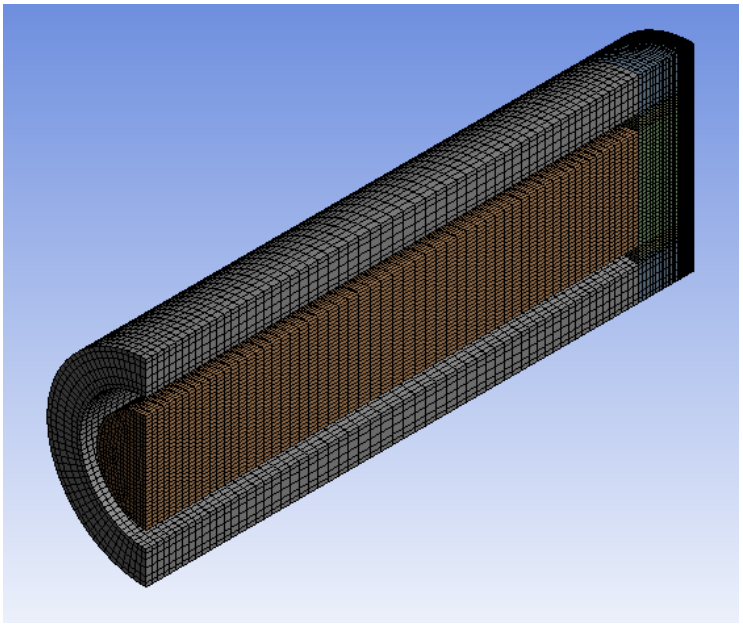

(a) Overview of the final mesh.

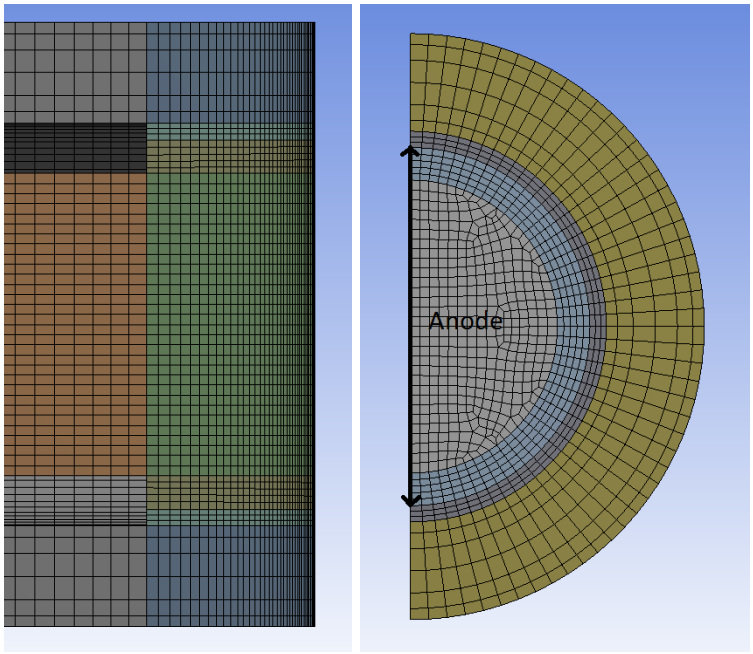

(b) Side view of the mesh. (c) Front view of the mesh.

Figure 4.13: Pictures of the fuel side of the final mesh. The mesh of each cross section is as shown in the bottom right, which is swept over the entire geometry. In axial direction, the mesh is refined towards the anode.

is also resulting in higher conversion. For the three cases, 7.5, 5 and 2.5 mm, the conversions found in the simulation are 18.1, 19.1 and 20.6% respectively.

In Figure 4.15 the line plots that were used to optimise the mesh are plotted for the three inlet distances. Indeed, the reaction rate is highest in the case with the inlet closest to the anode (2.5 mm). Surprisingly, the temperature is also higher in this case. The plot reveals that the additional heat comes from the fuel feed and shows once more that diffusion and conduction are the dominant transport mechanisms for these operating conditions, and not convection. A part of the additional heat can be a result of the prescribed temperature boundary condition. It would then be necessary to include thermal conduction in the ceramic inlet tube.

It is because of the diffusion limitations that the inlet distance has such a large influence on the solution. This is highlighted by the profile of the hydrogen concentration. The higher flow velocity that results from closer inlet distances is limiting back-diffusion toward the fuel inlet tube. The effect is a lower hydrogen concentration inside the anode, while it causes higher concentrations of methane and steam in the anode. Away from the anode, this effect reverses due to the higher methane conversion, which becomes clear from the plots in radial direction.

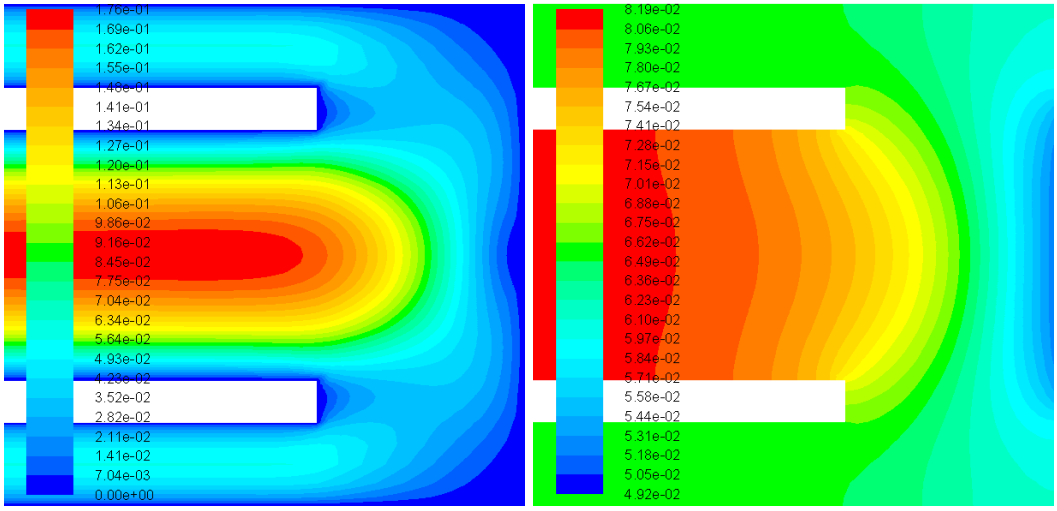

(a) Velocity magnitude, 7.5 mm (b) Methane concentration, 7.5 mm

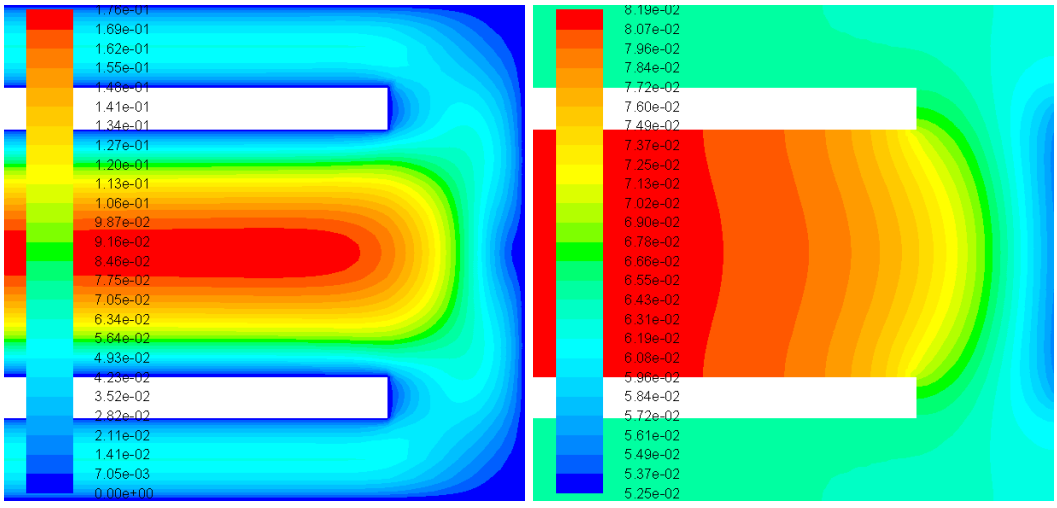

(c) Velocity magnitude, 5 mm (d) Methane concentration, 5 mm

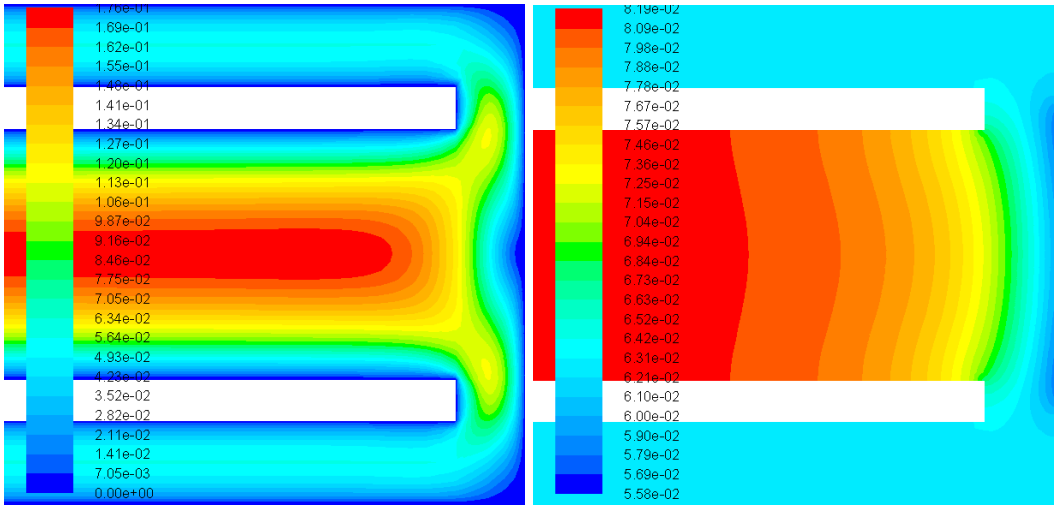

(e) Velocity magnitude, 2.5 mm (f) Methane concentration, 2.5 mm

Figure 4.14: Influence of the inlet distance on the velocity magnitude [m/s] and methane concentration [mol/mol].

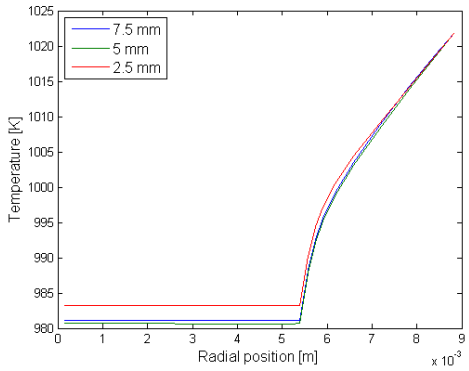

(a) Temperature, radial direction

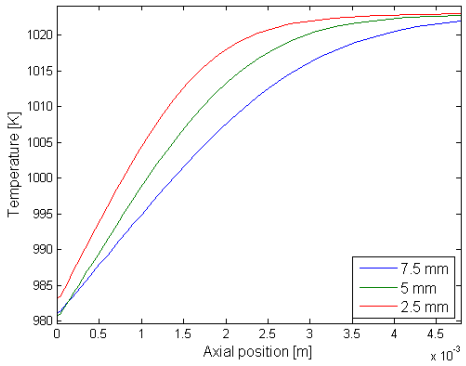

(b) Temperature, axial direction

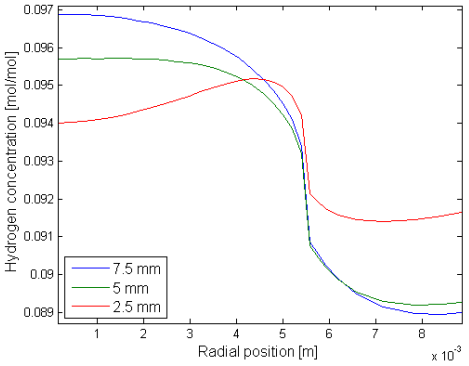

(c) Hydrogen, radial direction

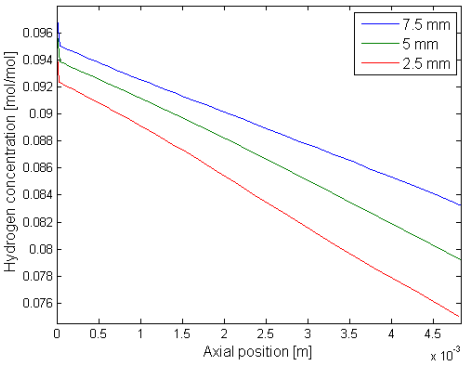

(d) Hydrogen, axial direction

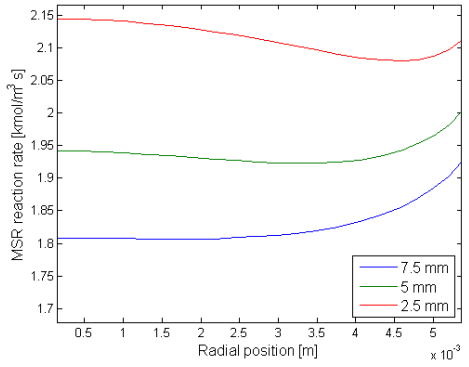

(e) MSR rate, radial direction

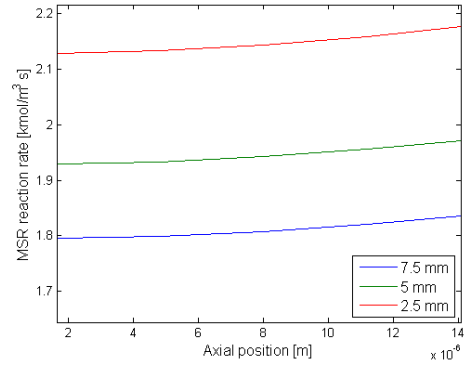

(f) MSR rate, axial direction

Figure 4.15: Spatial distribution of temperature, hydrogen concentration and MSR reaction rate in radial and axial direction for three simulated inlet distances.

Chapter 5

Modelling results and Discussion

With the final mesh obtained and model implementation checked the model can now be used to study cell performance under different operation conditions. The spatial variation of species concentration, temperature and current density obtained with the model can be used to verify assumptions and gain insight in the operation of fuel cells fuelled with methane. Ultimately it can be used to validate kinetic models and check whether the present model is capable of predicting fuel cell performance in an accurate way and can thus be used in future modelling studies.

5.1 Square Cell results

The model of the square cell is used to evaluate the rate equation proposed in Chapter 2. The results are compared with those obtained in the experimental work of Fan [52] and the power law model fitting to the same data. It is checked whether the model is able to predict the results and trends found in the experimental investigation.

5.1.1 Final model parameters

The physical properties of the anode and the electrolyte used in the final model are based on earlier modelling work in this group [34]. The electrochemical parameters are those reported in the modelling work of Costamagna [7]. After carefully studying the code of the ANSYS FLUENT SOFC module it is found that only a temperature depended cathode reference current is implemented.

For the anode, this reference current is assumed to be constant and is calculated for every modelled temperature. The default electrolyte conductivity sub model in the module is only valid from 1073 K and is thus not applicable to this study. Therefore and because the temperature is expected to be constant, the electrolyte conductivity is assumed to be constant as well.

Using a UDF, see Appendix F, the MSR rate equation and fitted parameters proposed in Chapter 2 is hooked to the final model. The power law comparison is also based on the parameters derived in Chapter 2. In both cases, the rate constant k_0 is fitted to meet a particular conversion in one case of the experimental data: gas

Table 5.1: Table of the final model input parameters for the model rate equation proposed in Chapter 2.

Anode		
Porosity ε	m^3/m^3	0.35
Tortuosity ι^2	m^2/m^2	5
Viscous drag K	$1/m^2$	1e8
Solid density ρ	kg/m^3	7760
Heat capacity c_p	J/kg K	600
Thermal cond. λ	W/m K	6
Electrical cond. δ	1/Ohm m	3.03e4

Electrolyte		
Density ρ	kg/m^3	6000
Heat capacity c_p	J/kg K	400
Thermal cond. λ	W/m K	2.7

Electrochemistry		
Anode i_0	A/m^2	5.5e8
$R/E_{A,anode}$	K^{-1}	8.314e-5
Cathode i_0	A/m^2	7e8
$R/E_{A,cathode}$	K^{-1}	6.928e-5
$[H2]_{ref}$	mol/mol	1
$[H2O]_{ref}$	mol/mol	1
$[O2]_{ref}$	mol/mol	1
γ_{H_2}	-	1
γ_{H_2O}	-	1
γ_{O_2}	-	0.25

MSR		
k_0	$(kmol/m^3)^{1.5}$ s	2.525e6
E_a	kJ/mol	164.7
A_O	-	173.8
ΔE_O	kJ/mol	35.05

WGS		
k_0	$(kmol/m^3)^{-1}$ s	1.626e7
E_a	kJ/mol	67.13
α_{CO}	-	1
β_{H_2O}	-	1

composition one at 998 K under open circuit conditions (see Appendix B). For the WGS, parameters based on Fan [52] are used in the model. The parameter values are summarised in Table 5.1.

5.1.2 Methane Steam Reforming kinetics

To compare the kinetic model derived in Chapter 2 to the experimental data gas composition, temperature and current density are varied in the model. The applied boundary conditions are selected to represent those in the experiment and the influence on the methane reforming rate is compared to experimental rate. The trends are checked qualitatively and quantitatively. In addition, the distribution of species, temperatures, reaction rates and current density in the anode can give useful information to verify assumptions done in calculation of the kinetic parameters, examine local influences on the MSR reaction rate and improved SOFC design.

In Figure 5.1 the most important result is plotted. Five cases are modelled: The base case with gas composition one at 998 K, two changes in temperature (973 K and 1023 K), and two other gas compositions, case 4 with the highest methane partial pressure and case 7 with the highest steam partial pressure. To investigate the influence of the electrochemical reaction, the current density is also changed in all cases. An overview of the experimental conditions can be found in Appendix B.

The results reveal that the model proposed in Chapter 2 is indeed able to predict all trends observed in the experiment: The increase with methane partial pressure, the small decrease with increased steam partial pressure, the effect of temperature and the enhancing effect of the electrochemical reactions. It is thus likely that the

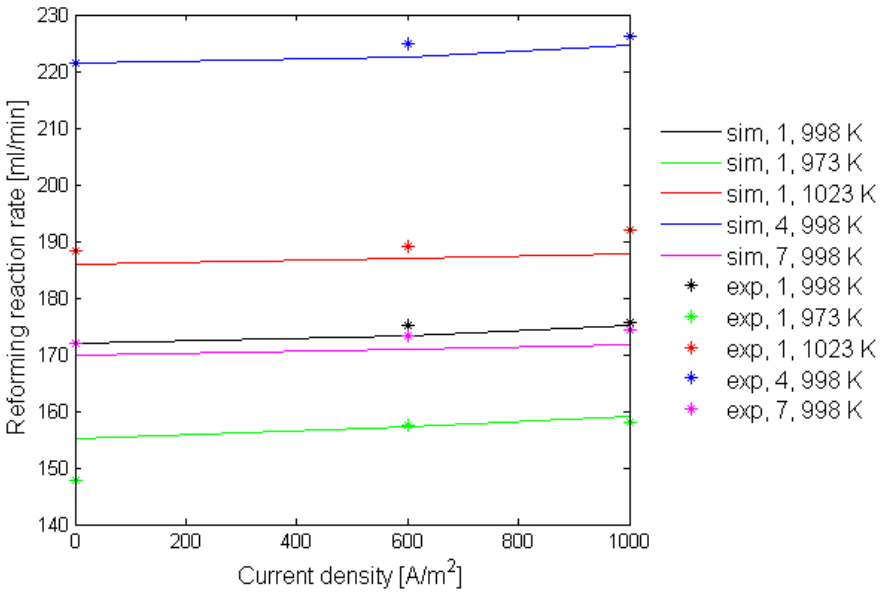

Figure 5.1: The overall reaction rate found with the proposed model (solid lines) compared to the data obtained in the experimental investigation (stars). The electrochemical reaction has an enhancing effect on the reforming rate in all cases, and the influences of gas composition and temperature is predicted correct in the model.

obtained model is able to predict both open and closed circuit MSR reactions on the fuel cell anode.

With a R^2 value of 0.987 the fit is quite good. The average error compared to the experimental data is only 1.17% and the worst case is with 4.91% still reasonable. Of course, since the model was fitted to the experimental data reasonable agreement might be expected. The agreement is however more than reasonable, especially if we consider that the model uses only two Arrhenius type constants based on two physical processes to correctly predict the influence of gas composition, temperature and electrochemistry. The numerical agreement is a strong indicator that the model captures the physics associated with rate limiting step of the MSR reforming.

The result shows that the mechanism of MSR on the fuel cell anode can be predicted by a model considering a rate limiting step on the catalyst surface between surface adsorbed radicals. The surface coverage of these surface adsorbed radicals is important and in equilibrium with the gas phase. This equilibrium follows from the energy associated with these processes and is of the Arrhenius type. For fuel cell operation conditions, it seems that the surface coverage of surface adsorbed oxygen can limit the number of reactions sites available for the MSR reaction.

In the following sections, the influences of gas composition, temperature and the electrochemical reactions are discussed in more detail. To do so, the spatial distribution of species, temperature and current density are plotted in the middle of the anode along the flow direction.

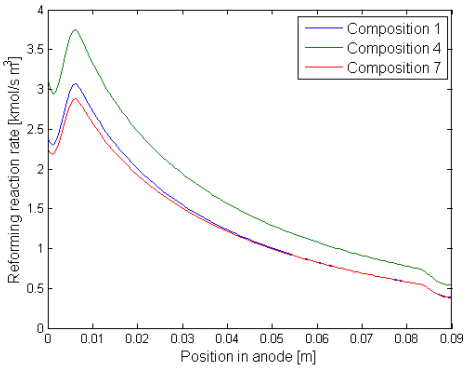

(a) MSR reaction rate

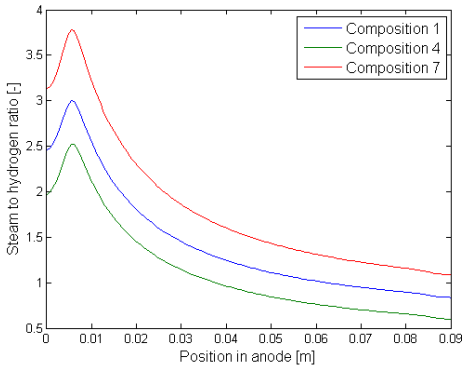

(b) Steam to hydrogen ratio

Figure 5.2: The effect of an increased methane partial pressure (composition 4) and steam partial pressure (composition 7) are plotted along the flow direction in the middle of the anode (5.2a). To highlight that the steam to hydrogen ratio is of particular importance at the inlet, the steam to hydrogen ratio is also plotted (5.2b).

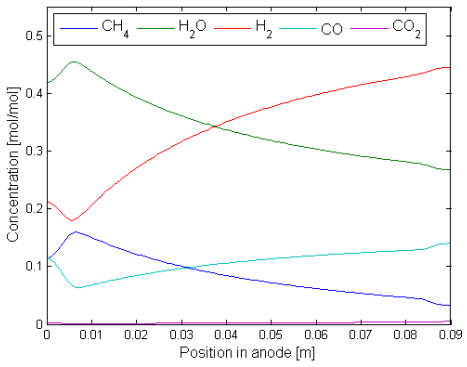

(a) Species distribution

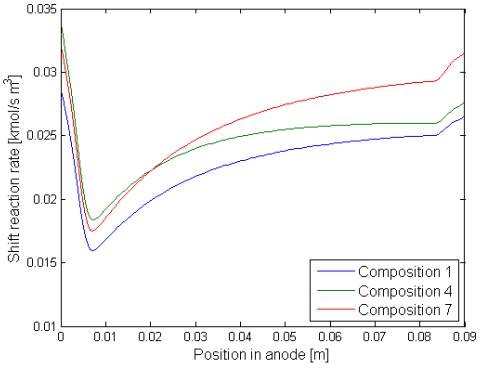

(b) WGS reaction rate

Figure 5.3: The gas composition distribution in the middle of the anode is plotted for the highest methane concentration at 998 K and open circuit conditions (5.3a). On the right, the influence of the gas composition on the WGS reaction rate is shown (5.3b).

The influence of the gas composition

In the experimental work a positive influence of methane and a small negative influence of steam was found. In Figure 5.2 spatial variation of the reaction rate for three gas composition is plotted. Methane has a general enhancing effect, as is expected. The influence of steam is slightly negative at the inlet. This negative effect disappears towards the outlet, where the steam to hydrogen ratio is lower as can be seen on the right. It shows that the influence of steam depends on the local conditions.

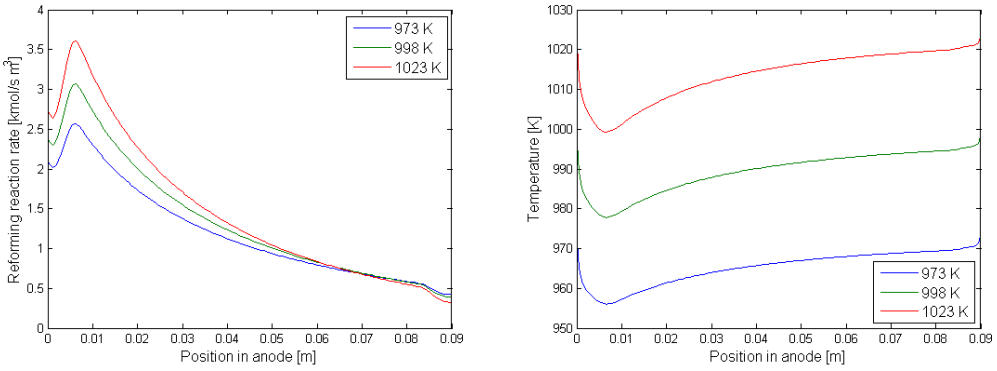

(a) MSR reaction rate

(b) Temperature distribution

Figure 5.4: The influence of the furnace temperature on the local MSR reaction rate is plotted (5.4a) as is the distribution of the temperature in the anode for these cases (5.4b).

In Figure 5.3a the variation of the gas composition is plotted for the gas composition with the highest methane partial pressure at 998 K and open circuit conditions. The first thing we noticed from the plot is the high steam to carbon ratio, higher than the 1.5 at the inlet. This is mostly because halfway into the anode a significant part of the methane is already reformed. The carbon dioxide concentration is very small, thus the water gas shift reaction is quite slow. Therefore, if the methane and carbon monoxide concentrations are compared in Figure 5.3a, they have an almost exact opposite correlation.

In Figure 5.3b the water gas shift reaction rate is plotted for the three gas compositions. As expected, the increase in either steam or methane partial pressure results in a higher reaction rate. The high hydrogen concentrations at the outlet limit the enhancing effect of the methane partial pressure. The low WGS reaction rate can be either a result of the specific operating conditions or because of inappropriate kinetic data. However, as the WGS reaction is found to be far from equilibrium in the modelling, the reason for the low rate is probably the latter.

The influence of temperature

To investigate the influence of the temperature we focus on the base gas composition again, at open circuit conditions. As can be seen in Figure 5.4a, the reaction rate is higher at higher temperatures. This is mainly at the inlet section, because the gas composition is similar in all cases. Towards the outlet section there is a crossover, as the high methane conversion has a severe limiting effect on the MSR rate.

In Figure 5.4b, the temperature distribution is plotted for the three furnace temperatures. Because a prescribed temperature boundary condition is used, there are quite sharp temperature gradients towards the wall. With more realistic boundary conditions, considering heat conduction in the ceramic parts, this is probably less severe. It is also worth mentioning that there is a deviation of the temperature in the anode from the wall that is proportional to the MSR reaction rate. Therefore

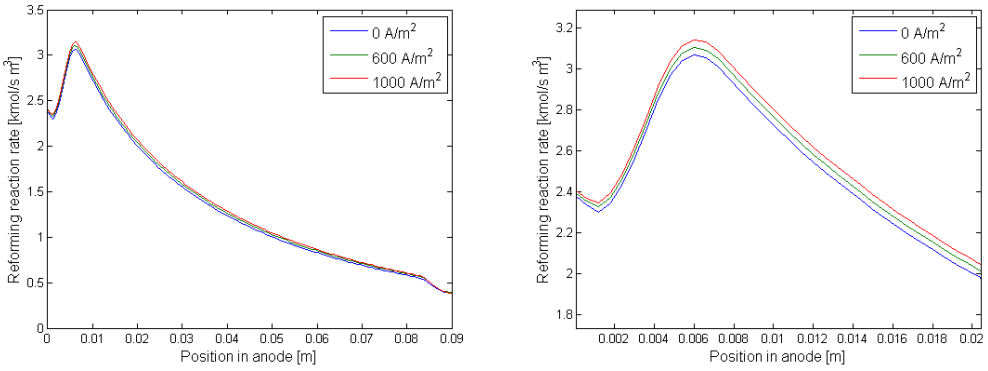

(a) MSR reaction rate

(b) Zoomed at the inlet

Figure 5.5: The effect of the current density in on the MSR reaction rate (5.5a), and zoomed in on the inlet section (5.5b).

the constant temperature assumption in the 1D Matlab model that was used to fit the data is not entirely correct. The highest deviation is about 25 K, which is considered to be still reasonable.

Electrochemical reactions

The main interest of this study is the investigation of the influence of the electrochemical reaction on the MSR reaction rate. In the model an improving effect was found, just like in the experimental investigation. This can be seen in Figure 5.5, for the base gas composition at 998 K. Zooming in at the inlet section reveals clearly that the electrochemical reactions have an enhancing effect on the reaction rate.

Although the improving effect of the electrochemical reactions on the MSR rate is very clear, it is interesting to see where it originates from. In Figure 5.6a the distribution of the current density along the flow direction is plotted. In Figure 5.6b the influence of the electrochemical reactions on the anode temperature is plotted. The current density is increasing in the flow direction because the fuel utilisation is relatively low at the tested current densities. The value along the middle of the channel is significantly higher than the average value in the whole anode, as the current density here is high compared to the current density on the sides of the channel. The endothermic electrochemistry results in an elevated temperature, which will enhance the MSR reaction rate.

Apart from changes in the temperature, the electrochemical reactions result in changes in the local gas composition. Others stated before that this would decrease the MSR reaction rate [46], as steam has a negative influence on the reaction. In Figure 5.7a the influence on the hydrogen partial pressure is plotted and in Figure 5.7b the change in steam to hydrogen ratio is shown.

As expected, the electrochemical reactions reduce the concentration of hydrogen in the anode. In the rate equation, hydrogen has a strong negative effect with an order of -2.5. Therefore, a beneficial effect of the lowered hydrogen concentration might be expected.

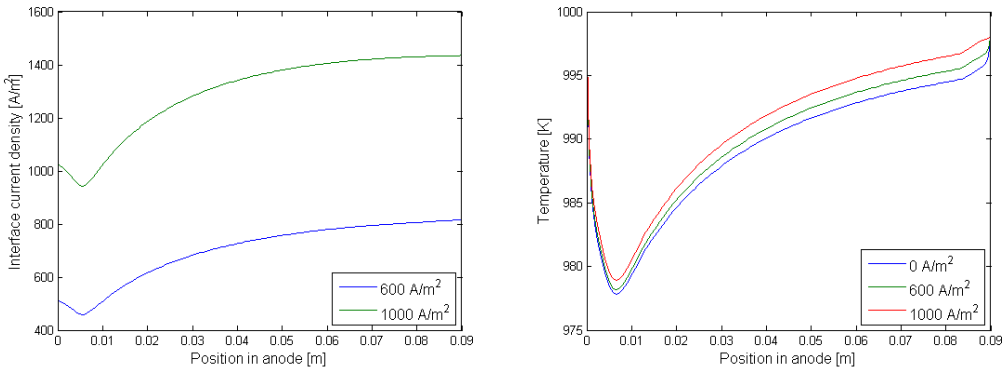

(a) Current density (b) Temperature distribution

Figure 5.6: Current density distribution along the middle of the channel (5.6a), and the effect on of the electrochemical reactions on the anode temperature (5.6b).

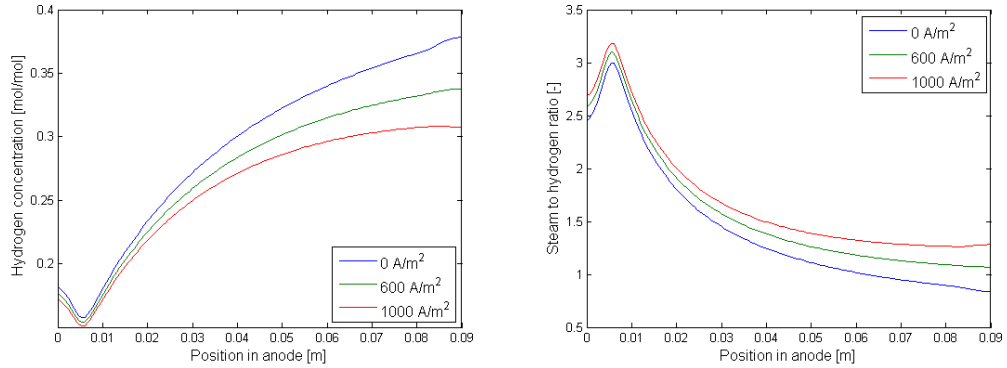

(a) Hydrogen concentration (b) Steam to hydrogen ratio

Figure 5.7: The effect of the current density on the spatial distribution of hydrogen (5.7a), and the steam to hydrogen ratio (5.7b).

From the same rate equation, it is also clear that high steam to hydrogen ratios have a negative effect on the MSR reaction rate. This ratio is increased by the electrochemical reactions, mostly in the outlet section. It is thus likely that an optimum current density exist, especially if high concentrations of steam are present in the inlet gas.

5.1.3 Square cell I-V characteristics

Of special interest in fuel cell operation is the Nernst voltage in the cell. This is influenced by the local temperature, gas composition and pressure and has an important influence on the fuel cell efficiency. The activation over potential at the anode is the main source of electrochemical losses. Both are displayed in Figure 5.8 for various gas compositions and temperatures at a current density of 1000 A/m^2.

It is clear that higher methane partial pressures are generally enhancing the

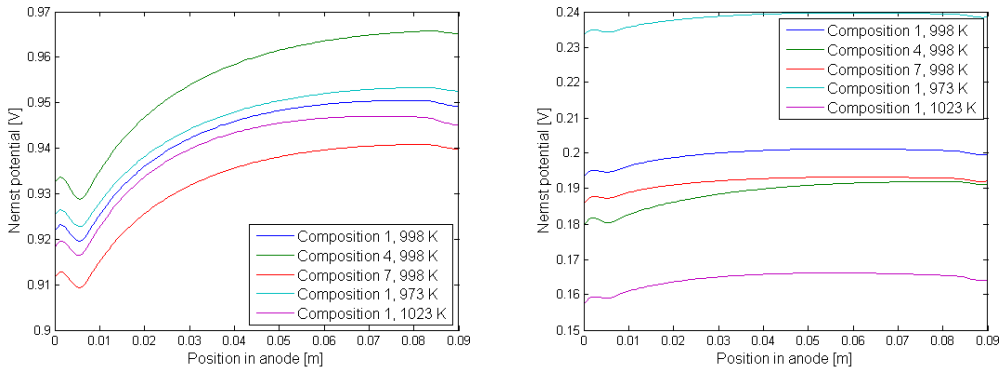

(a) Local Nernst potential

(b) Activation overpotential

Figure 5.8: The spatial variation of the Nernst potential (5.8a), and anode over potential (5.8b) in the fuel cell anode for various gas compositions and temperatures at a current density of 1000 A/m^2.

electrochemical efficiency. Higher steam concentrations lower the Nernst potential but also the activation over potential. The temperature has a small influence on the Nernst potential, but a dramatic effect on the activation losses. These distributions can be used to optimise fuel cell performance in fuel cell design and in the selection of operating conditions.

To investigate and validate the electrochemical performance of the square cell with the $Ni - GDC$ anode, the model is used to obtain current-voltage characteristics for the base gas composition (case 1), the composition with lowest methane and steam concentrations at 998 K. The current density is stepwise increased in the model and the result on the cell voltage is investigated. The resulting I-V characteristics and power density are plotted in Figure 5.9a.

In Figure 5.9b the effect of current density on the conversion of methane is shown. The conversion is increasing with current density, slowly in the first part and then apparently linear with the current density. The higher conversion will increase the Nernst potential thus enhancing the cell performance.

Compared to the experimental data it turns out that the model is generally underestimating the open circuit voltage and then shows similar behaviour with current density. The model is thus able to predict the fuel cell power with reasonable accuracy.

The deviation at open circuit conditions is probably because electrochemical conversion of species other than hydrogen and steam on the anode, like carbon monoxide, is neglected. Investigation in the model shows that including CO chemistry is elevating the open circuit voltage with 3.7e-2 Volt. Differences at higher current densities are most likely a result of the neglected ohmic losses.

5.1.4 Comparison to the Power Law expression

A common approach in the modelling of direct internal reforming in SOFCs is the use simplified power law expressions to calculate the methane steam reforming

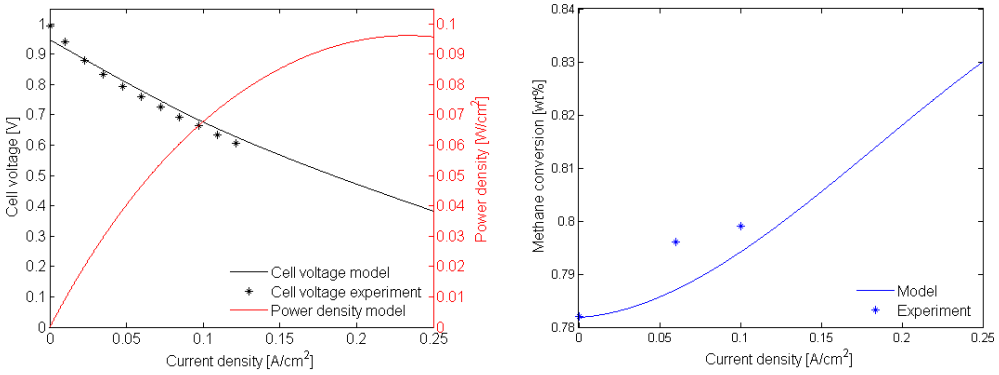

(a) I-V and I-W relation

(b) Methane conversion

Figure 5.9: I-V curve obtained with the model for the base case of the square cell (gas composition 1) at 998 K compared to the values obtained in the experiment (5.9a), and the respective methane conversion (5.9b).

Table 5.2: Constants in the power law (Equation (2.5)) fitted to the experimental data for the square cell at open circuit conditions. The value of k_0 is fitted to the same case in the CFD model.

Parameter	k_0 [mol Bar$^{0.5}$/s]	E_A [kJ/mol]	α_{CH_4} [-]	β_{H_2O} [-]
Value	4.60e6	88.0	0.64	-0.04

reaction rate. It is assumed this is a good strategy to get an idea of the species distribution in the anode without knowledge of the intrinsic reactions. Of course an error is made which is further evaluated in this section.

In Chapter 2 expressions for both a Power Law and a Langmuir-Hinshelwood rate equation are fitted to the experimental data. In Figure 5.10 the Langmuir-Hinshelwood expression that is evaluated in this chapter is compared to a power law expression fitted to the same experimental data. The parameters of the power law expression can be found in Table 5.2. For the Langmuir-Hinshelwood expression the parameters are those in Table 5.1.

To compare the two expressions, the base case, with gas composition one at 998 K and open circuit conditions is modelled in the CFD model. For both expressions the rate constant k_0 is fitted in FLUENT to match the conversion found in the experiment. The only difference is the type of expression with the respective parameters fitted to the experimental data.

In Figure 5.10a the resulting reaction rate is plotted along the flow direction in the middle of the anode. The reaction rate is much more sensitive to the species distribution for the LH expression, resulting in steeper gradients. This has a severe influence on the temperature distribution, as can be seen from Figure 5.10b.

Since the reaction rate is affected by the expression, the spatial distribution of the species concentrations are also different for the two rate equations as can be seen in Figure 5.10c. Although this effect seems to be less severe, it can be very important when electrochemical reactions are present or the test conditions are

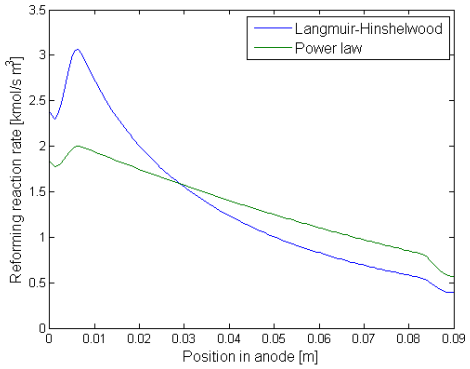

(a) MSR reaction rate

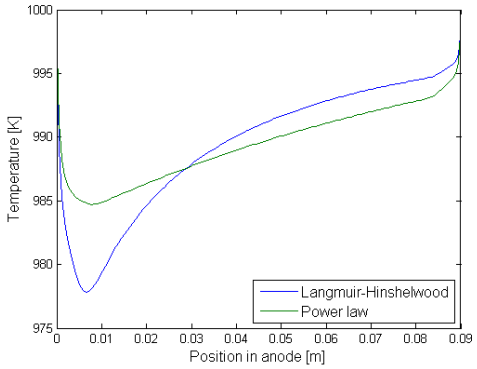

(b) Temperature

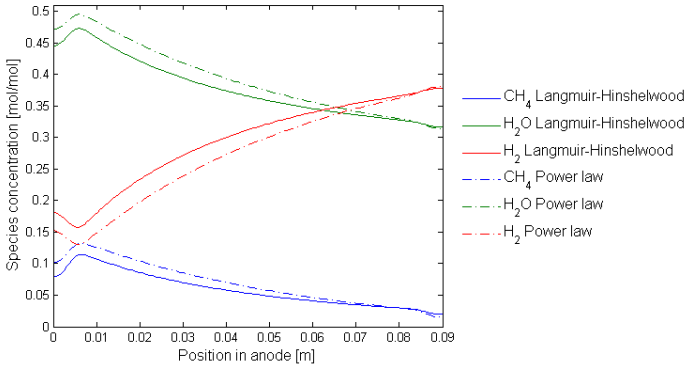

(c) Species concentrations

Figure 5.10: Simulated difference in the spatial distributions of the MSR reaction rate (5.10a), temperature (5.10b) and species distribution of methane, steam and hydrogen (5.10c) for the Langmuir-Hinshelwood and the Power Law rate equation. The lines are plotted along the flow direction in the middle of the anode.

optimised. Of course the difference in species concentration disappears towards the end of the channel as the conversion is the same in the two cases.

This result highlights that although a fit of reasonable quality can be obtained with the power law expression, neglecting of important physical processes in the MSR reaction makes the power law expression intrinsically invalid for most cases. The type of kinetic expression that is used in the modelling of chemical reactions in solid oxide fuel cells is therefore of crucial importance and should be able to correlate all relevant physical processes involved.

5.2 Button Cell results

The spatial distributions in the button cell setup differ from those in practical fuel cell operation. They are expected to be more homogeneous, which makes this setup useful for the study of specific reactions on the fuel cell anode. In addition, in-house fabricated cell can be used, allowing studies on specific anode materials and

Table 5.3: Constants in Equation 2.23 fitted to the experimental data for the button cell. The value of k_0 is fitted to one case in the CFD model.

Parameter	A_O [-]	ΔE_O [kJ/mol]	k_0 [mol Bar$^{0.5}$/s]	E_A [kJ/mol]
Value	2.448e6	116.5	1.500e7	135.3

morphologies. In the work of Fan [52] the influence of the anode thickness on the MSR rate was investigated.

5.2.1 Methane Steam Reforming kinetics

The model that is proposed in Chapter 2 is also implemented for the button cell setup. The material properties and electrochemical parameters are assumed to be the same as for the square cell. Since the model is steady state and we do not expect large temperature gradients in the anode the thermal properties will be of limited influence. These properties become more important in dynamic modelling and temperature gradients in actual fuel cell operation.

The parameters for the MSR reaction are those derived in Chapter 2. The activation energy is assumed to be constant and the value of k_0 is fitted to one specific case: gas composition 2 at 1023 K and open circuit conditions, see Appendix B. The MSR parameters are summarised in Table 5.3

Like with the square cell, the temperature, gas composition and current density are then changed and the effect on the conversion of methane is monitored. In addition, the thickness of the anode is changed. The results of the modelling compared to those obtained in the experiment can be seen in Table 5.4, based on the converted amount of methane.

It is clear that the deviations with the experimental results are significant. In contrast to the square cell, the model is incapable of predicting the conversions in the button cell. The R^2 value of the conversions is 0.364 for the open circuit conditions and becomes even negative if the closed circuit conditions are included.

To investigate why the results deviate that much from the experimental data, a closer study of the results is needed. The influences of gas composition, temperature, current density and anode thickness will be discussed individually in the following sections.

Gas composition

In the comparison the gas composition of the base case (composition 2) is changed. To test the influence of methane, the concentration is changed to composition 3, changing the methane concentration at the inlet from 8 to 12 ml/min. The influence of steam is investigated by changing to composition 5, reducing the steam concentration from 22 to 16 ml/min. An overview of the experimental inlet gas compositions can be found in Appendix B.

The effect of the changed gas composition on the reforming rate is evaluated by studying reforming rate, temperature and species distribution in the anode of the test cell. Since the anodes are very thin, these variables are virtually constant away from the electrolyte. The deviations are small but more significant in radial

Table 5.4: Results obained with the FLUENT model for the button cell setup.

Changed property	**Gas composition**		**Temperature**	
New value	Composition 3	Composition 5	1048 K	998 K
Conversion experiment (wt%)	0.125	0.273	0.158	0.186
Conversion mode (wt%)	0.152	0.180	0.160	0.173
Deviation (%)	21.6	24.1	1.27	6.99

Changed property	**Current density**		**Thickness**
New value	600 A/m^2	1000 A/m^2	27 μm
Conversion experiment (wt%)	0.352	0.352	0.240
Conversion model (wt%)	0.171	0.169	0.237
Deviation (%)	51.4	52.0	1.25

direction. Therefore the variables are plotted in radial direction in the middle of the anode. The results can be seen in Figure 5.11.

In agreement with the experimental data the increased methane concentration increases the MSR reaction rate. The reaction rate is also increased for lower steam concentrations, as was observed in the experiment. The temperature seems to be inversely correlated to the reforming reaction rate. There is a difference of approximately 17 K between the highest and the lowest reaction rate. More important, there is a large deviation up to 69 K with the temperature set in the furnace.

In the model, the concentration of methane and the steam to hydrogen ratio are of particular importance to the reaction rate. Consequently, a higher concentration of methane at the inlet results in an increased methane concentration in the anode while lower steam concentrations reduce the steam to hydrogen ratio. The higher reaction rates result in lower methane concentrations and a decrease in the steam to hydrogen ratios.

Temperature

The temperature of the inlet gas and boundaries is changed in the model to 1048 K and decreased to 998 K to study the effect of the temperature. The result on the distributions is plotted in Figure 5.12. The most important effect is the change in the reaction rate. As is observed in the experimental data, higher temperatures have a reducing effect on the MSR reaction rate. The change is however significantly smaller if the temperature is lowered, resulting in a smaller methane conversion compared to the conversion found in the experiment.

Due to the change in reaction rate the actual temperature deviations are a bit larger. For the experimental conversions these deviations will be even larger, as reaction rate changes more in the experiment. The absolute temperature is again significantly lower than the temperature set in the furnace. The methane concentration and steam to hydrogen ratio are inversely coupled to the MSR reaction rate, as is expected.

The decrease of the reaction rate with temperature is a strong non-Arrhenius

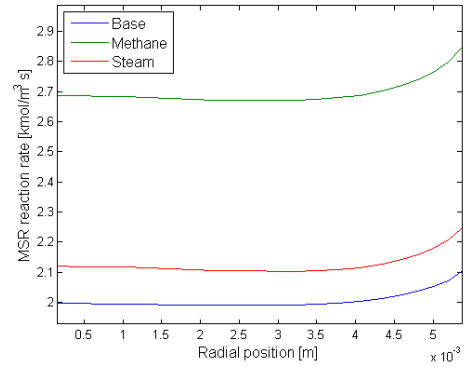

(a) MSR rate, radial direction

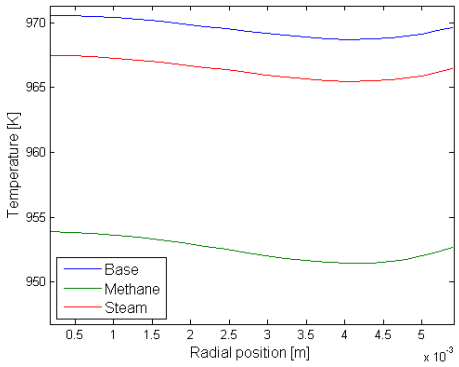

(b) Temperature, radial direction

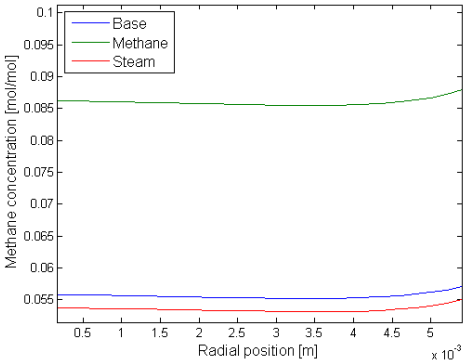

(c) Methane, radial direction

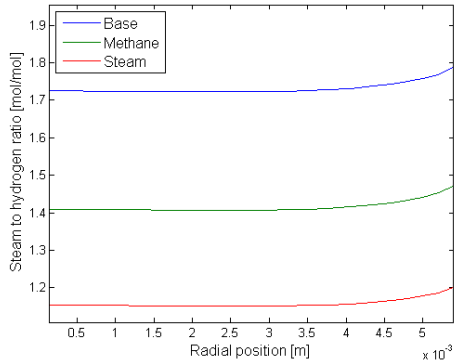

(d) Steam to hydrogen, radial direction

Figure 5.11: Results of an increased methane concentration and a decreased steam concentration compared to the base case. Radial distribution of MSR rate, temperature, methane concentration and steam to hydrogen ratio in the middle of the anode.

type correlation that is rarely observed. The model shows the capability to predict the negative temperature trend, which is attributed to the increased surface coverage of surface adsorbed oxygen, limiting the number of reaction sites. This works best for the higher temperatures, which are already significantly lower compared to the temperature assumed in the fitting. In addition, the steam to hydrogen ratio in the anode is probably lower due to diffusive effects. For these reasons, the effect is probably underestimated in the fitting.

Electrochemical reactions

In the experiment the electrochemical reactions have a large influence on the reforming rate of methane. There is little difference between the two current densities, but there is a large improvement from open circuit to closed circuit conditions. The model completely fails to predict this behaviour: a small improvement is observed for a current density of 600 A/m^2, but increasing the current density to 1000 A/m^2 is decreasing the reaction rate as can be seen in Figure 5.13.

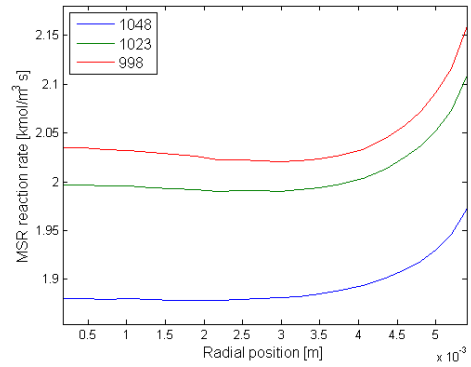

(a) MSR rate, radial direction

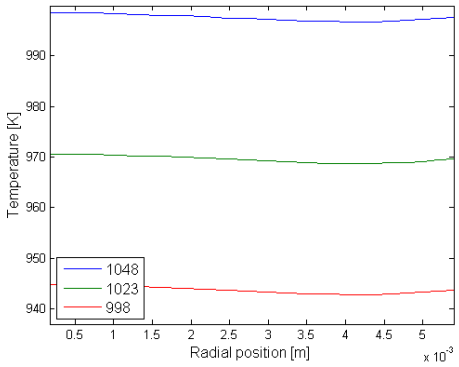

(b) Temperature, radial direction

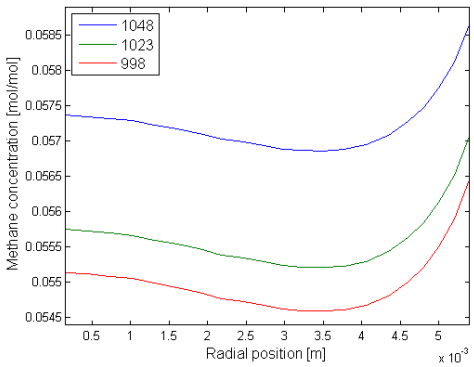

(c) Methane, radial direction

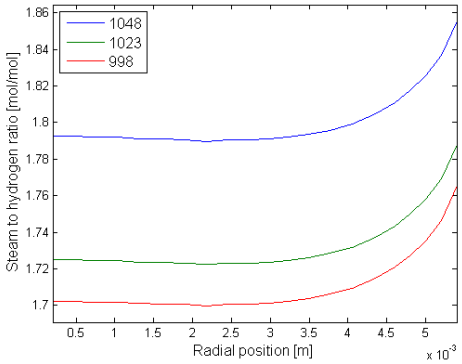

(d) Steam to hydrogen, radial direction

Figure 5.12: Distributions in the middle of the anode for various furnace temperatures: the *base case* at 1023 K, and the effects of an elevated and lowered furnace temperature.

The temperature is affected significantly by the electrochemical reactions. The temperature is increased about 19 K for the 1000 A/m^2 case. With the negative influence of temperature, this is probably decreasing the reforming rate. Another reason for the decrease is found in the increased steam to hydrogen ratio, changing from 1.73 at open circuit conditions to 2.05 at 1000 A/m^2.

Anode thickness

To study the influence of the anode thickness plots in axial direction can be seen in Figure 5.14. It is clear that the general trends are the same in the anode. The higher conversion has an influence on the absolute values. Again, the distribution of species in the anode is very homogeneous. The temperature drops to 951 K, a 72 K drop from the 1023 K set in the furnace.

From Table 5.4 it can be observed that the influence of the anode thickness on the reaction rate is predicted correct by the model. This suggests that the thickness of the anode increases the number of reaction sites, but does not change the reaction mechanism on the anode.

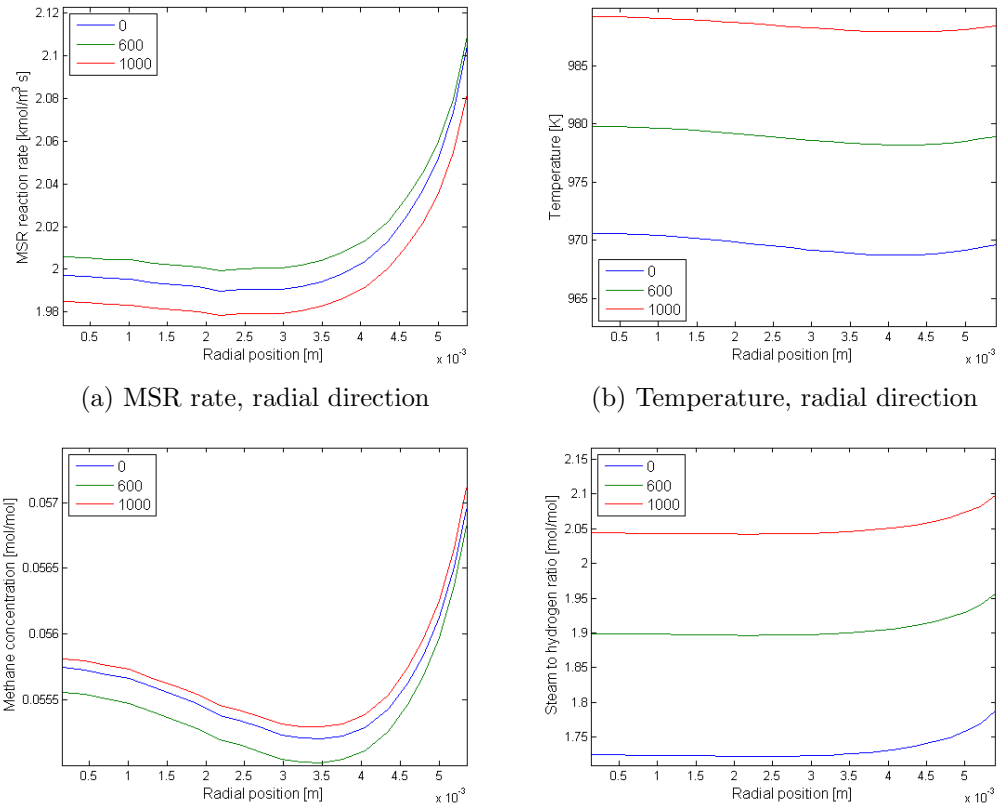

(a) MSR rate, radial direction

(b) Temperature, radial direction

(c) Methane, radial direction

(d) Steam to hydrogen, radial direction

Figure 5.13: Influence of the electrochemical reactions on the spatial distributions in the anode. The reaction rate increases first but then decreases rapidly. The electrochemical reactions increase the anode temperature and the steam to hydrogen ratio.

5.2.2 Important observations

The button cell model is able to predict the correlations with temperature and gas composition qualitatively, but fails to predict it numerically correct. Only the effect of an increased anode thickness and temperature seems to be predicted with reasonable accuracy.

Further investigation of the deviations was done in the previous sections. Clear deviations from the assumptions in the fitting procedure are the differences between the anode gas composition and outlet gas composition, assumed to be similar in the fitting, and the constant temperature assumption. The largest deviation, found for the varied anode thickness, resulted in a temperature drop of 72 K. For higher methane reaction rates, the temperature drop will be even more severe and probably very unrealistic.

To investigate the effect of this temperature drop and different gas composition, a worst case is modelled in which the highest methane conversion is forced with a first order in methane model. This was experimentally observed for gas composition

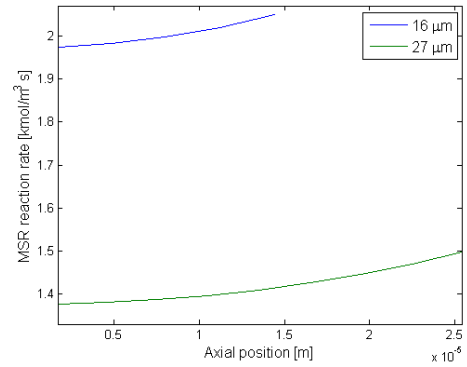

(a) MSR rate, axial direction

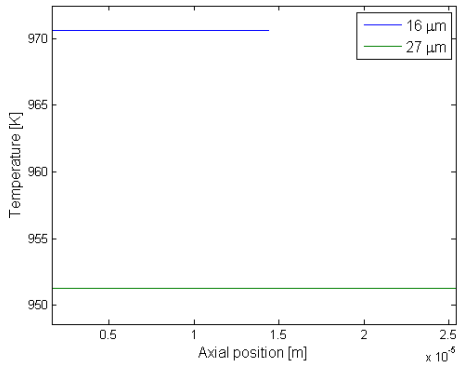

(b) Temperature, axial direction

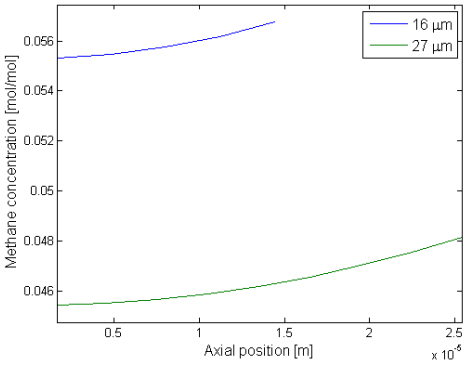

(c) Methane, axial direction

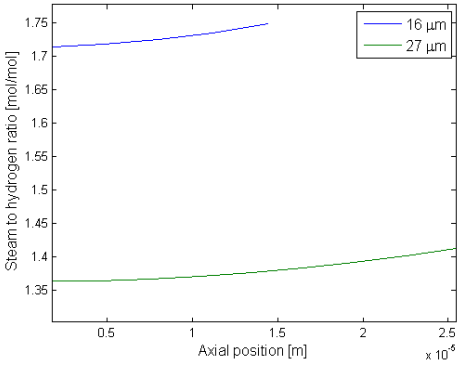

(d) Steam to hydrogen, axial direction

Figure 5.14: Radial distribution of MSR rate, temperature, methane concentration and steam to hydrogen ratio in the middle of the anode for an increased methane concentration and a decreased steam concentration compared to the base case.

three at 973 K, with a conversion over 50%. The influence of this conversion on the anode temperature and gas compositions is investigated in the model.

In Table 5.5 the results of this worst case analysis is shown. A remarkable difference between the furnace and anode temperature is predicted by the model, 763.1 K, as well as a large difference between the gas composition in the anode and the outlet gas, mainly because a large bypass of fuel gas.

The predicted temperature drop is very unrealistic and there is a good chance that it would result in a broken cell. Another quite alarming result is that the ratio between product gasses and reactants is much larger than the equilibrium constant for the anode temperature. In other words, the measured conversion at the predicted temperature is thermodynamically impossible.

There are several explanations possible for this contradiction, such as problems with the experimental setup or measurements and modelling assumptions. The experimental mass flow might be overestimated due to bad calibration or gas leakage or the mass spectroscopy inaccurate.

Apart from that, methane might be converted by other reactions than methane steam reforming on the anode. For the high temperature drops predicted by the

Table 5.5: The difference between the temperature and the mole fractions at the outlet and in the anode in the model for a case with 50% methane conversion. The ratio between product and reactants is given for the gas composition, as well as the thermodynamic equilibrium at the local temperature.

	T [K]	X_{CH_4}	X_{H_2O}	X_{H_2}	X_{CO}	$K(X)$	$K_{eq}(T)$
Outlet	973	0.0539	0.1272	0.2080	0.0553	0.07208	9.132
Anode	763.1	0.0108	0.0922	0.2315	0.1083	1.3449	4.652e-3

model, neglecting radiative heat transfer will most certainly result in an underestimated anode temperature.

Chapter 6

Conclusions and Recommendations

In Chapter 5 the kinetic model that is proposed in Chapter 2 is evaluated in a full 3D finite volume model developed in FLUENT with the SOFC add-on module to solve the electrochemistry. This has been done for both the $Ni - GDC$ square anode and the $Ni - YSZ$ button cell anode. Conclusions regarding the results and recommendations for future work are discussed in this chapter.

6.1 Conclusions

The objectives of this study were to:

- Study the influence of the test setup geometry on the spatial distributions in the fuel cell anode;
- Evaluate the use of ideal reactor models for the fitting of experimental data obtained in operational SOFCs;
- Investigate possible Methane Steam Reforming mechanisms on SOFC anodes;
- Study the influence of electrochemical reactions on the MSR reaction rate in SOFC anodes.

The conclusions are discussed separately in the following sections.

6.1.1 Test setup geometry

An important objective of the work was to investigate the influence of the specific design of the test setup geometry on the distribution of species, temperature and finally the MSR rate in the fuel cell anode for two test setups. The full 3D finite volume FLUENT model confirms very different distributions in the two setups.

In the square cell, fuel flows along the anode. The flow field has a significant influence on the distributions and species are diffusing into and out of the anode along the flow reactions. The distributions are therefore far from homogeneous. Since the anode is very thin (35 μm) diffusion towards the electrolyte is quite fast. Diffusion in sideways direction in the anode is slow.

For the button cell test rig, the distribution is completely different. The distance between the fuel inlet and the anode has an important influence on the flow field, and thus on the distributions in the anode. If the inlet is close to the anode, the distribution of species becomes more flow controlled. If the inlet section is far from the anode, diffusion is the main mass transport mechanism. This is assumed to be the case during the experiments, and results in well mixed conditions in the anode. Again, due to the limited thickness of the anodes (16 and 27 μm), the effect of diffusion in the anode itself is of limited importance.

6.1.2 Ideal reactor models

Considering the iterative (non-linear) nature of fitting the kinetics parameters it is numerically attractive to use ideal reactor models using some basic assumptions for fitting purposes. If the assumptions are reasonable, the influence on the quality of the fit is limited. Further evaluation of the obtained reaction model and the assumptions is however very important.

In the work of Fan [52] the MSR kinetics were experimentally investigated and fitted to a power law reaction model with a 1D ideal plug flow reactor model. The original fitting procedure was improved in Chapter 2. Based on the results obtained with the CFD model, it is decided that the ideal plug flow reactor model is indeed the best choice for the square cell. For the well-mixed composition in the anode of the button cell a 0D continuously ideally stirred tank reactor model is best to fit the experimental data.

For the square cell the data fitted to the ideal plug flow reactor model performs very well in the FLUENT model. The R^2 value of the results obtained with this model is with 0.987 quite close to a perfect fit. This shows that if the assumptions in the ideal model are reasonable it can be used to fit experimental data. For the button cell, the fit is worse. It is however shown that this is mainly because the kinetic model is unable to predict the observed conversions and because the assumptions (constant temperature, ideally mixed) are unreasonable.

6.1.3 Methane Steam Reforming reaction mechanism

In Chapter 2 the methane steam reforming reaction is evaluated based on the numerous rate equations reported in literature and the experimental work in the desertion of Fan [52]. It was found that:

- The surface coverage of oxygen is likely to play a role in methane steam reforming reaction. Reaction site blocking of oxygen would explain the negative influence of steam that is often reported;
- The negative influence of steam increases with temperature and could be responsible for the negative influence of higher temperatures observed in the button cell experiment;
- The adsorption of methane on the catalyst is probably much slower and does not seem to result in significant reaction site blocking;
- The adsorption of the other species does not seem to influence the reaction kinetics for these experimental conditions.

Based on these conclusions various models were tested, of which a fit to a simplified model proposed by Xu and Froment [14] gives good results:

$$-r = k\frac{p_{CH_4}p_{H_2O}}{p_{H_2}^{2.5}(1+K_O\frac{p_{H_2O}}{p_{H_2}})^2}$$

The model is of the Langmuir-Hinshelwood-Hougen-Watson type and is based on rate limiting kinetics between surface adsorbed radicals on the catalyst surface. The two parameters, k and K_O are of the Arrhenius type and increase with temperature.

This model predicts the methane conversion in the square $Ni-GDC$ anode with good accuracy. In addition it might explain why the reaction rate might decrease with temperature in the $Ni-YSZ$ button cell anode although its performance for this setup is poor. The modelling results for the button cell indicate more problems on this setup like unreasonable high temperature gradients and geometrical uncertainties.

The energy associated with the surface adsorption of oxygen is found to be different for the two cells, and deviates from the value obtained by Xu et al. [14]. This can be an indication that the support material is also involved in the surface adsorption of oxygen.

The strong surface coverage effect of atomic oxygen on the catalyst suggests that with high steam concentrations the electrochemical oxidation reaction might be governed by an oxygen spillover mechanism. This is in agreement with recently published work of Rossmeisl et al. [60], who concluded this from quantum mechanical calculations on the stability of surface-adsorbed molecules on several catalyst metals including Nickel.

6.1.4 Electrochemical reactions

The proposed model is based on rate equations developed for industrial reformers and showed good performance for the experiments done on the $Ni-GDC$ anode. This suggests that the methane steam reforming mechanism on this anode is similar to mechanisms proposed for industrial reforming.

In the experiments on the button cell, a huge improvement in methane conversion is observed at closed circuit conditions that seems to be unrelated to the value of the current. The general trends with temperature and species distribution are however not affected. This observation cannot be explained by the proposed kinetic model. As there are more uncertainties with respect to the results obtained in the button cell experiment further investigation is required to evaluate the enhancing effect of electrochemistry on this setup.

6.2 Recommendations

Although significant progress has been made in the modelling of direct internal reforming in solid oxide fuel cells, there are a number of issues that require further investigation. This includes experimental investigation, study of possible MSR reaction mechanisms, modelling work and the investigation of the influence of electrochemistry on the catalytic activity and reforming mechanism on the fuel cell anode.

6.2.1 Experimental investigation

In this work, a mechanism with a significant influence of hydrogen is proposed. Since the influence of hydrogen on the reaction rate is rarely reported this needs to be experimentally confirmed. This will be difficult since, according to the proposed mechanism, hydrogen can have both an enhancing and a limiting effect on the MSR reaction rate. The same holds for the partial pressure of steam. The influence of other species on the reaction rate, for example by adsorption effects, should also be investigated.

In the button cell experiments done by Fan [52] no direct information on the anode temperature was monitored. Since a large temperature drop is predicted in the model for the experimentally found conversions, it would be good to measure the temperature of the cell itself. This also gives direct information on the actual reaction temperature, which can be of significant influence in the fitting of temperature depended parameters. Large temperature drops can also be identified with electrochemical impedance spectroscopy.

6.2.2 Methane Steam Reforming mechanism and electrochemistry

In this work a rate equation is proposed that is able to predict the methane steam reforming on the $Ni - GDC$ anode. The enhancing effect of current is entirely explained by the influence on the gas composition and temperature in the anode. If this is the case, the study of the reaction mechanisms on substrates and crushed anode materials would be sufficient for modelling purposes.

On the $Ni - YSZ$ anode this was not achieved. The rapid increase of the reaction rate for closed circuit conditions cannot be explained by the proposed model. Whether this is the result of the problems with the test setup, modelling assumptions or selected reaction mechanism is not clear yet and should be investigated.

Further evaluation of the proposed model for various test conditions, current density and anode materials could give more insight in the reaction path of MSR in fuel cell anodes and reveal whether different mechanism exist on different anode materials and for different operation conditions.

6.2.3 Modelling of direct internal reforming

The modelling of direct internal reforming requires the solving of a lot of equations on a small interface. Preparing a good mesh, fine and structured near the anode, is of great importance to achieve accurate results. Solving a large number of equations is also computational demanding, on which the iterative nature of the solver is of significant influence.

The FLUENT SOFC add-on module is easy to work with but its applicability is limited. It is for example only possible to do full 3D simulations which is not very efficient for the often used axisymmetric geometries like the button cell setup. The default equations for the electrochemistry and correction for species diffusion are simple and effective but perhaps not applicable for more sophisticated problems. For example, the temperature dependence of the electrolyte resistance is only valid at temperatures from 1073 K to 1373 K and temperature dependent anode over potentials are not implemented yet.

To implement an intrinsic reaction mechanism, a volumetric rate equation was hooked to FLUENT in this study using UDFs. This is easy to do if the rate equation is programmed well and if it is stable, especially during initial solutions. The volumetric rate equation is perhaps problematic if the morphology of the anode is investigated, in which case wall-surface kinetics might be more convenient.

Bibliography

[1] L. Carrette, K. A. Friedrich, and U. Stimming, "Fuel cells: Principles, types, fuels, and applications," *ChemPhysChem*, vol. 1, no. 4, pp. 162–193, 2000.

[2] R. P. O'Hayre, S.-W. Cha, W. Colella, and F. B. Prinz, "Fuel cell fundamentals," 2006.

[3] R. M. Ormerod, "Solid oxide fuel cells," *Chem. Soc. Rev.*, vol. 32, pp. 17–28, 2003.

[4] V. Kharton, F. Marques, and A. Atkinson, "Transport properties of solid oxide electrolyte ceramics: a brief review," *Solid State Ionics*, vol. 174, no. 14, pp. 135 – 149, 2004. Solid State Ionics Dokiya Memorial Special Issue.

[5] J. T. Stock and M. V. Orna, *Electrochemistry, past and present*, vol. 390. ACS Publications, 1989.

[6] E. D. Wachsman and K. T. Lee, "Lowering the temperature of solid oxide fuel cells," *Science*, vol. 334, no. 6058, pp. 935–939, 2011.

[7] P. Costamagna, A. Selimovic, M. D. Borghi, and G. Agnew, "Electrochemical model of the integrated planar solid oxide fuel cell (IP-SOFC)," *Chemical Engineering Journal*, vol. 102, no. 1, pp. 61 – 69, 2004.

[8] Q. Li, R. He, J.-A. Gao, J. O. Jensen, and N. J. Bjerrum, "The CO poisoning effect in PEMFCs operational at temperatures up to 200°C," *Journal of the Electrochemical Society*, vol. 150, no. 12, pp. A1599–A1605, 2003.

[9] F. Calise, M. Dentice dAccadia, A. Palombo, and L. Vanoli, "Simulation and exergy analysis of a hybrid solid oxide fuel cell SOFC–gas turbine system," *Energy*, vol. 31, no. 15, pp. 3278–3299, 2006.

[10] J. Huijsmans, F. van Berkel, and G. Christie, "Intermediate temperature SOFC a promise for the 21st century," *Journal of Power Sources*, vol. 71, no. 12, pp. 107 – 110, 1998.

[11] K. I. of Technology, "Reaction kinetics of nanostuctured sofc cathodes," November 2014.

[12] P. Tsiakaras and A. Demin, "Thermodynamic analysis of a solid oxide fuel cell system fuelled by ethanol," *Journal of Power Sources*, vol. 102, no. 1, pp. 210–217, 2001.

[13] A. Atkinson, S. Barnett, R. J. Gorte, J. Irvine, A. J. McEvoy, M. Mogensen, S. C. Singhal, and J. Vohs, "Advanced anodes for high-temperature fuel cells," *Nature materials*, vol. 3, no. 1, pp. 17–27, 2004.

[14] J. Xu and G. F. Froment, "Methane steam reforming, methanation and water-gas shift: I. intrinsic kinetics," *AIChE Journal*, vol. 35, no. 1, pp. 88–96, 1989.

[15] T. Namioka, T. Naruse, and R. Yamane, "Behavior and mechanisms of ni/scsz cermet anode deterioration by trace tar in wood gas in a solid oxide fuel cell," *International Journal of Hydrogen Energy*, vol. 36, no. 9, pp. 5581–5588, 2011.

[16] J. R. Wilson, W. Kobsiriphat, R. Mendoza, H.-Y. Chen, J. M. Hiller, D. J. Miller, K. Thornton, P. W. Voorhees, S. B. Adler, and S. A. Barnett, "Three-dimensional reconstruction of a solid-oxide fuel-cell anode," *Nature materials*, vol. 5, no. 7, pp. 541–544, 2006.

[17] J. S. Newman, *Electrochemical Systems*. Prentice Hall, Englewood Cliffs, New Jersey, 1973.

[18] S. Chan, K. Khor, and Z. Xia, "A complete polarization model of a solid oxide fuel cell and its sensitivity to the change of cell component thickness," *Journal of Power Sources*, vol. 93, no. 12, pp. 130 – 140, 2001.

[19] V. Kharton, F. Marques, and A. Atkinson, "Transport properties of solid oxide electrolyte ceramics: a brief review," *Solid State Ionics*, vol. 174, no. 14, pp. 135 – 149, 2004. Solid State Ionics Dokiya Memorial Special Issue.

[20] J. W. Fergus, "Electrolytes for solid oxide fuel cells," *Journal of Power Sources*, vol. 162, no. 1, pp. 30 – 40, 2006.

[21] W. G. Bessler, "A new computational approach for SOFC impedance from detailed electrochemical reaction-diffusion models," *Solid State Ionics*, vol. 176, no. 1112, pp. 997 – 1011, 2005.

[22] R. B. E. III, G. M. Watson, and E. A. Mason, "Gaseous diffusion in porous media at uniform pressure," *The Journal of Chemical Physics*, vol. 35, no. 6, pp. 2076–2083, 1961.

[23] R. B. E. III, G. M. Watson, and E. A. Mason, "Gaseous diffusion in porous media. ii. effect of pressure gradients," *The Journal of Chemical Physics*, vol. 36, no. 7, pp. 1894–1902, 1962.

[24] H. Merk, "The macroscopic equations for simultaneous heat and mass transfer in isotropic, continuous and closed systems," *Applied Scientific Research, Section A*, vol. 8, no. 1, pp. 73–99, 1959.

[25] R. Suwanwarangkul, E. Croiset, M. Fowler, P. Douglas, E. Entchev, and M. Douglas, "Performance comparison of Ficks, dusty-gas and Stefan-Maxwell models to predict the concentration overpotential of a SOFC anode," *Journal of Power Sources*, vol. 122, no. 1, pp. 9 – 18, 2003.

[26] P. J. Kerkhof, "A modified maxwell-stefan model for transport through inert membranes: the binary friction model," *The Chemical Engineering Journal and the Biochemical Engineering Journal*, vol. 64, no. 3, pp. 319 – 343, 1996.

[27] D. Arnošt and P. Schneider, "Dynamic transport of multicomponent mixtures of gases in porous solids," *The Chemical Engineering Journal and the Biochemical Engineering Journal*, vol. 57, no. 2, pp. 91 – 99, 1995.

[28] J. Young and B. Todd, "Modelling of multi-component gas flows in capillaries and porous solids," *International Journal of Heat and Mass Transfer*, vol. 48, no. 2526, pp. 5338 – 5353, 2005.

[29] E. H. Kennard and E. H. Kennard, *Kinetic theory of gases: with an introduction to statistical mechanics*. McGraw-hill New York, 1938.

[30] N. Epstein, "On tortuosity and the tortuosity factor in flow and diffusion through porous media," *Chemical engineering science*, vol. 44, no. 3, pp. 777–779, 1989. eng.

[31] B. Haberman and J. Young, "Three-dimensional simulation of chemically reacting gas flows in the porous support structure of an integrated-planar solid oxide fuel cell," *International Journal of Heat and Mass Transfer*, vol. 47, no. 1718, pp. 3617 – 3629, 2004.

[32] B. Haberman and J. Young, "A detailed three-dimensional simulation of an IP-SOFC stack," *Journal of fuel cell science and technology*, vol. 5, no. 1, p. 011006, 2008.

[33] G. DiGiuseppe, N. K. Honnagondanahalli, O. Taylor, and J. Dederer, "Modeling studies of tubular sofcs for transportation markets," *Journal of Fuel Cell Science and Technology*, vol. 10, no. 2, p. 021009, 2013.

[34] Z. Qu, P. Aravind, S. Boksteen, N. Dekker, A. Janssen, N. Woudstra, and A. Verkooijen, "Three-dimensional computational fluid dynamics modeling of anode-supported planar SOFC," *International Journal of Hydrogen Energy*, vol. 36, no. 16, pp. 10209 – 10220, 2011. European Fuel Cell 2009.

[35] L. Fan, Z. Qu, M. J. B. M. Pourquie, A. H. M. Verkooijen, and P. V. Aravind, "Computational studies for the evaluation of fuel flexibility in solid oxide fuel cells: A case with biosyngas," *Fuel Cells*, vol. 13, no. 3, pp. 410–427, 2013.

[36] L. Fan, E. Dimitriou, M. Pourquie, M. Liu, A. Verkooijen, and P. Aravind, "Prediction of the performance of a solid oxide fuel cell fuelled with biosyngas: Influence of different steam-reforming reaction kinetic parameters," *International Journal of Hydrogen Energy*, vol. 38, no. 1, pp. 510 – 524, 2013. European Fuel Cell 2011.

[37] J. Yuan, G. Yang, and B. Sunden, "Simulation of surface reactions and multiscale transport processes in a composite anode domain relevant for solid oxide fuel cells," *Journal of Fuel Cell Science and Technology*, vol. 10, no. 2, p. 021001, 2013.

[38] E. S. Hecht, G. K. Gupta, H. Zhu, A. M. Dean, R. J. Kee, L. Maier, and O. Deutschmann, "Methane reforming kinetics within a Ni-YSZ SOFC anode support," *Applied Catalysis A: General*, vol. 295, no. 1, pp. 40 – 51, 2005.

[39] K. Hou and R. Hughes, "The kinetics of methane steam reforming over a Ni_{α}-Al_2O catalyst," *Chemical Engineering Journal*, vol. 82, no. 1, pp. 311–328, 2001.

[40] S. Elnashaie, A. Adris, A. Al-Ubaid, and M. Soliman, "On the non-monotonic behaviour of methane-steam reforming kinetics," *Chemical Engineering Science*, vol. 45, no. 2, pp. 491–501, 1990.

[41] D. Mogensen, J.-D. Grunwaldt, P. Hendriksen, K. Dam-Johansen, and J. Nielsen, "Internal steam reforming in solid oxide fuel cells: Status and opportunities of kinetic studies and their impact on modelling," *Journal of Power Sources*, vol. 196, no. 1, pp. 25 – 38, 2011.

[42] A. L. Lee, R. Zabransky, and W. Huber, "Internal reforming development for solid oxide fuel cells," *Industrial & engineering chemistry research*, vol. 29, no. 5, pp. 766–773, 1990.

[43] H. Yakabe, T. Ogiwara, M. Hishinuma, and I. Yasuda, "3-D model calculation for planar SOFC," *Journal of Power Sources*, vol. 102, no. 12, pp. 144 – 154, 2001.

[44] K. Ahmed and K. Foger, "Kinetics of internal steam reforming of methane on Ni/YSZ-based anodes for solid oxide fuel cells," *Catalysis Today*, vol. 63, no. 24, pp. 479 – 487, 2000.

[45] E. Achenbach and E. Riensche, "Methane/steam reforming kinetics for solid oxide fuel cells," *Journal of Power Sources*, vol. 52, no. 2, pp. 283 – 288, 1994.

[46] A. Dicks, K. Pointon, and A. Siddle, "Intrinsic reaction kinetics of methane steam reforming on a nickel/zirconia anode," *Journal of Power Sources*, vol. 86, no. 12, pp. 523 – 530, 2000.

[47] N. Nakagawa, H. Sagara, and K. Kato, "Catalytic activity of Ni-YSZ-CeO_2 anode for the steam reforming of methane in a direct internal-reforming solid oxide fuel cell," *Journal of Power Sources*, vol. 92, no. 12, pp. 88 – 94, 2001.

[48] V. M. Janardhanan and O. Deutschmann, "CFD analysis of a solid oxide fuel cell with internal reforming: Coupled interactions of transport, heterogeneous catalysis and electrochemical processes," *Journal of Power Sources*, vol. 162, no. 2, pp. 1192 – 1202, 2006. Special issue including selected papers from the International Power Sources Symposium 2005 together with regular papers.

[49] P. Aguiar, C. Adjiman, and N. Brandon, "Anode-supported intermediate temperature direct internal reforming solid oxide fuel cell. i: model-based steady-state performance," *Journal of Power Sources*, vol. 138, no. 12, pp. 120 – 136, 2004.

[50] V. Belyaev, T. Politova, O. Mar'ina, and V. Sobyanin, "Internal steam reforming of methane over Ni-based electrode in solid oxide fuel cells," *Applied Catalysis A: General*, vol. 133, no. 1, pp. 47 – 57, 1995.

[51] I. Yentekakis, Y. Jiang, S. Neophytides, S. Bebelis, and C. Vayenas, "Catalysis, electrocatalysis and electrochemical promotion of the steam reforming of methane over Ni film and Ni-YSZ cermet anodes," *Ionics*, vol. 1, no. 5-6, pp. 491–498, 1995.

[52] L. Fan, *Methane Steam Reforming Kinetics in Operating Solid Oxide Fuel Cells*. PhD thesis, 2014.

[53] "Ideal reactors," in *Systems Analysis for Water Technology*, pp. 101–127, Springer Berlin Heidelberg, 2008.

[54] A. Dicks, "Advances in catalysts for internal reforming in high temperature fuel cells," *Journal of power Sources*, vol. 71, no. 1-2, pp. 111–122, 1998.

[55] F. G. Helfferich, *Kinetics of multistep reactions*. Elsevier, 2004.

[56] L. Glasser, "Rates of bimolecular heterogeneous reactions following the Langmuir-Hinshelwood mechanism," *Journal of Chemical Education*, vol. 56, no. 1, p. 22, 1979.

[57] R. Peters, R. Dahl, U. Klttgen, C. Palm, and D. Stolten, "Internal reforming of methane in solid oxide fuel cell systems," *Journal of Power Sources*, vol. 106, no. 12, pp. 238 – 244, 2002. Proceedings of the Seventh Grove Fuel Cell Symposium.

[58] H. Freundlich, "Über die adsorption in lösungen," *Zeitschrift für Physikalische*, 1906.

[59] N. Bodrov, L. Apel'Baum, and M. Temkin, "Kinetics of the reaction of methane with steam on the surface of nickel," *Kinet. Katal*, vol. 5, p. 696, 1964.

[60] J. Rossmeisl and W. G. Bessler, "Trends in catalytic activity for SOFC anode materials," *Solid State Ionics*, vol. 178, no. 3132, pp. 1694 – 1700, 2008.

[61] S. Boksteen, "CFD modeling of transport phenomena in a complex geometry medium temperature solid oxide fuel cell," 2008.

[62] S. Hosseini, K. Ahmed, and M. O. Tad, "CFD model of a methane fuelled single cell SOFC stack for analysing the combined effects of macro/micro structural parameters," *Journal of Power Sources*, vol. 234, no. 0, pp. 180 – 196, 2013.

[63] J. O. Hirschfelder, C. F. Curtiss, R. B. Bird, *et al.*, *Molecular theory of gases and liquids*, vol. 26. Wiley New York, 1954.

[64] H. A. McGee, *Molecular engineering*. McGraw-Hill, 1991.

[65] B. Todd and J. Young, "Thermodynamic and transport properties of gases for use in solid oxide fuel cell modelling," *Journal of Power Sources*, vol. 110, no. 1, pp. 186 – 200, 2002.

[66] F. Fuller, "New method for prediction of binary gas-phase diffusion coefficients," *Ind. Eng. Chem.*, vol. 58, 1966.

[67] J. O. B.E. Poling, J.M. Prausnitz, *The Properties of Gases & Liquids, 5th Edition*. McGraw-Hilll, New York, 2000.

[68] H. Yakabe, M. Hishinuma, M. Uratani, Y. Matsuzaki, and I. Yasuda, "Evaluation and modeling of performance of anode-supported solid oxide fuel cell," *Journal of Power Sources*, vol. 86, no. 12, pp. 423 – 431, 2000.

Appendix A

Alternative modelling

Momentum losses in porous electrodes

Usually only viscous drag is used in the momentum source to model the momentum losses in the porous electrodes. Hosseini et al. [62] states a generalised for of Darcy's law to model the addition loss of momentum of a fluid in a porous medium:

$$S_M = -\frac{\mu}{\alpha_p}\vec{u} \tag{A.1}$$

$$\alpha_p = \frac{\varepsilon^3 d_p^2}{72\iota(1-\varepsilon)^2} \tag{A.2}$$

With α_p the permeability, d_p the mean particle diameter and ι the tortuosity of the porous medium. Note the similarity with the viscous drag in term in FLUENT.

Species transport in Solid Oxide Fuel Cells

The transport of species in SOFCs is essential to model their behaviour, and care should be taken to implement realistic transport equations. As diffusion is an important mechanism of transport in fuel cells, the specification of the diffusion constants is vital. In addition, the diffusion is limited in porous media for which the equations should be adjusted. There are several ways to do this. The complications of these methods vary, as do their accuracies.

Diffusivity coefficients

For multicomponent diffusion, binary diffusion coefficients have to be specified. By default, if ideal gas is assumed, fluent calculates these value from a modified Chapman-Enskog relation [64]. They can however also be specified by the user. Todd and Young [65] have shown that the Fuller's method [66] modified by Poling et al. [67] yields the best results:

$$D_{ij} = \frac{0.00143T^{1.75}(\frac{1}{M_{w,i}} + \frac{1}{M_{w,j}})^{0.5}}{p[(\sum v_i)^{1/3} + (\sum v_j)^{1/3}]^2} \tag{A.3}$$

With M_w being the molar weight of the species and v the species Fuller's parameter as indexed. The diffusivity of a single component in an ideal gas mixture follows from:

$$D_{i,GM} = \frac{1 - X_i}{\sum_{j \neq i}^{m} \frac{X_i}{D_{ij}}} \text{ [68]} \tag{A.4}$$

Porous media

To some authors believe, the Dusty-gas model [22, 23] would be most appropriate [25]. It does however require numerical solution, whereas Fick's and Stefan-Maxwell's do not, and according to Kerkhof the DGM does have its limitations as well [26]. Alternatively, MPTM [27] or CPIM [28] might therefore give better results.

DGM and MTPM

Both the Dusty Gas Model (DGM) and the Mean Transport Pore Model (MTPM) can model mass transport in the transient Knudsen region by adding an additional Knudsen diffusivity to a modified Stefan-Maxwell [27]:

$$\frac{J_{i,d}}{D_{i,k,p}} + \sum_{j=1, j \neq i}^{n} \frac{X_j J_{i,d} - X_i J_{j,d}}{D_{ij,p}} = -c_T \frac{dy_i}{dx} \tag{A.5}$$

Where J_d is the molar diffusive flux and $D_{i,k,p} = \psi D_{i,k}$ is the Knudson flow coefficient, given by [29]:

$$D_{i,k} = \langle r_p \rangle \frac{2}{3} \sqrt{\frac{8RT}{\pi M_{w,i}}} \tag{A.6}$$

and the binary diffusion coefficients $D_{ij,p}$ follows from $D_{ij,p} = \psi D_{ij}$. In the equation for the Knudson flow coefficient, $\langle r_p \rangle$ is the mean pore radius

About the value of ψ is some discussion. Epstein showed that the correct value however should be $\psi = \frac{\varepsilon}{\iota^2}$ [30], with ε being the porosity and ι the tortuosity of the porous medium. Some authors seem to forget the difference between the *tortuosity* and the *tortuosity factor*, which is the *tortuosity squared*.

The DGM and the MTPM do however have a different approach for the calculation of the permeation flux, additionally on the right hand side. Dusty Gas Model:

$$-X_i \frac{dc_T}{dx} (1 - \frac{B}{D_{i,k,p}}) \tag{A.7}$$

Mean Transport Pore Model:

$$-[\frac{B_i}{D_{i,k,p}} + \sum_{j=1, j \neq i}^{n} \frac{B_i}{P} D_{ij,p} X_j (1 - \frac{B_j}{B_i})] X_i \frac{dc_T}{dx} \tag{A.8}$$

Note that the permeability coefficient B in the DGM is just one additional parameter ($B = B_0 p/\mu$), whereas in the MTPM every mixture component has a different one:

$$B_i = D_{i,k} \frac{\omega \nu_i + K n_i}{1 + K n_i} + \frac{\langle r_p^2 \rangle \psi p}{8\mu} \tag{A.9}$$

In which equation ν_i is given by:

$$\nu_i = \sqrt{\frac{M_i}{\sum X_j M_j}} \tag{A.10}$$

While ω is a numerical coefficient depending on the wall-slip description, Kn_i the Knudsen number of component i and μ the dynamic viscosity.

Cylindrical pore interpolation model

The Cylindrical Pore Interpolation Model (CPIM) is proposed by Young and Todd [28] in order to create a more well-defined model with clear assumptions. It describes total species fluxes rather than diffusive mass fluxes alone [**?**]:

$$\vec{G}_i = Y_i \rho \vec{u} + \vec{G}_{i,d} \tag{A.11}$$

In the gas channels, the fluxes can be described with Stefan-Maxwell, like:

$$\nabla X_i = \frac{\tilde{M}}{\rho} \sum_{j=1}^{n} \left(\frac{\vec{G}_j X_i}{M_j D_{ji}} - \frac{\vec{G}_i X_j}{M_i D_{ij}} \right) \tag{A.12}$$

Where M_i and $\tilde{M}$ are the species and mean molar mass and $D_{ij} = D_{ji}$. In the porous electrodes the mass fluxes are calculated from n-1 independent modified Stefan-Maxwell relations:

$$\frac{\rho \varepsilon}{\iota^2} \nabla X_i = \frac{\tilde{M}}{\rho} \sum_{j=1}^{n} \left(\frac{\vec{G}_j X_i}{M_j D_{ji,e}} - \frac{\vec{G}_i X_j}{M_i D_{ij,e}} \right) \tag{A.13}$$

And one pressure gradient equation:

$$\frac{\varepsilon}{\iota^2} \nabla p = -A \sum_{i=1}^{n} \vec{G}_i M_i^{-1/2} \tag{A.14}$$

Note that $D_{ij,e} \neq D_{ji,e}$, as:

$$D_{ij,e} = (D_{ij}^{-1} + D_{i,k}^{-1})^{-1} \tag{A.15}$$

Finally, A is an interpolated pressure coefficient and is given by

$$A = (A_0^{-1} + A_\infty^{-1})^{-1} \tag{A.16}$$

With:

$$A_0 = \frac{8\tilde{\mu}}{\rho \langle r_p \rangle^2 \sum_{i=1}^{n} Y_i / \sqrt{M_i}} \tag{A.17}$$

$$A_\infty = \frac{3}{4\langle r_p \rangle} \left(\frac{\pi R T}{2} \right)^{1/2} \tag{A.18}$$

Appendix B

Experimental data

Table B.1: Gas compositions fed to the square cell $Ni - GDC$ anode. The total flow rate was kept constant at 1020 ml/min by adjusting the flow of nitrogen.

	Species flow rate [ml/min]				Ratios [ml/ml]		
Case	Methane	Steam	Hydrogen	Nitrogen	SC	HC	NC
1	220	450	80	270	2.05	0.36	1.23
2	240	450	80	250	1.88	0.33	1.04
3	260	450	80	230	1.73	0.31	0.88
4	300	450	80	190	1.50	0.27	0.63
5	220	480	80	240	2.18	0.36	1.09
6	220	510	80	210	2.32	0.36	0.95
7	220	540	80	180	2.45	0.36	0.82

Table B.2: Methane conversions found in the square cell setup for various temperatures, gas compositions and current densities.

Temp [K]	Current density [A/m^2]	Methane conversion [wt%] 1	2	3	4	5	6	7
1023	0	0.856	0.848	0.832	0.800	0.862	0.865	0.866
	600	0.860	0.852	0.837	0.818	0.860	0.860	0.860
	1000	0.873	0.865	0.846	0.829	0.873	0.870	0.874
998	0	0.782	0.776	0.762	0.738	0.780	0.784	0.782
	600	0.796	0.782	0.770	0.750	0.790	0.798	0.788
	1000	0.799	0.792	0.780	0.754	0.795	0.796	0.792
973	0	0.672	0.666	0.654	0.632	0.670	0.665	0.666
	600	0.716	0.706	0.690	0.656	0.710	0.717	0.713
	1000	0.718	0.709	0.693	0.658	0.715	0.717	0.712
923	0	0.435	0.409	0.392	0.370	0.430	0.426	0.426

Table B.3: Gas compositions fed to the button cell $Ni - YSZ$ anodes. The total flow rate was kept constant at 100 ml/min by adjusting the flow of nitrogen.

	Species flow rate [ml/min]				Ratios [ml/ml]		
Case	Methane	Steam	Hydrogen	Nitrogen	SC	HC	NC
1	4	22	5	69	5.50	1.25	17.25
2	8	22	5	65	2.75	0.63	8.13
3	12	22	5	61	1.83	0.42	5.08
4	8	19	5	68	2.38	0.63	8.50
5	8	16	5	71	2.00	0.63	8.88

Table B.4: Methane conversions found in the button cell setup for various temperatures, gas compositions, current densities and two anode thicknesses.

Anode thickness	Temp [K]	Current density [A/m^2]	Methane conversion [wt%] 1	2	3	4	5
16 μm	1048	0	0.238	0.158	0.100	0.250	0.274
		600	0.418	0.330	0.298	0.387	0.470
		1000	0.416	0.329	0.289	0.388	0.416
	1023	0	0.236	0.170	0.125	0.256	0.273
		600	0.474	0.352	0.317	0.421	0.457
		1000	0.473	0.352	0.319	0.408	0.423
	998	0	0.261	0.186	0.167	0.257	0.260
		600	0.507	0.370	0.334	0.425	0.430
		1000	0.509	0.374	0.333	0.429	0.434
	973	0	0.262	0.227	0.207	0.263	0.269
		600	0.511	0.376	0.340	0.430	0.420
		1000	0.508	0.377	0.379	0.436	0.443
27 μm	1048	0	0.218	0.210	0.190	0.241	0.243
		600	0.732	0.569	0.543	0.606	0.636
		1000	0.738	0.531	0.492	0.585	0.482
	1023	0	0.273	0.240	0.175	0.228	0.226
		600	0.735	0.549	0.503	0.575	0.604
		1000	0.736	0.546	0.460	0.575	0.573
	973	0	0.348	0.248	0.206	0.223	0.220
		600	0.781	0.589	0.519	0.566	0.610
		1000	0.777	0.587	0.517	0.571	0.568

Appendix C

Sensitivity analysis power law model

One of the most important parts of model evaluation, after the balances is to assess its sensitivity to its input parameters. This was originally done with a kinetic model derived in the work of Fan [52]. As outputs are selected: Cell voltage, Nernst voltage, methane conversion and the heat flux through the walls. The input parameters for the base case can be seen in Table 4.1. The respective change in parameters (absolute and in percentage) can be seen in Table C.1.

A sensitivity analyses reveals several things concerning the single channel model. It shows essentially which parameters have the largest effects on the solution and therefore on the cell or model performance. With respect to this it is concluded that:

- The model is stable and the change in solution is as expected for realistic changes in model parameters.
- Due to the relatively low current density compared to usual SOFC operation and neglected electric losses, electrochemical parameters have a limited influence on the solution. The current density itself however has a larger influence.
- The methane reforming kinetics, including pre-exponential factors and rate exponents have a huge influence on the conversion of methane and therefore on the realized cell voltage.
- Enabling CO chemistry has some influence on the Nernst voltage but has virtually no influence on the reforming chemistry. The water-gas shift reaction rate is however somewhat lower as carbon monoxide can be directly oxidised to carbon dioxide.
- The porosity has an important influence on the methane conversion, mostly because reactions are modelled on a volumetric basis: Increasing the porosity effectively increases the reaction volume.

From the analysis it is concluded that the correlations of the model seem to be correct. The parameters used predict realistic values and changing those shows expected behaviour. Parameters with a large influence on the solution should be fitted to experimental work in future study.

Table C.1: Result of the sensitivity analysis. The change in parameters and respective change of the model output, both absolute and in percentage, is displayed. A large relative change in the output data from a relatively small change in input parameters, like with the methane reforming rate exponent, highlights the models sensitivity to that specific parameter.

Property	Change (%)	Cell pot. (V)	%	Nernst (V)	%	Conv (%)	%	Q wall (W)	%
Reference		0.8434		0.9339		88.2		0.7937	
Current density	100	0.7154	-15.18	0.9017	-3.45	87.2	-1.13	0.5517	-30.49
Current density	-50	0.9061	7.43	0.9516	1.90	88.6	0.45	0.8818	11.10
Anode porosity	14.29	0.8520	1.02	0.9413	0.79	91.6	3.85	0.8279	4.31
Tortuosity factor	20	0.8396	-0.45	0.9307	-0.34	88.0	-0.23	0.7845	-1.16
Reforming k_0	-11.11	0.8405	-0.34	0.9317	-0.24	85.4	-3.17	0.7635	-3.80
CO chemistry	*enabled*	0.8645	2.50	0.9543	2.18	88.2	0	0.792	-0.21
Inlet temperature	-2.44	0.8434	0	0.9339	0	88.1	-0.11	0.8212	3.46
Wall temperature	-0.98	0.8454	0.24	0.9359	0.21	86.7	-1.70	0.7724	-2.68
Reforming α_{H_2O}	*to 0.1*	0.8239	-2.31	0.9193	-1.56	70.6	-19.95	0.5957	-24.95
And current density	-50	0.8918	5.74	0.9384	0.48	70.9	-19.61	0.6877	-13.36
Reforming α_{H_2O}	15.38	0.8179	-3.02	0.9153	-1.99	65.1	-26.19	0.5371	-32.33
R_{ele}	18.37	0.8345	-1.06	0.9332	-0.07	88.1	-0.11	0.7903	-0.43
R_{ele}	136.74	0.7786	-7.68	0.93	-0.42	88.2	0	0.7669	-3.38
$X_{H_2O,in}$	10	0.8417	-0.20	0.9295	-0.47	87.7	-0.57	0.788	-0.72
$X_{CH_4,in}$	-10	0.8371	-0.75	0.9285	-0.58	89.2	1.13	0.7077	-10.84
$\dot{m}_{fuel,in}$	10	0.8412	-0.26	0.9323	-0.17	85.2	-3.40	0.8538	7.57
Anode i_0	-10	0.8392	-0.50	0.9334	-0.05	88.1	-0.11	0.7912	-0.31
Temp dep $i_{0,c}$	-10	0.8431	-0.04	0.9336	-0.03	88.1	-0.11	0.7924	-0.16
Temp dep $E_{A,c}$	10	0.8431	-0.04	0.9336	-0.03	88.1	-0.11	0.7924	-0.16

Appendix D

Overview of proposed Methane Steam Reforming rate equations

An overview of kinetic expression that have been derived for methane steam reforming on Ni-catalysts.

Power law expressions

Achenbach and Riensche [45] developed a very simple first order in methane expression, that performed well for their test conditions:

$$-r = kp_{CH_4}(1 - \frac{p_{CO}p_{H_2}^3}{K_{eq}p_{CH_4}p_{H_2O}}) \tag{D.1}$$

Ahmed and Foger [44] were able to fit their data to a power law expression, but the coefficients are deviating in the experiments. The influence of steam is positive but the influence of steam is negative:

$$-r = kp_{CH_4}^{0.85<\alpha<1.4}p_{H_2O}^{-0.8<\beta<-0.35} \tag{D.2}$$

Lee et al. [42] found a strong negative dependency on the steam partial pressure:

$$-r = kp_{CH_4}p_{H_2O}^{-1.25} \tag{D.3}$$

Langmuir-Hinshelwood expressions

The most extensive study for industrial reforming was done by Xu and Froment [14]. They found two possible rate limiting steps, one dominant at low and one dominant at high temperatures. The overall methane reforming rate is given by:

$$-r = \frac{\frac{k_1}{p_{H_2}^{2.5}}(p_{CH_4}p_{H_2O} - \frac{p_{CO}p_{H_2}^3}{K_{eq1}}) + \frac{k_2}{p_{H_2}^{3.5}}(p_{CH_4}p_{H_2O}^2 - \frac{p_{CO_2}p_{H_2}^4}{K_{eq2}})}{(1 + K_{CO}p_{CO} + K_{H_2}p_{H_2} + K_{CH_4}p_{CH_4} + K_{H_2O}\frac{p_{H_2O}}{p_{H_2}})^2} \tag{D.4}$$

Similar kinetics were derived by Hou et al. [39]:

$$-r = \frac{\frac{k_1 p_{CH_4}p_{H_2O}^{0.5}}{p_{H_2}^{1.25}}(1 - \frac{p_{CO}p_{H_2}^3}{K_{eq1}(p_{CH_4}p_{H_2O})}) + \frac{k_2 p_{CH_4}p_{H_2O}}{p_{H_2}^{1.75}}(1 - \frac{p_{CO_2}p_{H_2}^4}{K_{eq1}(p_{CH_4}p_{H_2O}^2)})}{(1 + K_{CO}p_{CO} + K_{H_2}p_{H_2}^{0.5} + K_{H_2O}\frac{p_{H_2O}}{p_{H_2}})^2} \tag{D.5}$$

One of the first to find surface adsorption effects of oxygen was Bodrov et al. [59]:

$$-r = k\frac{p_{CH_4}}{1 + a\frac{p_{H_2O}}{p_{H_2}} + bp_{CO}} \tag{D.6}$$

A very classical rate equation was proposed by Nakagawa et al. [47] and Peters et al. [57]:

$$-r = k_1\frac{p_{CH_4}p_{H_2O}}{(1 + k_2p_{CH_4} + k_3p_{H_2O})^2} \tag{D.7}$$

Dicks et al. [54] initially proposed a classical expression involving four reactions sites:

$$-r = k_1\frac{p_{CH_4}p_{H_2O}}{(1 + k_2p_{CH_4} + k_3p_{H_2O})^4} \tag{D.8}$$

Later, Dicks et al. [46] used another mechanism that predicts negative influences of steam:

$$-r = k\frac{p_{CH_4}}{(1 + K_Hp_{H_2}^{0.5} + K_S\frac{p_{H_2O}}{p_{H_2}})^2} \tag{D.9}$$

Appendix E

Matlab scripts

Initialise FluidProp

```
%%%%%%%%%%%%%%%%%%%%%%%%%%
%     Init_FluidProp     %
%%%%%%%%%%%%%%%%%%%%%%%%%%

clc

global FP

%Create an instance of the FluidProp COM server
FP = actxserver ('FluidProp.FluidProp');
Msg='FluidProp: COM object created';
disp(Msg)
```

Calculate inlet mass flows

Square cell

```
%% Calculating inlet boundary conditions for the Square cell
% Calculation requires FluidProp

Init_FluidProp
T=[25];                                 % Reference temperature (...
   Ambient) [Celcius]
P=1.01;                                 % Reference pressure (...
   Atmospheric) [Bar]
V=1020;                                 % Total volume flow [ml/min]
Me=[220 240 260 300 220 220 220];       % Methane volume flow
St=[450 450 450 450 480 510 540];       % Steam volume flow
Hy=[80 80 80 80 80 80 80];              % Hydrogen volume flow
Ni=V-Me-St-Hy;                          % Nitrogen volume flow
St=[16 16 16 16 17 18 19];              % For steam, the exact mass ...
   flow is known

global FP

Model = 'GasMix';
```

```
nCmp  = 1;          % of no importance in case of pure fluid
Cnc   = [1,0];      % of no importance in case of pure fluid
Cmp   = 'CH4';

ErrorMsg = invoke(FP,'SetFluid_M',Model,nCmp,Cmp,Cnc);

[rho,ErrorMsg] = invoke(FP,'Density','TP',T,P);
m_Me=rho*Me/(60*1000*1000);


Cmp   = 'H20';
m_St=St/(1000*3600);
[rho,ErrorMsg] = invoke(FP,'Density','TP',T,P);
Stv=m_St*(60*1000*1000)/rho

Cmp   = 'H2';

ErrorMsg = invoke(FP,'SetFluid_M',Model,nCmp,Cmp,Cnc);

[rho,ErrorMsg] = invoke(FP,'Density','TP',T,P);
m_Hy=rho*Hy/(60*1000*1000);

Cmp   = 'N2';

ErrorMsg = invoke(FP,'SetFluid_M',Model,nCmp,Cmp,Cnc);

[rho,ErrorMsg] = invoke(FP,'Density','TP',T,P);
m_Ni=rho*Ni/(60*1000*1000);

% Total mass flow at reference conditions [kg/s]
M=m_Me+m_St+m_Hy+m_Ni

% Mass flows of individual compounds [kg/s]
mf_Me=m_Me./M
mf_St=m_St./M
mf_Hy=m_Hy./M
```

Button cell

```
%% Calculating inlet boundary conditions for the Button cell
% Calculation requires FluidProp

Init_FluidProp
T=[25];                     % Reference temperature (Ambient) [...
   Celcius]
P=1.01;                     % Reference pressure (Atmospheric) [Bar]
V=100;                      % Total volume flow [ml/min]
Me=[4 8 12 8 8];            % Methane volume flow
St=[22 22 22 19 16];        % Steam volume flow
Hy=[5 5 5 5 5];             % Hydrogen volume flow
Ni=V-Me-St-Hy;              % Nitrogen volume flow

global FP

Model = 'GasMix';
nCmp  = 1;          % of no importance in case of pure fluid
Cnc   = [1,0];      % of no importance in case of pure fluid
```

```
Cmp    = 'CH4';

ErrorMsg = invoke(FP,'SetFluid_M',Model,nCmp,Cmp,Cnc)

[rho,ErrorMsg] = invoke(FP,'Density','TP',T,P);
m_Me=rho*Me/(60*1000*1000);

Cmp    = 'H2O';

[rho,ErrorMsg] = invoke(FP,'Density','TP',T,P);
m_St=rho*St/(60*1000*1000);

Cmp    = 'H2';

ErrorMsg = invoke(FP,'SetFluid_M',Model,nCmp,Cmp,Cnc)

[rho,ErrorMsg] = invoke(FP,'Density','TP',T,P);
m_Hy=rho*Hy/(60*1000*1000);

Cmp    = 'N2';

ErrorMsg = invoke(FP,'SetFluid_M',Model,nCmp,Cmp,Cnc)

[rho,ErrorMsg] = invoke(FP,'Density','TP',T,P);
m_Ni=rho*Ni/(60*1000*1000);

% Total mass flow at reference conditions [kg/s]
M=m_Me+m_St+m_Hy+m_Ni

% Mass flows of individual compounds [kg/s]
mf_Me=m_Me./M
mf_St=m_St./M
mf_Hy=m_Hy./M
```

Calculate equilibrium constants

Methane Steam Reforming

```
%% Calculating equilibrium constant for the Methane Steam Reforming ...
   reaction
% Calculation requires FluidProp

Init_FluidProp
T=1023-273;          % Temperature [Celcius]
P=1.01;              % Pressure [Bar]
R=8.314462175;       % Universal gas constant [J/mol K]

global FP

Model = 'GasMix';
nCmp  = 1;          % of no importance in case of pure fluid
Cnc   = [1,0];      % of no importance in case of pure fluid
Cmp   = 'H2';

ErrorMsg = invoke(FP,'SetFluid_M',Model,nCmp,Cmp,Cnc);
```

```
[h,ErrorMsg] = invoke(FP,'Enthalpy','TP',T,P);
[s,ErrorMsg] = invoke(FP,'Entropy','TP',T,P);
G_h2=(h-(T+273)*s)*2;

Cmp    = 'H2O';

ErrorMsg = invoke(FP,'SetFluid_M',Model,nCmp,Cmp,Cnc);

[h,ErrorMsg] = invoke(FP,'Enthalpy','TP',T,P);
[s,ErrorMsg] = invoke(FP,'Entropy','TP',T,P);
G_h2o=(h-(T+273)*s)*18;

Cmp    = 'CO';

ErrorMsg = invoke(FP,'SetFluid_M',Model,nCmp,Cmp,Cnc);

[h,ErrorMsg] = invoke(FP,'Enthalpy','TP',T,P);
[s,ErrorMsg] = invoke(FP,'Entropy','TP',T,P);
G_co=(h-(T+273)*s)*28;

Cmp    = 'CH4';

ErrorMsg = invoke(FP,'SetFluid_M',Model,nCmp,Cmp,Cnc);

[h,ErrorMsg] = invoke(FP,'Enthalpy','TP',T,P);
[s,ErrorMsg] = invoke(FP,'Entropy','TP',T,P);
G_ch4=(h-(T+273)*s)*16;

% Change in Gibbs free energy
dG=(G_ch4+G_h2o)-((3*G_h2)+G_co);

% Equilibrium constant
K=exp(dG/(R*(T+273.15)))
```

Water Gas Shift

```
%% Calculating equilibrium constant for the Water Gas Shift reaction
% Calculation requires FluidProp

Init_FluidProp
T=1023-273;          % Temperature [Celcius]
P=1.01;              % Pressure [Bar]
R=8.314462175;       % Universal gas constant [J/mol K]

global FP

Model = 'GasMix';
nCmp  = 1;          % of no importance in case of pure fluid
Cnc   = [1,0];      % of no importance in case of pure fluid
Cmp   = 'H2';

ErrorMsg = invoke(FP,'SetFluid_M',Model,nCmp,Cmp,Cnc);

[h,ErrorMsg] = invoke(FP,'Enthalpy','TP',T,P);
[s,ErrorMsg] = invoke(FP,'Entropy','TP',T,P);
G_h2=(h-(T+273)*s)*2;
```

```
Cmp    = 'H2O';

ErrorMsg = invoke(FP,'SetFluid_M',Model,nCmp,Cmp,Cnc);

[h,ErrorMsg] = invoke(FP,'Enthalpy','TP',T,P);
[s,ErrorMsg] = invoke(FP,'Entropy','TP',T,P);
G_h2o=(h-(T+273)*s)*18;

Cmp    = 'CO';

ErrorMsg = invoke(FP,'SetFluid_M',Model,nCmp,Cmp,Cnc);

[h,ErrorMsg] = invoke(FP,'Enthalpy','TP',T,P);
[s,ErrorMsg] = invoke(FP,'Entropy','TP',T,P);
G_co=(h-(T+273)*s)*28;

Cmp    = 'CO2';

ErrorMsg = invoke(FP,'SetFluid_M',Model,nCmp,Cmp,Cnc);

[h,ErrorMsg] = invoke(FP,'Enthalpy','TP',T,P);
[s,ErrorMsg] = invoke(FP,'Entropy','TP',T,P);
G_co2=(h-(T+273)*s)*44;

% Change in Gibbs free energy
dG=(G_co+G_h2o)-(G_h2+G_co2);

% Equilibrium constant
K=exp(dG/(R*(T+273.15)))
```

Fit data to the Ideal Plug Flow Reactor model

Optimisation

```
%% Fit everything to an Ideal Plug Flow Reactor model

% Initial condition
opt0=[1e5;80];

% Optimization for most constant k
options = optimset('LargeScale','off','TolFun',1e-4,'MaxFunEvals'...
   ,5000,'MaxIter',5000,'PlotFcns',@optimplotx);
[optimum,fval,exitflag,output] = fminsearch(@(opt) optimizeall_IPFR(...
   opt), opt0, options);
[yt,k1,k2,k3,T1,T2,T3]=optimizeall_IPFR(optimum);

% Fitting the activation energies, determining k0 and Ea
R=8.314462175;

for i=1:min(size(k1))
    [curvefit,G]=fit((1./T1)',k1(i,:)','poly1');
    P=coeffvalues(curvefit);
    Ea_1(i)=-P(1)*R/1000;
    k0_1(i)=P(2);
end
```

```
for i=1:min(size(k2))
    [curvefit,G]=fit((1./T2)',k2(i,:)','poly1');
    P=coeffvalues(curvefit);
    Ea_2(i)=-P(1)*R/1000;
    k0_2(i)=P(2);
end

for i=1:min(size(k3))
    [curvefit,G]=fit((1./T3)',k3(i,:)','poly1');
    P=coeffvalues(curvefit);
    Ea_3(i)=-P(1)*R/1000;
    k0_3(i)=P(2);
end

% Results of the optimization
Ea_1
Ea_2
Ea_3
k0_1
k0_2
k0_3
A=optimum(1)
H=optimum(2)
```

Function to determine k

```
function [yt,k1,k2,k3,T1,T2,T3]=optimizeall_IPFR(opt)

% Constants for which is (not) optimized
Ah2o=opt(1);
Hh2o=opt(2);
% Ach4=opt(3);
% Hch4=opt(4);
Ach4=0;
Hch4=0;
% Ah2=opt(5);
% Hh2=opt(6);
Ah2=0;
Hh2=0;
% a=opt(7);
% b=opt(8);
a=1.5;
b=0;

% 3 Layer button cell
% Conditions
T=[1048 1023 998 973];
Ft=6.7941e-05;
Fa=96485;
F=([4 8 12 8 8]./100)*Ft;
SC=[22 22 22 19 16]./[4 8 12 8 8];
HC=5./[4 8 12 8 8];

% Determine k for the experimental data

% 3L, OC
xf1 = [0.238, 0.158,0.100,0.250,0.274];%oc,3L
```

```
xf2 = [0.236,0.170,0.125,0.256,0.273];%oc,3L
xf3 = [0.261,0.186,0.167,0.257,0.260];%OC,3L
xf4 = [0.262,0.227,0.207,0.263,0.269];%oc,3L
xf=[xf1;xf2;xf3;xf4];
I=0;
CC=I./(2*Fa*(ones(min(size(xf)),1)*F).*xf);

for i=1:min(size(xf))
    for j=1:length(xf)
        k11(i,j)=integral(@(x)rate_IPFR(x,a,b,F(j),Ft,SC(j),HC(j),CC(...
           i,j),T(i),Ah2o,Hh2o,Ach4,Hch4,Ah2,Hh2),0,xf(i,j));
    end
end
y11=mean(std(k11')./mean(k11'));

% 3L, A
xf1 = [0.418,0.330,0.298,0.387,0.470];%case a,3L
xf2 = [0.474,0.352,0.317,0.421,0.457];%case a,3L
xf3 = [0.507,0.370,0.334,0.425,0.430];%case a,3L
xf4 = [0.511,0.376,0.340,0.430,0.420];%case a,3L
xf=[xf1;xf2;xf3;xf4];
I=0.06;
CC=I./(2*Fa*(ones(min(size(xf)),1)*F).*xf);

for i=1:min(size(xf))
    for j=1:length(xf)
        k12(i,j)=integral(@(x)rate_IPFR(x,a,b,F(j),Ft,SC(j),HC(j),CC(...
           i,j),T(i),Ah2o,Hh2o,Ach4,Hch4,Ah2,Hh2),0,xf(i,j));
    end
end
y12=mean(std(k12')./mean(k12'));

% 3L, B
xf1 = [0.416,0.329,0.289,0.388,0.416];%case b,3L
xf2 = [0.473,0.352,0.319,0.408,0.423];%case b,3L
xf3 = [0.509,0.374,0.333,0.429,0.434];%case b,3L
xf4 = [0.508,0.377,0.379,0.436,0.443];%case b,3L
xf=[xf1;xf2;xf3;xf4];
I=0.1;
CC=I./(2*Fa*(ones(min(size(xf)),1)*F).*xf);

for i=1:min(size(xf))
    for j=1:length(xf)
        k13(i,j)=integral(@(x)rate_IPFR(x,a,b,F(j),Ft,SC(j),HC(j),CC(...
           i,j),T(i),Ah2o,Hh2o,Ach4,Hch4,Ah2,Hh2),0,xf(i,j));
    end
end
y13=mean(std(k13')./mean(k13'));

% If k is assumed to be constant with current density
k1=[k11 k12 k13];
y1=mean(std(k1')./mean(k1'));

T1=T;

% 5 Layer button cell
% Clear data and define new conditions
clear xf T
```

```
T=[1048 1023 973];

% Determine k for the experimental data

% 5L, OC
xf1 = [0.218, 0.210,0.190,0.241,0.243];%oc,5L
xf2 = [0.273,0.240,0.175,0.228,0.226];%oc,5L
xf3 = [0.348,0.248,0.206,0.223,0.220];%oc,5L
xf=[xf1;xf2;xf3];
I=0;
CC=I./(2*Fa*(ones(min(size(xf)),1)*F).*xf);

for i=1:min(size(xf))
    for j=1:length(xf)
        k21(i,j)=integral(@(x)rate_IPFR(x,a,b,F(j),Ft,SC(j),HC(j),CC(...
           i,j),T(i),Ah2o,Hh2o,Ach4,Hch4,Ah2,Hh2),0,xf(i,j));
    end
end
y21=mean(std(k21')./mean(k21'));

% 5L, A
xf1 = [0.732,0.569,0.543,0.606,0.636];%case a,5L
xf2 = [0.735,0.549,0.503,0.575,0.604];%case a,5L
xf3 = [0.781,0.589,0.519,0.566,0.610];%case a,5L
xf=[xf1;xf2;xf3];
I=0.06;
CC=I./(2*Fa*(ones(min(size(xf)),1)*F).*xf);

for i=1:min(size(xf))
    for j=1:length(xf)
        k22(i,j)=integral(@(x)rate_IPFR(x,a,b,F(j),Ft,SC(j),HC(j),CC(...
           i,j),T(i),Ah2o,Hh2o,Ach4,Hch4,Ah2,Hh2),0,xf(i,j));
    end
end
y22=mean(std(k22')./mean(k22'));

% 5L, B
xf1 = [0.738,0.531,0.492,0.585,0.482];%case b,5L
xf2 = [0.736,0.546,0.460,0.575,0.573];%case b,5L
xf3 = [0.777,0.587,0.517,0.571,0.568]; %b,5L
xf=[xf1;xf2;xf3;];
I=0.1;
CC=I./(2*Fa*(ones(min(size(xf)),1)*F).*xf);

for i=1:min(size(xf))
    for j=1:length(xf)
        k23(i,j)=integral(@(x)rate_IPFR(x,a,b,F(j),Ft,SC(j),HC(j),CC(...
           i,j),T(i),Ah2o,Hh2o,Ach4,Hch4,Ah2,Hh2),0,xf(i,j));
    end
end
y23=mean(std(k21')./mean(k23'));

% If k is assumed to be constant with current density
k2=[k21 k22 k23];
y2=mean(std(k2')./mean(k2'));

T2=T;
```

```
% Square cell
% Clear data and define new conditions
clear xf T SC HC F Ft
T=[1023 998 973];
Ft=6.93e-4;
V=1020;
F=([220 240 260 300 220 220 220]./V).*Ft;
SC=[450 450 450 450 480 510 540]./[220 240 260 300 220 220 220];
HC=80./[220 240 260 300 220 220 220];

% Determine k for the experimental data

% SG, OC
xf1=[0.856 0.848 0.832 0.8 0.862 0.865 0.866];
xf2=[0.782 0.776 0.762 0.738 0.78 0.784 0.782];
xf3=[0.672 0.666 0.654 0.632 0.67 0.665 0.666];
xf=[xf1;xf2;xf3;];
I=0;
CC=I./(2*Fa*(ones(min(size(xf)),1)*F).*xf);

for i=1:min(size(xf))
    for j=1:length(xf)
        k31(i,j)=integral(@(x)rate_IPFR(x,a,b,F(j),Ft,SC(j),HC(j),CC(...
           i,j),T(i),Ah2o,Hh2o,Ach4,Hch4,Ah2,Hh2),0,xf(i,j));
    end
end
y31=mean(std(k31')./mean(k31'));

% SG, A
xf1=[0.860 0.852 0.837 0.818 0.86 0.86 0.86];
xf2=[0.796 0.782 0.77 0.75 0.79 0.798 0.788];
xf3=[0.716 0.706 0.69 0.656 0.71 0.715 0.713];
xf=[xf1;xf2;xf3];
I=4.86;
CC=I./(2*Fa*(ones(min(size(xf)),1)*F).*xf);

for i=1:min(size(xf))
    for j=1:length(xf)
        k32(i,j)=integral(@(x)rate_IPFR(x,a,b,F(j),Ft,SC(j),HC(j),CC(...
           i,j),T(i),Ah2o,Hh2o,Ach4,Hch4,Ah2,Hh2),0,xf(i,j));
    end
end
y32=mean(std(k32')./mean(k32'));

% SG, B
xf1=[0.873 0.865 0.846 0.829 0.873 0.87 0.874];
xf2=[0.799 0.792 0.78 0.754 0.795 0.796 0.792];
xf3=[0.718 0.709 0.693 0.658 0.715 0.717 0.712];
xf=[xf1;xf2;xf3];
I=8.1;
CC=I./(2*Fa*(ones(min(size(xf)),1)*F).*xf);

for i=1:min(size(xf))
    for j=1:length(xf)
        k33(i,j)=integral(@(x)rate_IPFR(x,a,b,F(j),Ft,SC(j),HC(j),CC(...
           i,j),T(i),Ah2o,Hh2o,Ach4,Hch4,Ah2,Hh2),0,xf(i,j));
    end
end
```

```
y33=mean(std(k33')./mean(k33'));

% If k is assumed to be constant with current density
k3=[k31 k32 k33];
y3=mean(std(k3')./mean(k3'));

T3=T;

k1=log([mean(k11');mean(k12');mean(k13')]);
k2=log([mean(k21');mean(k22');mean(k23')]);
k3=log([mean(k31');mean(k32');mean(k33')]);

% y1=y11+y12+y13;       % Use if k can change with current density
% y2=y21+y22+y23;       % Use if k can change with current density
% y3=y31+y32+y33;       % Use if k can change with current density

% Determines for which data is optimized
% yt=y1;
% yt=y2;
yt=y3;
% yt=y1+y2;
% yt=y1+y2+y3;
% yt=y21;

end
```

Integrated function F/r

```
function [r]=rate_IPFR(x,a,b,F,Ft,SC,HC,CC,T,Akh2o,Hh2o,Akch4,Hch4,...
   Akh2,Hh2)

% Constants
R=8.314462175;      % Universal gas constant [J/mol K]
P=1.0135;           % Pressure [Bar]

% Calculation of equilibrium constants
% K1=exp(-27070/T+30.032);              % Equilibrium constant MSR
K2=exp(4202.5/T-3.928);                 % Equilibrium constant WGS
% Kco=Akco*exp((-Hco*10^3)/(R*T));
Kh2=Akh2*exp((-Hh2*10^3)/(R*T));
Kch4=Akch4*exp((-Hch4*10^3)/(R*T));
Kh2o=Akh2o*exp((-Hh2o*10^3)/(R*T));

% Calculate y, the amount of methane converted to carbon dioxide
y=(HC + 3*x + CC*x - (CC^2*K2^2*x.^2 + 2*CC^2*K2*x.^2 + CC^2*x.^2 + ...
   2*CC*HC*K2*x + 2*CC*HC*x + 2*CC*K2^2*SC*x - 4*CC*K2^2*x.^2 + 2*CC*...
   K2*SC*x + 10*CC*K2*x.^2 + 6*CC*x.^2 + HC^2 + 2*HC*K2*SC + 6*HC*x +...
    K2^2*SC^2 - 4*K2^2*SC*x + 4*K2^2*x.^2 + 10*K2*SC*x - 4*K2*x.^2 + ...
   9*x.^2).^(1/2) + K2*SC + CC*K2*x)/(2*(K2 - 1));

% Adjust total molar flow (CH4 + H2O --> 3 H2 + CO)
pt=Ft*(1+2*(F/Ft)*x);

% Species partial pressures:
pch4=(F./pt).*(1-x)*P;
ph2o=(F./pt).*(SC-x*(1-CC)-y)*P;
ph2=(F./pt).*(HC+x*(3-CC)+y)*P;
```

```
% pco=(F./pt).*(x-y)*P;
% pco2=(F./pt)*y*P;

% If adsorption of CH4 and H2 is not considered
Kch4=0;
Kh2=0;

% F/reaction rate, integrated to find k. Replace by desired ...
   expression.
r=F./((pch4./ph2.^a).*(ph2o./ph2)./((1+(Kh2o.*ph2o./ph2)+(Kch4.*pch4)...
   +(Kh2.*ph2)).^2));
% r=F./(pch4.^a.*ph2o.^b);
end
```

Fit data to the Contineous Ideally Stirred Tank Reactor

Optimisation

```
%% Fit everything to a Contineous Ideally Stirred Tank Reactor model

% Initial condition
opt0=[1e5;80];

% Optimization for most constant k
options = optimset('LargeScale','off','TolFun',1e-4,'MaxFunEvals'...
   ,5000,'MaxIter',5000,'PlotFcns',@optimplotx);
[optimum,fval,exitflag,output] = fminsearch(@(opt) optimizeall_CSTR(...
   opt), opt0, options);
[yt,k1,k2,k3,T1,T2,T3]=optimizeall_CSTR(optimum);

% Fitting the activation energies, determining k0 and Ea
R=8.314462175;

for i=1:min(size(k1))
    [curvefit,G]=fit((1./T1)',k1(i,:)','poly1');
    P=coeffvalues(curvefit);
    Ea_1(i)=-P(1)*R/1000;
    k0_1(i)=P(2);
end

for i=1:min(size(k2))
    [curvefit,G]=fit((1./T2)',k2(i,:)','poly1');
    P=coeffvalues(curvefit);
    Ea_2(i)=-P(1)*R/1000;
    k0_2(i)=P(2);
end

for i=1:min(size(k3))
    [curvefit,G]=fit((1./T3)',k3(i,:)','poly1');
    P=coeffvalues(curvefit);
    Ea_3(i)=-P(1)*R/1000;
    k0_3(i)=P(2);
end

% Results of the optimization
Ea_1
```

```
Ea_2
Ea_3
k0_1
k0_2
k0_3
A=optimum(1)
H=optimum(2)
```

Function to determine k

```
function [yt,k1,k2,k3,T1,T2,T3]=optimizeall_CSTR(opt)

% Constants for which is (not) optimized
Ah2o=opt(1);
Hh2o=opt(2);
% Ach4=opt(3);
% Hch4=opt(4);
Ach4=0;
Hch4=0;
% Ah2=opt(5);
% Hh2=opt(6);
Ah2=0;
Hh2=0;
% a=opt(7);
% b=opt(8);
a=1.5;
b=0;

% 3 Layer button cell
% Conditions
T=[1048 1023 998 973];
Ft=6.7941e-05;
Fa=96485;
F=([4 8 12 8 8]./100)*Ft;
SC=[22 22 22 19 16]./[4 8 12 8 8];
HC=5./[4 8 12 8 8];

% Determine k for the experimental data

% 3L, OC
xf1 = [0.238, 0.158,0.100,0.250,0.274];%oc,3L
xf2 = [0.236,0.170,0.125,0.256,0.273];%oc,3L
xf3 = [0.261,0.186,0.167,0.257,0.260];%OC,3L
xf4 = [0.262,0.227,0.207,0.263,0.269];%oc,3L
xf=[xf1;xf2;xf3;xf4];
I=0;
CC=I./(2*Fa*(ones(min(size(xf)),1)*F).*xf);

for i=1:min(size(xf))
    for j=1:length(xf)
        k11(i,j)=F(j).*xf(i,j)./rate_CSTR(xf(i,j),a,b,F(j),Ft,SC(j),...
           HC(j),CC(i,j),T(i),Ah2o,Hh2o,Ach4,Hch4,Ah2,Hh2);
    end
end
y11=mean(std(k11')./mean(k11'));

% 3L, A
```

```
xf1 = [0.418,0.330,0.298,0.387,0.470];%case a,3L
xf2 = [0.474,0.352,0.317,0.421,0.457];%case a,3L
xf3 = [0.507,0.370,0.334,0.425,0.430];%case a,3L
xf4 = [0.511,0.376,0.340,0.430,0.420];%case a,3L
xf=[xf1;xf2;xf3;xf4];
I=0.06;
CC=I./(2*Fa*(ones(min(size(xf)),1)*F).*xf);

for i=1:min(size(xf))
    for j=1:length(xf)
        k12(i,j)=F(j).*xf(i,j)./rate_CSTR(xf(i,j),a,b,F(j),Ft,SC(j),...
           HC(j),CC(i,j),T(i),Ah2o,Hh2o,Ach4,Hch4,Ah2,Hh2);
    end
end
y12=mean(std(k12')./mean(k12'));

% 3L, B
xf1 = [0.416,0.329,0.289,0.388,0.416];%case b,3L
xf2 = [0.473,0.352,0.319,0.408,0.423];%case b,3L
xf3 = [0.509,0.374,0.333,0.429,0.434];%case b,3L
xf4 = [0.508,0.377,0.379,0.436,0.443];%case b,3L
xf=[xf1;xf2;xf3;xf4];
I=0.1;
CC=I./(2*Fa*(ones(min(size(xf)),1)*F).*xf);

for i=1:min(size(xf))
    for j=1:length(xf)
        k13(i,j)=F(j).*xf(i,j)./rate_CSTR(xf(i,j),a,b,F(j),Ft,SC(j),...
           HC(j),CC(i,j),T(i),Ah2o,Hh2o,Ach4,Hch4,Ah2,Hh2);
    end
end
y13=mean(std(k13')./mean(k13'));

% If k is assumed to be constant with current density
k1=[k11 k12 k13];
y1=mean(std(k1')./mean(k1'));

T1=T;

% 5 Layer button cell
% Clear data and define new conditions
clear xf T
T=[1048 1023 973];

% Determine k for the experimental data

% 5L, OC
xf1 = [0.218, 0.210,0.190,0.241,0.243];%oc,5L
xf2 = [0.273,0.240,0.175,0.228,0.226];%oc,5L
xf3 = [0.348,0.248,0.206,0.223,0.220];%oc,5L
xf=[xf1;xf2;xf3];
I=0;
CC=I./(2*Fa*(ones(min(size(xf)),1)*F).*xf);

for i=1:min(size(xf))
    for j=1:length(xf)
        k21(i,j)=F(j).*xf(i,j)./rate_CSTR(xf(i,j),a,b,F(j),Ft,SC(j),...
           HC(j),CC(i,j),T(i),Ah2o,Hh2o,Ach4,Hch4,Ah2,Hh2);
```

```
    end
end
y21=mean(std(k21')./mean(k21'));

% 5L, A
xf1 = [0.732,0.569,0.543,0.606,0.636];%case a,5L
xf2 = [0.735,0.549,0.503,0.575,0.604];%case a,5L
xf3 = [0.781,0.589,0.519,0.566,0.610];%case a,5L
xf=[xf1;xf2;xf3];
I=0.06;
CC=I./(2*Fa*(ones(min(size(xf)),1)*F).*xf);

for i=1:min(size(xf))
    for j=1:length(xf)
        k22(i,j)=F(j).*xf(i,j)./rate_CSTR(xf(i,j),a,b,F(j),Ft,SC(j),...
           HC(j),CC(i,j),T(i),Ah2o,Hh2o,Ach4,Hch4,Ah2,Hh2);
    end
end
y22=mean(std(k22')./mean(k22'));

% 5L, B
xf1 = [0.738,0.531,0.492,0.585,0.482];%case b,5L
xf2 = [0.736,0.546,0.460,0.575,0.573];%case b,5L
xf3 = [0.777,0.587,0.517,0.571,0.568]; %b,5L
xf=[xf1;xf2;xf3;];
I=0.1;
CC=I./(2*Fa*(ones(min(size(xf)),1)*F).*xf);

for i=1:min(size(xf))
    for j=1:length(xf)
        k23(i,j)=F(j).*xf(i,j)./rate_CSTR(xf(i,j),a,b,F(j),Ft,SC(j),...
           HC(j),CC(i,j),T(i),Ah2o,Hh2o,Ach4,Hch4,Ah2,Hh2);
    end
end
y23=mean(std(k21')./mean(k23'));

% If k is assumed to be constant with current density
k2=[k21 k22 k23];
y2=mean(std(k2')./mean(k2'));

T2=T;

% Square cell
% Clear data and define new conditions
clear xf T SC HC F Ft
% a=opt(11);
% b=opt(12);
T=[1023 998 973];
Ft=6.93e-4;
V=1020;
F=([220 240 260 300 220 220 220]./V).*Ft;
SC=[450 450 450 450 480 510 540]./[220 240 260 300 220 220 220];
HC=80./[220 240 260 300 220 220 220];

% Determine k for the experimental data

% SG, OC
xf1=[0.856 0.848 0.832 0.8 0.862 0.865 0.866];
```

```
xf2=[0.782 0.776 0.762 0.738 0.78 0.784 0.782];
xf3=[0.672 0.666 0.654 0.632 0.67 0.665 0.666];
xf=[xf1;xf2;xf3;];
I=0;
CC=I./(2*Fa*(ones(min(size(xf)),1)*F).*xf);

for i=1:min(size(xf))
    for j=1:length(xf)
        k31(i,j)=integral(@(x)rate_CSTR(x,a,b,F(j),Ft,SC(j),HC(j),CC(...
           i,j),T(i),Ah2o,Hh2o,Ach4,Hch4,Ah2,Hh2),0,xf(i,j));
    end
end
y31=mean(std(k31')./mean(k31'));

% SG, A
xf1=[0.860 0.852 0.837 0.818 0.86 0.86 0.86];
xf2=[0.796 0.782 0.77 0.75 0.79 0.798 0.788];
xf3=[0.716 0.706 0.69 0.656 0.71 0.715 0.713];
xf=[xf1;xf2;xf3];
I=4.86;
CC=I./(2*Fa*(ones(min(size(xf)),1)*F).*xf);

for i=1:min(size(xf))
    for j=1:length(xf)
        k32(i,j)=integral(@(x)rate_CSTR(x,a,b,F(j),Ft,SC(j),HC(j),CC(...
           i,j),T(i),Ah2o,Hh2o,Ach4,Hch4,Ah2,Hh2),0,xf(i,j));
    end
end
y32=mean(std(k32')./mean(k32'));

% SG, B
xf1=[0.873 0.865 0.846 0.829 0.873 0.87 0.874];
xf2=[0.799 0.792 0.78 0.754 0.795 0.796 0.792];
xf3=[0.718 0.709 0.693 0.658 0.715 0.717 0.712];
xf=[xf1;xf2;xf3];
I=8.1;
CC=I./(2*Fa*(ones(min(size(xf)),1)*F).*xf);

for i=1:min(size(xf))
    for j=1:length(xf)
        k33(i,j)=integral(@(x)rate_CSTR(x,a,b,F(j),Ft,SC(j),HC(j),CC(...
           i,j),T(i),Ah2o,Hh2o,Ach4,Hch4,Ah2,Hh2),0,xf(i,j));
    end
end
y33=mean(std(k33')./mean(k33'));

% If k is assumed to be constant with current density
k3=[k31 k32 k33];
y3=mean(std(k3')./mean(k3'));

T3=T;

k1=log([mean(k11');mean(k12');mean(k13')]);
k2=log([mean(k21');mean(k22');mean(k23')]);
k3=log([mean(k31');mean(k32');mean(k33')]);

y1=y11+y12+y13;          % Use if k can change with current density
y2=y21+y22+y23;          % Use if k can change with current density
```

```
% y3=y31+y32+y33;       % Use if k can change with current density

% Determines for which data is optimized
% yt=y1;
% yt=y2;
% yt=y3;
yt=y1+y2;
% yt=y1+y2+y3;
% yt=y11+y21;
% yt=y11;

end
```

Function to determine the rate

```
function [r]=rate_CSTR(x,a,b,F,Ft,SC,HC,CC,T,Akh2o,Hh2o,Akch4,Hch4,...
   Akh2,Hh2)

% Constants
R=8.314462175;      % Universal gas constant [J/mol K]
P=1.0135;           % Pressure [Bar]

% Calculation of equilibria
% K1=exp(-27070/T+30.032);            % Equilibrium constant MSR
K2=exp(4202.5/T-3.928);               % Equilibrium constant WGS
% Kco=Akco*exp((-Hco*10^3)/(R*T));
Kh2=Akh2*exp((-Hh2*10^3)/(R*T));
Kch4=Akch4*exp((-Hch4*10^3)/(R*T));
Kh2o=Akh2o*exp((-Hh2o*10^3)/(R*T));

% Calculate y, the amount of methane converted to carbon dioxide
y=(HC + 3*x + CC*x - (CC^2*K2^2*x.^2 + 2*CC^2*K2*x.^2 + CC^2*x.^2 + ...
   2*CC*HC*K2*x + 2*CC*HC*x + 2*CC*K2^2*SC*x - 4*CC*K2^2*x.^2 + 2*CC*...
   K2*SC*x + 10*CC*K2*x.^2 + 6*CC*x.^2 + HC^2 + 2*HC*K2*SC + 6*HC*x +...
    K2^2*SC^2 - 4*K2^2*SC*x + 4*K2^2*x.^2 + 10*K2*SC*x - 4*K2*x.^2 + ...
   9*x.^2).^(1/2) + K2*SC + CC*K2*x)/(2*(K2 - 1));

% Adjust total molar flow (CH4 + H2O --> 3 H2 + CO)
pt=Ft*(1+2*(F/Ft)*x)*P;

% Species partial pressures:
pch4=(F./pt).*(1-x)*P;
ph2o=(F./pt).*(SC-x*(1-CC)-y)*P;
ph2=(F./pt).*(HC+x*(3-CC)+y)*P;
% pco=(F./pt).*(x-y)*P;
% pco2=(F./pt).*y*P;

% If adsorption of CH4 and H2 is not considered
Kch4=0;
Kh2=0;

% Reaction rate. Replace by desired expression.
r=((pch4./ph2.^a).*(ph2o./ph2)./((1+(Kh2o.*ph2o./ph2)+(Kch4.*pch4)+(...
   Kh2.*ph2)).^2));
% r=(pch4.^a.*ph2o.^b);

end
```

Appendix F

User Defined volumetric rate equation in FLUENT

Square cell

```
/************************************************************************
UDF used to specify the volumetric MSR reaction rate for the Square
cell FLUENT model.
species [0] refers to the steam concentration, species [2] to the
hydrogen concentration. Make sure the species are in the correct
order in the Mixture Species dialog box.

This file only adjusts the volumetric rate for the reaction with
the name "reaction-1" which is default in FLUENT for the first
defined reaction.

The other variables (k0, Ea, exp_species) are taken from the
reaction input panel in FLUENT.

- L. van Biert -
************************************************************************/

#include "udf.h"

#define A1 173.8027
#define H1 3.50515e7

DEFINE_VR_RATE(vol_reac_rate,c,t,r,wk,yk,rate,rr_t)
{
real ci, prod, K1, DEN;
int i;

if (!strcmp(r->name, "reaction-1"))
{
prod = 1.;

K1 = A1 * exp( - H1 / (UNIVERSAL_GAS_CONSTANT * C_T(c,t)));


if (yk[2]==0)
```

```
DEN = 1;
else
DEN = pow((1 + K1*wk[2]*yk[0]/(yk[2]*wk[0])),2.0);

for(i = 0; i < r->n_reactants; i++)
{
ci = C_R(c,t) * yk[r->reactant[i]] / wk[r->reactant[i]];
prod *= pow(ci, r->exp_reactant[i]);
}


for(i = 0; i < r->n_products; i++)
{
if (yk[r->product[i]]==0)
prod *= 1;
else
{
ci = C_R(c,t) * yk[r->product[i]] / wk[r->product[i]];
prod *= pow(ci, r->exp_product[i]);
}
}


*rate = r->A * exp( - r->E / (UNIVERSAL_GAS_CONSTANT * C_T(c,t))) *
pow(C_T(c,t), r->b) * prod / DEN;

*rr_t = *rate;
}
else
{

prod = 1.;

for(i = 0; i < r->n_reactants; i++)
{
ci = C_R(c,t) * yk[r->reactant[i]] / wk[r->reactant[i]];
prod *= pow(ci, r->exp_reactant[i]);
}
*rate = r->A * exp( - r->E / (UNIVERSAL_GAS_CONSTANT * C_T(c,t))) *
pow(C_T(c,t), r->b) * prod;

*rr_t = *rate;
}
}
```

Button cell

```
/************************************************************************
UDF used to specify the volumetric MSR reaction rate for the Button
cell FLUENT model.
species [0] refers to the steam concentration, species [2] to the
hydrogen concentration. Make sure the species are in the correct
order in the Mixture Species dialog box.

This file only adjusts the volumetric rate for the reaction with
the name "reaction-1" which is default in FLUENT for the first
```

```
defined reaction.

The other variables (k0, Ea, exp_species) are taken from the
reaction input panel in FLUENT.

- L. van Biert
*****************************************************************/

#include "udf.h"

#define A1 2.448e6
#define H1 1.165e8

DEFINE_VR_RATE(vol_reac_rate,c,t,r,wk,yk,rate,rr_t)
{
real ci, prod, K1, DEN;
int i;

if (!strcmp(r->name, "reaction-1"))
{
prod = 1.;

K1 = A1 * exp( - H1 / (UNIVERSAL_GAS_CONSTANT * C_T(c,t)));


if (yk[2]==0)
DEN = 1;
else
DEN = pow((1 + K1*wk[2]*yk[0]/(yk[2]*wk[0])),2.0);;

for(i = 0; i < r->n_reactants; i++)
{
ci = C_R(c,t) * yk[r->reactant[i]] / wk[r->reactant[i]];
prod *= pow(ci, r->exp_reactant[i]);
}


for(i = 0; i < r->n_products; i++)
{
if (yk[r->product[i]]==0)
prod *= 1;
else
{
ci = C_R(c,t) * yk[r->product[i]] / wk[r->product[i]];
prod *= pow(ci, r->exp_product[i]);
}
}

*rate = r->A * exp( - r->E / (UNIVERSAL_GAS_CONSTANT * C_T(c,t))) *
pow(C_T(c,t), r->b) * prod / DEN;

*rr_t = *rate;
}
else
{

prod = 1.;
```

```
for(i = 0; i < r->n_reactants; i++)
{
ci = C_R(c,t) * yk[r->reactant[i]] / wk[r->reactant[i]];
prod *= pow(ci, r->exp_reactant[i]);
}
*rate = r->A * exp( - r->E / (UNIVERSAL_GAS_CONSTANT * C_T(c,t))) *
pow(C_T(c,t), r->b) * prod;

*rr_t = *rate;
}
}
```